

# QUIJOTE scientific results – XIII. Intensity and polarization study of supernova remnants in the QUIJOTE-MFI wide survey: CTB 80, Cygnus Loop, HB 21, CTA 1, Tycho and HB 9

C. H. López-Caraballo<sup>1,2</sup> \* B. Ruiz-Granados<sup>3</sup> R. T. Génova-Santos<sup>1,2</sup>  
 M. Fernández-Torreiro<sup>1,2</sup> J. A. Rubiño-Martín<sup>1,2</sup> M. W. Peel<sup>4,1,2</sup> F. Poidevin<sup>1,2</sup>  
 E. Artal<sup>5</sup> M. Ashdown<sup>6,7</sup> R. B. Barreiro<sup>8</sup> F. J. Casas<sup>8</sup> E. de la Hoz<sup>8,9,10</sup>  
 R. González-González<sup>1,2</sup> F. Guidi<sup>11</sup> D. Herranz<sup>8</sup> R. Hoyland<sup>1,2</sup> A. Lasenby<sup>6,7</sup>  
 E. Martínez-González<sup>8</sup> L. Piccirillo<sup>12</sup> R. Rebolo<sup>1,2,13</sup> D. Tramonte<sup>14,1,2</sup> F. Vansyngel<sup>1,2</sup>  
 P. Vielva<sup>8</sup> R. A. Watson<sup>12</sup>

<sup>1</sup>Instituto de Astrofísica de Canarias, E-38200 La Laguna, Tenerife, Spain

<sup>2</sup>Departamento de Astrofísica, Universidad de La Laguna, E-38206 La Laguna, Tenerife, Spain

<sup>3</sup>Departamento de Física. Facultad de Ciencias. Universidad de Córdoba. Campus de Rabanales, Edif. C2. Planta Baja. E-14071 Córdoba, Spain

<sup>4</sup>Imperial College London, Blackett Lab, Prince Consort Road, London SW7 2AZ, UK

<sup>5</sup>Universidad de Cantabria, Departamento de Ingeniería de Comunicaciones, Edificio Ingeniería de Telecomunicación, Plaza de la Ciencia nº 1, 39005 Santander, Spain

<sup>6</sup>Astrophysics Group, Cavendish Laboratory, University of Cambridge, J J Thomson Avenue, Cambridge CB3 0HE, UK

<sup>7</sup>Kavli Institute for Cosmology, University of Cambridge, Madingley Road, Cambridge CB3 0HA, UK

<sup>8</sup>Instituto de Física de Cantabria (IFCA), CSIC-Univ. de Cantabria, Avda. los Castros, s/n, E-39005 Santander, Spain

<sup>9</sup>Departamento de Física Moderna, Universidad de Cantabria, Avda. de los Castros s/n, 39005 Santander, Spain

<sup>10</sup>CNRS-UCB International Research Laboratory, Centre Pierre Binétruy, IRL2007, CPB-IN2P3, Berkeley, CA 94720, USA

<sup>11</sup>Institut d'Astrophysique de Paris, UMR 7095, CNRS & Sorbonne Université, 98 bis boulevard Arago, 75014 Paris, France

<sup>12</sup>Jodrell Bank Centre for Astrophysics, Alan Turing Building, Department of Physics & Astronomy, School of Natural Sciences, The University of Manchester, Oxford Road, Manchester, M13 9PL, U.K.

<sup>13</sup>Consejo Superior de Investigaciones Científicas, E-28006 Madrid, Spain

<sup>14</sup>Department of Physics, Xi'an Jiaotong-Liverpool University, 111 Ren'ai Road,

Suzhou Dushu Lake Science and Education Innovation District, Suzhou Industrial Park, Suzhou 215123, P.R. China.

Accepted XXX. Received YYY; in original form ZZZ

## ABSTRACT

We use the new QUIJOTE-MFI wide survey (11, 13, 17 and 19 GHz) to produce spectral energy distributions (SEDs), on an angular scale of 1 deg, of the supernova remnants (SNRs) CTB 80, Cygnus Loop, HB 21, CTA 1, Tycho and HB 9. We provide new measurements of the polarized synchrotron radiation in the microwave range. For each SNR, the intensity and polarization SEDs are obtained and modelled by combining QUIJOTE-MFI maps with ancillary data. In intensity, we confirm the curved power law spectra of CTB 80 and HB 21 with a break frequency  $\nu_b$  at  $2.0^{+1.2}_{-0.5}$  GHz and  $5.0^{+1.2}_{-1.0}$  GHz respectively; and spectral indices respectively below and above the spectral break of  $-0.34 \pm 0.04$  and  $-0.86 \pm 0.5$  for CTB 80, and  $-0.24 \pm 0.07$  and  $-0.60 \pm 0.05$  for HB 21. In addition, we provide upper limits on the Anomalous Microwave Emission (AME), suggesting that the AME contribution is negligible towards these remnants. From a simultaneous intensity and polarization fit, we recover synchrotron spectral indices as flat as  $-0.24$ , and the whole sample has a mean and scatter of  $-0.44 \pm 0.12$ . The polarization fractions have a mean and scatter of  $6.1 \pm 1.9\%$ . When combining our results with the measurements from other QUIJOTE studies of SNRs, we find that radio spectral indices are flatter for mature SNRs, and particularly flatter for CTB 80 ( $-0.24^{+0.07}_{-0.06}$ ) and HB 21 ( $-0.34^{+0.04}_{-0.03}$ ). In addition, the evolution of the spectral indices against the SNRs age is modelled with a power-law function, providing an exponent  $-0.07 \pm 0.03$  and amplitude  $-0.49 \pm 0.02$  (normalised at 10 kyr), which are conservative with respect to previous studies of our Galaxy and the Large Magellanic Cloud.

**Key words:** radiation mechanisms: general - radio continuum: ISM - ISM: supernova remnants - polarization

## 1 INTRODUCTION

In recent decades, observations devoted of the Cosmic Microwave Background (CMB, [Penzias & Wilson 1965](#); [Gamow 1946](#)) have allowed us to confirm the  $\Lambda$ -CDM paradigm successfully ([Corey & Wilkinson 1976](#); [Lubin et al. 1983](#); [Smoot et al. 1992](#); [Fixsen et al. 1996](#)) and have yielded cosmological parameters to the one percent level of precision ([Planck Collaboration et al. 2020](#); [Bennett et al. 2013](#)). Naturally, characterization of physical mechanisms that act in the Galactic Interstellar Medium (ISM) has also deepened, resulting in increased knowledge of synchrotron radiation. Such mechanisms include cosmic-ray electrons accelerated by the Galactic magnetic field ([Ginzburg & Syrovatskii 1965](#); [Gardner & Whiteoak 1966](#)), free-free emission due to electron-ion collisions ([Oster 1961a,b](#)), and thermal radiation originating in Galactic interstellar dust ([Hildebrand 1983](#); [Desert et al. 1990](#)) and triggering the discovery of Anomalous Microwave Emission (AME, [Kogut et al. 1996](#); [Leitch et al. 1997](#)). Despite this progress, Galactic emission remains a major hindrance for the study of CMB B-modes, which are induced by primordial gravitational waves and are hidden in CMB polarization patterns ([Starobinsky 1979](#); [Rubakov et al. 1982](#); [Kamionkowski et al. 1997](#); [Zaldarriaga & Seljak 1997](#)). A comprehensive characterization of Galactic emission on different scales is therefore mandatory in order to meet the challenge of current and upcoming studies of the CMB, as well as for improving our understanding of the ISM. Supernova Remnants (SNRs) are Galactic regions of interest, not only because their microwave emission is dominated by one of the main Galactic foregrounds (synchrotron radiation), but also because AME detections towards some SNRs have been reported (e.g. [Génova-Santos et al. 2017](#); [Tramonte et al. 2023](#)). In this context, the new QUIJOTE-MFI Wide Survey ([Rubiño-Martín et al. 2023](#)), covering the range 10–20 GHz, will provide new insight into intensity and polarization properties of supernova remnants and on the role played by AME in SNRs.

Observations of SNRs allow us to understand the physical process acting in these powerful astronomical objects and to model their evolution ([Dubner & Giacani 2015](#); [Vink 2020](#), and references therein). The radio-to-microwave emission from SNRs is explained in terms of synchrotron emission from cosmic ray electrons spiralling around magnetic field lines, where the shock waves driven by the remnant could accelerate particles by diffusive shock acceleration (DSA, [Bell 1978](#); [Blandford & Ostriker 1978](#)). For energies between  $10^{10}$  and  $10^{20}$  eV, the cosmic-ray spectrum is described by a power law distribution  $dN(E) = AE^{-\Gamma_p}dE$ , where  $A$  and  $E$  respectively represent a scale factor and the energy.  $\Gamma_p$  identifies the particle spectral index, which reaches typical values of  $\Gamma_p \approx 3$  for Galactic cosmic rays (e.g. see [Rybicki & Lightman 1979](#); [Vink 2020](#)). The particle spectral index can be related to the radio spectral index via  $\alpha_{\text{radio}} = (1 - \Gamma_p)/2$  (see e.g., [Rybicki & Lightman 1979](#)), where we adopt the convention  $S_\nu \propto \nu^{\alpha_{\text{radio}}}$  for the flux density spectrum. The DSA mechanism predicts  $\alpha_{\text{radio}} \approx -0.5$  for cases of strong compression shocks, as expected in SNRs. Radio observations of Galactic SNRs reveal an average radio spectral index of  $-0.5$  for shell-type remnants (Galactic SNRs catalog<sup>1</sup>, [Green 2019](#)), although there is a significant spread requiring theoretical explanation ([Dubner & Giacani 2015](#); [Vink 2020](#)). Despite the spread in spectral indices ([Bozzetto et al. 2017](#); [Ranasinghe & Leahy 2023](#)), observa-

tions suggest that young remnants are bright and have steep spectra (i.e.  $\alpha$  from  $-0.8$  to  $-1$ ), while mature remnants are fainter with flatter spectral indices (i.e.  $\alpha \lesssim -0.5$ ) (e.g. see [Clark & Caswell 1976](#); [Harris 1962](#); [Zeng et al. 2019](#)). For the Large Magellanic Cloud (LMC), [Bozzetto et al. \(2017\)](#) have established the correlation of the spectral index and age by using 29 LMC SNRs, including multi-epoch observations of the younger remnant SN1987A. The latter was crucial in confirming that evolved remnants have flatter spectral indices than younger ones. To date, the debate about the evolution of spectral index of Galactic SNRs is still open and is mostly blurred by significant scatter of the spectral index distribution ([Bozzetto et al. 2017](#); [Ranasinghe & Leahy 2023](#)).

Observations show lower polarization levels than expected. In an ideal case, the synchrotron emission is driven by a homogeneous magnetic field perfectly orientated with respect to the observer, yielding an intrinsic degree of polarization  $\Pi_o$  that can be written in term of the radio spectral index  $\alpha_{\text{radio}}$  as follows (e.g., [Ginzburg & Syrovatskii 1965](#)):

$$\Pi_o(\alpha_{\text{radio}}) = \frac{1 - \alpha_{\text{radio}}}{5/3 - \alpha_{\text{radio}}}, \quad (1)$$

which is independent of the frequency. Therefore, for values of  $\alpha = -0.5$  (predicted by the DSA) the maximum theoretical polarization degree is around 69% towards SNRs. However, owing to irregularities in the magnetic field, typical observed values range between 10 and 15% (e.g. see [Kotthes et al. 2006](#); [Gao et al. 2011](#)), while only in some exceptional cases with remarkable homogeneity of the magnetic field does the observed polarization levels reach around 60% (e.g. SN 1006, [Reynoso et al. 2013](#)). Low-angular resolution observations, e.g. QUIJOTE-MFI at scales of 1 deg, are usually affected by beam depolarization, causing lower polarization fractions in SNRs; for instance, [Génova-Santos et al. \(2017\)](#) found values of around 15% for a region containing W44. In this context, there are a variety of effects dimming the polarization ([Sokoloff et al. 1998](#)), spanning instrumental depolarization (e.g. beam and bandwidth depolarizations, [Gardner & Whiteoak 1966](#)) and physical conditions acting locally (e.g. inhomogeneous and/or non-uniform magnetic field, [Burn 1966](#); [Sazonov 1973](#)).

Whereas the radio emission of SNRs is well explained by synchrotron radiation, the physical mechanism responsible for AME is still under discussion. Electric dipole radiation (ED, [Draine & Lazarian 1998](#)) from very small ( $N \leq 10^3$  atoms) rapidly rotating ( $\sim 1.5 \times 10^{10} \text{s}^{-1}$ ) dust grains in the ISM, known as *spinning dust emission* (SD), appears to reproduce the observations well (see the review by [Dickinson et al. 2018](#), and references therein). However, other physical mechanisms such as magnetic dipole (MD) emission from thermal fluctuations in magnetic dust grains ([Draine & Lazarian 1999](#); [Draine & Hensley 2013](#)) and thermal emission from amorphous dust grains ([Nashimoto et al. 2020](#)), have been invoked to explain the intensity of AME behaviour. The observational polarization properties of AME, however, are still being debated, the only constraints suggesting weak or negligible polarization ([Rubiño-Martín et al. 2012a](#); [Dickinson et al. 2018](#)). Predictions from the SD yield a polarization fraction  $\Pi_{\text{AME}} \leq 1\%$  at 20 GHz (for grains aligned via resonance paramagnetic relaxation, [Lazarian & Draine 2000](#)), and significantly unpolarized levels where there is quantum alignment suppression ( $\ll 1\%$ , [Draine & Hensley 2016](#)). To date the most restrictive upper limits fall in the range  $\Pi_{\text{AME}} \leq 1\text{--}6\%$  (see [Kogut et al. 2007](#); [Macellari et al. 2011](#); [López-Caraballo et al. 2011](#); [Dickinson et al. 2011](#); [Rubiño-Martín et al. 2012a](#); [Herman et al. 2022](#)), the strongest being, QUIJOTE-MFI and WMAP data ([Génova-Santos et al. 2017](#)),  $\Pi_{\text{AME}} \leq 0.2\%$  at 41 GHz towards the

<sup>1</sup> Updated versions of the Galactic SNR catalog focusing on radio frequencies have been maintained by D. Green. The latest version is publicly available at [VizieR](http://vizier.cds.unistra.fr/viz-bin/VizieR?-source=VII/284) (<http://vizier.cds.unistra.fr/viz-bin/VizieR?-source=VII/284>)

molecular cloud W 43. Therefore, the presence of AME in the line of sight towards SNRs represents an opportunity of better understanding AME properties.

The first sign of an AME contribution to SNRs was found in 3C 396, a finding supported by a  $7\sigma$  excess at 33 GHz over the extrapolation of synchrotron emission from low frequencies (at 9 arcmin beam resolution, Scaife et al. 2007). Those claims were recently refuted using data on the same object from the Parkes 64 m telescope, where the microwave spectra can be well understood in terms of flatter ( $\alpha = -0.36 \pm 0.02$ ) synchrotron emission (Cruciani et al. 2016), with observations in the 5–30 GHz range being key to disentangling the AME, free–free and synchrotron contributions. The AME in SNRs has been studied mainly in studies characterizing the integrated spectral energy distribution on a scale of 1 deg, where WMAP, *Planck* and QUIJOTE data are considered. The integrated spectrum of the region dominated by W44 revealed a significant AME component at  $6\sigma$  (Génova-Santos et al. 2017); this was the first remnant studied with QUIJOTE-MFI data. For W49 and W51, the AME contribution was detected at  $4.7\sigma$  and  $4.0\sigma$  respectively (Tramonte et al. 2023), revealing the first AME detection for W51. They also provided evidence of no AME contribution for IC443 suggested by Loru et al. (2019) using observations on scales of few arc-minutes from the Sardinia Radio Telescope (SRT) at 1.6, 7.0, 21.4 GHz and ancillary flux densities (e.g. *Planck* measurements at resolution  $\lesssim 0.8$  deg, Planck Collaboration et al. 2016a). In addition, Loru et al. (2019) ruled out the presence of AME for W44, which was also supported by recent COMAP observations with similar beam resolutions (around 4.5 arcmin at 26–31 GHz, Rennie et al. 2022), having these higher resolutions than those of previous studies with QUIJOTE-MFI, WMAP and *Planck*. There is still a controversy about the presence of AME towards SNRs, where interaction with the surrounding of remnants or the overlapping of different emissions in the line of sight are the topics under discussion.

In this work, part of a series of QUIJOTE-MFI scientific papers, we characterize the intensity and polarized spectral energy distribution of six supernova remnants using the QUIJOTE-MFI wide survey data. Observational properties of the synchrotron emission towards the remnants are presented, with emphasis on the spectral index behaviour and the integrated polarization degree. This study complements the analysis of SNRs in other QUIJOTE-MFI publications (Génova-Santos et al. 2015a; Tramonte et al. 2023; Ruiz-Granados et al. 2023), which collectively provide a sample of SNRs that can be used to explore the evolution of the spectral indices and the statistics of the polarization fraction, and investigate the presence of AME towards SNRs on scales of 1 deg.

Section 2 of this article gives a brief overview of the SNR sample of this study. The QUIJOTE-MFI survey and ancillary data are described in Section 3. The methodology for building the intensity and polarized SED is presented in Section 4, which also shows the models and strategies used to perform the SED fits considering using a Markov Chain Monte Carlo (MCMC) approach. The main results and discussion about the characterization of each SNR are shown in Section 5, in addition to the statistical analysis of synchrotron properties and the possible AME contribution towards SNRs. Our main conclusions and summary are listed in Section 6.

## 2 SUPERNOVA REMNANTS IN THE QUIJOTE-MFI SURVEY

The QUIJOTE-MFI Wide Survey covers the full northern sky at four frequency bands between 10 and 20 GHz (see Section 3.1 and

Rubiño-Martín et al. 2023), which allow us to access approximately half of the Galactic plane (see Figure 1). In Table 1, we summarize the properties from literature of the SNRs studied here: CTB 80, Cygnus Loop, HB 21, CTA 1, Tycho and HB 9. For these remnants, the main radio and microwave properties are briefly described below (Section 2.1). In addition, this sample is supplemented by the SNRs characterized by other QUIJOTE papers using MFI data, which are used in the statistical analysis of Section 5. This supplementary group consists of W44 (the first remnant studied by QUIJOTE, Génova-Santos et al. 2017), IC443, W49 and W51 (current QUIJOTE-MFI wide survey release combined with deeper observations towards these regions, Tramonte et al. 2023). We shall be using here some of the physical parameters derived in those publications for these SNRs. The plerions or filled centre remnants, such as the Crab (Tau A), Cassiopeia A (Cas A) and 3C58, are not considered in the statistical analysis (see details in Section 5.7). The intensity and polarization SED of 3C 58 is characterized as part of the study of the Fan region (Ruiz-Granados et al. 2023, in prep.). For Tau A and Cas A, there will be a paper devoted to describing in detail the spectral properties of these important sources (Génova-Santos et al. 2023a, in prep.), which are calibrators for the QUIJOTE-MFI data (Rubiño-Martín et al. 2023).

### 2.1 SNRs studied in this paper

#### CTB 80

This is an old-age SNR with a composite morphology and significant polarization level based on radio observations (Velusamy & Kundu 1974; Angerhofer et al. 1981; Strom 1987). The structure of CTB 80 covers approximately  $130 \times 100$  arcmin<sup>2</sup> and is located at Galactic coordinates  $(l, b) = (68.8^\circ, +2.7^\circ)$ . It shows a central nebula, with a bright source of flat radio spectrum, surrounded by an extended plateau and three extended arms with steeper spectral indices (Mantovani et al. 1985; Castelletti et al. 2003). Its pulsar wind nebula (PWN) is powered by the pulsar PSR B1951+32 (discovered by Kulkarni et al. 1988), which has a period of 39.5 ms, a dispersion measure (DM) of  $45 \text{ cm}^{-3} \text{ pc}$  and rotation measure (RM) of  $-182 \pm 8 \text{ rad m}^{-2}$  (Hobbs et al. 2004; Weisberg et al. 2004). The distance had been estimated to lie between 1.4 and up to 5 kpc (Blair et al. 1984; Leahy & Ranasinghe 2012; Shan et al. 2018), which is compatible with the distance of 2 kpc associated with PSR B1951+32 (Kulkarni et al. 1988). This value is also used as a reference in the age estimation (45 to 82 kyr, Koo et al. 1990; Migliazzo et al. 2002; Zeiger et al. 2008; Suzuki et al. 2021). We assume conservatively that the age is most probably  $65 \pm 20$  kyr. CTB 80 has been detected in radio, optical, X-ray and gamma ray studies (e.g., Mavromatakis et al. 2001; Castelletti et al. 2003; Leahy & Ranasinghe 2012; Araya & Herrera 2021, and references therein). The X-ray emission associated with the pulsar PSR B1951+32 was reported by Safi-Harb et al. (1995), while the gamma ray emission analysis provides the cut-off energy,  $E_c = 5 \text{ GeV}$  and  $\Gamma = 1.75$  (Ramanamurthy et al. 1995; Abdo et al. 2010), which are common values for a PWN. In addition, the observed extended GeV emission could suggest that the SNR shock interacts with the surrounding interstellar medium (Araya & Herrera 2021).

The characterization of its radio spectrum is still not clear, owing to the spread of the integrated flux densities at frequencies lower than 3 GHz and the steepening of the spectral index at  $\geq 10$  GHz (Sofue et al. 1983; Planck Collaboration et al. 2016a). Several radio spectral indices  $\alpha_{\text{radio}}$  have been reported ranging from  $-0.36 \pm 0.02$  up to  $-0.45 \pm 0.03$  (Castelletti & Dubner 2005;

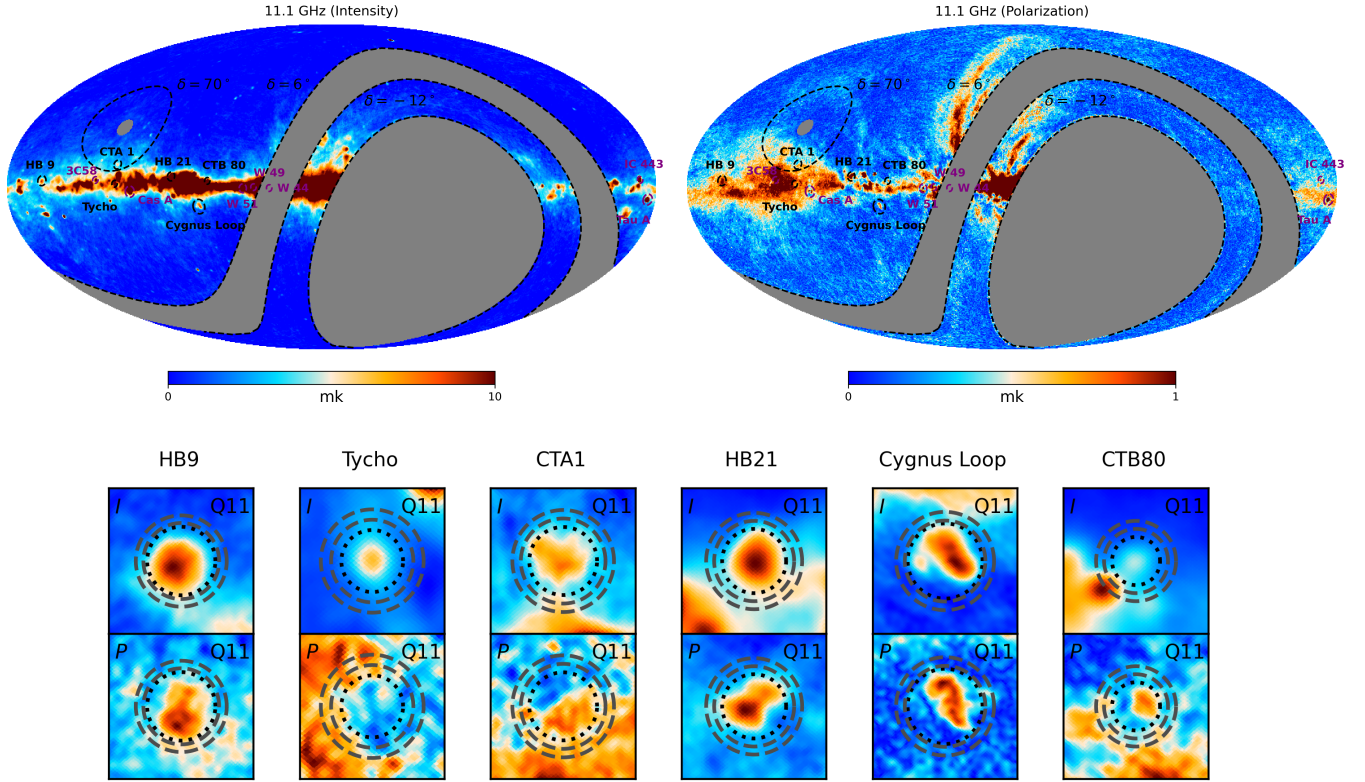


**Figure 1.** Supernova Remnants studied using QUIJOTE-MFI data. Top left and right panels respectively show the intensity and polarized intensity ( $P = \sqrt{Q^2 + U^2}$ , pixel-by-pixel) maps in the Galactic coordinate system, smoothed to 1 deg, from the QUIJOTE-MFI wide survey at 11 GHz. The apertures and names identify the SNRs studied using the QUIJOTE-MFI facility (see Table 1) in this study (black apertures, CTB 80, Cygnus Loop, HB 21, CTA 1, Tycho and HB 9) and in other publications (purple apertures, W44, W49, W51, Cas A, 3C 58, Tau A and IC443, see text). Bottom panels present the close view of intensity and polarized intensity maps of CTB 80 ( $6^\circ \times 6^\circ$ ), Cygnus Loop ( $8.4^\circ \times 8.4^\circ$ ), HB 21 ( $6^\circ \times 6^\circ$ ), CTA 1 ( $5.7^\circ \times 5.7^\circ$ ), Tycho ( $4.7^\circ \times 4.7^\circ$ ) and HB 9 ( $6^\circ \times 6^\circ$ ). Central positions and apertures are taken from Table 4, which are used in the flux density estimates (Section 4.1).

Kothes et al. 2006; Gao et al. 2011), which agree with spatial spectral variations observed across the SNR on arcmin scales (Castelletti & Dubner 2005). polarized signal has been detected at radio frequencies reaching a level of up to 50% at resolutions better than 10 arcmin (Velusamy & Kundu 1974; Kothes et al. 2006; Gao et al. 2011); e.g. 10–20% (the plateau and central regions) and 30–40% (towards arms) at 4750 MHz (Mantovani et al. 1985). Regarding average properties,<sup>2</sup> the average polarization fraction reaches values of  $12^{+10}_{-6}\%$  at 11 cm (Velusamy & Kundu 1974),  $7.6 \pm 0.7\%$  at 1420 MHz (Kothes et al. 2006) and  $13.2 \pm 2.0\%$  at 6 cm (Gao et al. 2011). These measurements suggest depolarization at lower frequencies, which is observed in high-resolution analyses (Mantovani et al. 1985; Li et al. 2020). The rotation registers fluctuations of  $35\text{--}85 \text{ rad m}^{-2}$  (Mantovani et al. 1985; Castelletti et al. 2021), which favours the depth depolarization from the pulsar region over the beam depolarization (Li et al. 2020).

<sup>2</sup> At angular resolutions better than 1 deg, the polarization intensity map can be computed to resolve the structure of the SNRs. In these cases, the average polarized intensity ( $PI_\nu$ ) can be defined as the mean of the polarization measurements over the pixels towards the SNR. Consequently, the average polarization fraction also arises from the polarization fraction map estimated pixel-by-pixel. Nevertheless  $\Pi_\nu = 100 * PI_\nu / S_\nu$  can be also consider as the polarization level towards the SNRs. These definitions depart from the integrated properties computed in this study (section 4.2), causing differences in the interpretation of the properties of SNRs.

### The Cygnus Loop

This is a large and archetypal middle-aged shell-type SNR also known as the Veil Nebula or Network Nebula. The Cygnus Loop is located at around  $l = 74.2^\circ$  and  $b = -8.7^\circ$  in a region with low Galactic emission (far enough from the Galactic plane), and is well-studied across the whole electromagnetic spectrum (Mantovani et al. 1985; Hester et al. 1986; Levenson et al. 1997, 1998; Katagiri et al. 2011; Loru et al. 2021). Its emission is moderate at radio–microwave frequencies and particularly intense in X-rays. It is approximately  $4^\circ \times 3^\circ$  in apparent size and covers a nearly circular shell, which is composed of prominent radio–microwave regions such as NGC 6960, NGC 6992, NGC 6995, the central filament and a southern shell (referenced in the equatorial coordinate system, Sun et al. 2006; Loru et al. 2021). This southern bubble-like structure was proposed to be another SNR based on its spectral index distribution and polarization properties (Uyaniker et al. 2002), however, this hypothesis has been refuted by X-ray observations (Katsuda et al. 2011; Leahy & Hassan 2013). The Cygnus Loop is located at a distance of  $735 \pm 25 \text{ pc}$  (Fesen et al. 2018b; Minkowski 1958), although distance estimates fall in the range 440–1400 pc (see Minkowski 1958; Blair et al. 2005; Fesen et al. 2018a, Table 1 for a summary). From X-ray and optical measurements, the estimated age spans the range 10–20 kyr, assuming that the Cygnus Loop is in an adiabatic phase and at the end of the Sedov stage (Ku

**Table 1.** Summary of the properties of supernova remnant sampled from the literature. The name and Galactic coordinates are shown in columns 1 and 2 respectively. For the distance, age and the spectral index of intensity-integrated spectrum ( $\alpha_{\text{radio}}$ ), we present the available coverage range for each parameter, as well as the value considered in this paper (in parentheses). We adopt the spectral index definition such that the flux densities follow  $S_\nu \propto \nu^\alpha$ . The last column presents comments or remarks about the SNR. References are presented throughout Section 2.1.

Name	Position <i>l, b</i> [deg,deg]		Distance [kpc]	Age [kyr]	$\alpha_{\text{radio}}$	Remarks or comments
CTB 80	68.8	+2.7	1.4 to 5 ( $2 \pm 0.5$ )	45–82 ( $65 \pm 20$ )	−0.0 to −0.8 ( $-0.45 \pm 0.03$ )	Curved microwave spectrum
Cyg. Loop	74.2	−8.8	0.4 to 1.4 ( $0.74 \pm 0.03$ )	10–20 ( $15 \pm 5$ )	−0.40 to −0.53 ( $-0.45 \pm 0.05$ )	
HB 21	89.0	+4.7	0.7 to 3.0 ( $1.74 \pm 0.5$ )	15–45 ( $30 \pm 15$ )	−0.27 to −0.41 ( $-0.38 \pm 0.02$ )	Curved microwave spectrum
CTA 1	119.5	+10.0	1.1 to 1.7 ( $1.4 \pm 0.3$ )	5–20 ( $14 \pm 4$ )	−0.5 to −0.7 ( $-0.63 \pm 0.05$ )	
Tycho	120.1	+1.0	2 to 5 ( $2.5 \pm 0.8$ )	1572 A.D.	−0.65 to −0.58 ( $-0.624 \pm 0.004$ )	
HB 9	160.4	+2.8	0.6 to 1.5 ( $0.6 \pm 0.3$ )	4–20 ( $6.6 \pm 1.5$ )	−0.44 to −0.64 ( $-0.59 \pm 0.02$ )	Mixed-morphology type

et al. 1984; Hester & Cox 1986; Miyata et al. 1994; Levenson et al. 1998; Fesen et al. 2018a).

In the radio range, Cygnus Loop is well described by observations from 400 MHz up to 5 GHz at resolutions of 1–10 arcmin (see Leahy & Roger 1998; Uyaniker et al. 2004; Sun et al. 2006). In intensity, the integrated spectrum has a spectral index of  $\alpha = -0.40 \pm 0.06$  for frequencies lower than 4.9 GHz (Sun et al. 2006; Uyaniker et al. 2004). When also considering higher frequencies, Loru et al. (2021) obtained  $\alpha = -0.53 \pm 0.01$  and an amplitude of  $164 \pm 5$  Jy (normalised at 1 GHz), using ancillary radio data (Uyaniker et al. 2004; Sun et al. 2006) and measurements from Medicina and *Planck* (at 30 GHz, Planck Collaboration et al. 2016a). Polarization varies across the Cygnus Loop, where some regions present levels of up to 35% (Kundu & Becker 1972; Leahy et al. 1997; Uyaniker et al. 2002; Sun et al. 2006). At 4.8 GHz, NGC 6992/5, NGC 6960 and the central filament (in the northern shell) show levels of up to 30%, and down to 20% in the southern shell (Sun et al. 2006; Kundu & Becker 1972). In contrast, at lower frequencies there are major polarization differences between the southern and northern regions, the northern region being less intense (Uyaniker et al. 2002). At 1.42 GHz, this reveals that the depolarization is significantly higher in northern areas than in the southern regions, where depolarization seems to be spatially correlated with X-ray emission (Leahy et al. 1997). Regarding rotation measure, differences remain between the north and south, with averages of  $-21 \text{ rad m}^{-2}$  and  $-73 \text{ rad m}^{-2}$  respectively (using 6, 11 and 21 cm, Sun et al. 2006).

### HB 21

This is a mixed-morphology and middle-aged SNR. HB 21 consists of an irregular radio shell of around  $2^\circ \times 1.5^\circ$  centred at  $l = 89.0^\circ$  and  $b = 4.7^\circ$ , whose morphology reveals interaction with molecular clouds (Hill 1974; Tatematsu et al. 1990; Byun et al. 2006) and the X-ray thermal emission is coming from its central area (Leahy & Aschenbach 1996; Knoedseder et al. 1996). Observations of CO and infrared lines confirm its interaction with molecular clouds (Koo & Heiles 1991; Shinn et al. 2009), where HB 21 is associated with the Cyg OB7 complex located at  $0.8 \pm 0.07$  kpc (Tatematsu et al. 1990; Leahy & Aschenbach 1996). Byun et al. (2006) recently suggested, on the basis of a compendium from multiple analyses and datasets, a conservative higher distance value of  $1.7 \pm 0.5$  kpc. Consequently, there is also a wide age range spanning the range 6–45 kyr (Kundu et al. 1973; Shinn et al. 2009; Flower & Pineau des Forêts 1999; Lazendic & Slane 2006; Byun et al. 2006). Here we adopt a conservative value of  $30 \pm 15$  kyr in order to remain

consistent with that obtained from its expanding HI shell (at 1.1 kpc, Kundu et al. 1973).

Concerning the radio–microwave properties, the intensity SED reveals a curved spectrum with a break frequency  $\nu_b = 5.9 \pm 1.2$  GHz, when a change of the spectral index of  $\Delta\alpha = -0.5$  is assumed (at  $\lesssim 100$  GHz, Pivato et al. 2013). The radio spectral index falls between  $-0.27$  to  $-0.41$  in the range  $\sim 0.03$ –5 GHz (e.g. see Willis 1973; Reich et al. 2003; Kothes et al. 2006, and references therein),  $\alpha_{\text{radio}} = -0.36 \pm 0.03$  being the adopted value (Gao et al. 2011; Pivato et al. 2013). At radio frequencies, HB 21 shows polarization level of up to 35% in some areas (Kundu et al. 1973; Kothes et al. 2006; Landecker et al. 2010; Gao et al. 2011). At 1420 MHz, polarized intensity is strongest in the east while it falls towards the western edge (at  $\sim 1$  arcmin scales, Reich et al. 2003; Landecker et al. 2010). At 4.8 GHz, Gao et al. (2011) found an average polarization intensity of  $PI_{4.8} = 11.3 \pm 1.1$  Jy yielding a polarization fraction of  $10.7 \pm 1.1$ %. The average polarization fraction seems to decrease at low frequencies ( $3.7 \pm 0.5$ % at 1.42 GHz, Kothes et al. 2006), although we also expect some differences caused by the resolutions of the maps used ( $\sim 1$  and 9.5 arcmin at 1.4 and 4.8 GHz respectively).

### CTA 1

In our sample, this is the farthest SNR from the Galactic plane. It is located at  $l = 119.5^\circ$  and  $b = 10.2^\circ$  and was discovered by Harris & Roberts (1960). CTA 1 shows the typical morphology of a radio fragmentary shell, which is composed of strong limb-brightened arcs (mainly in the south and southwest), a central branch and a diffuse extended emission covering a circular region of radius  $\sim 45$  arcmin. The breakout phenomenon is affecting the north-eastern part of the shell. Observations of CTA 1 span radio (Caswell et al. 1975; Sieber et al. 1979, 1981; Pineault et al. 1997), optical (Fesen et al. 1981, 1983; Mavromataki et al. 2007; Mignani et al. 2013), X-ray (Seward et al. 1995; Slane et al. 1997; Lin et al. 2012) and higher-energy bands (Romero et al. 1999; Aliu et al. 2013; Torres et al. 2003; Li et al. 2016; Martín et al. 2016). Pineault et al. (1993) obtained a kinematic distance of  $1.4 \pm 0.3$  kpc from HI observations. Fermi-LAT data allowed the detection and characterization of its pulsar and PWN (Abdo et al. 2008, 2012), yielding a period of  $\sim 316$  ms, a spin-down power of  $\sim 4.5 \times 10^{35} \text{ erg s}^{-1}$  and a characteristic age of 13.9 kyr for the pulsar. This age is in agreement with estimations based on radio and X-ray thermal emissions (5–20 kyr, Pineault et al. 1993; Slane et al. 1997, 2004), where we adopted the  $14 \pm 4$  kyr at 1.4 kpc (from Sedov expansion model, Slane et al. 2004) and accounting for an uncertainty of 25%.

At radio frequencies, the integrated spectrum of CTA 1 is described by a power law with a spectral index  $\alpha = -0.63 \pm 0.05$  in the 408–4800 MHz range (Sun et al. 2011a), which is in agreement with previously reported spectral indices (e.g.  $-0.57 \pm 0.006$ , Pineault et al. 1997). This spectral index from integrated SED is compatible with the spectral index distribution obtained at resolutions of around 10 arcmin, which has values around  $-0.5$  (shell structure),  $-0.6$  (central branch) and steepening in the breakout region (Pineault et al. 1997; Sun et al. 2011a; Sieber et al. 1981). Polarized emission has been reported from 1.4 to 4.8 GHz (Sieber et al. 1981, 1979; Sun et al. 2011a), where the average polarization fraction reaches levels of up to 40% (at 4.8 GHz) in the eastern shell (Sun et al. 2011a), significantly decreasing towards the breakout region (Sun et al. 2011a). The RM map shows variations between  $\pm 40 \text{ rad m}^{-2}$  (Sieber et al. 1981; Sun et al. 2011a), in full agreement with the RMs obtained from extragalactic sources in the line of sight of CTA 1 (Simonetti 1992; Taylor et al. 2009). These variations support the presence of a Faraday Screen (FS) in front of the remnant, driven by a regular magnetic field, between 2.7 and  $1.9 \mu\text{G}$ , in the direction opposite to the interstellar magnetic field.

### Tycho

Tycho is the remnant of a type Ia Supernova explosion, which was observed by Tycho Brahe in 1572 and has a long historical follow-up (Baade 1943; Hanbury Brown & Hazard 1952; Gorenstein et al. 1970; Acciari et al. 2011; Decourchelle 2017, and references therein) that includes the detection of optical scattered-light echoes (Krause et al. 2008; Rest et al. 2008). Tycho is catalogued as a shell-type SNR with a diameter of  $\sim 8$  arcmin in radio bands, which expands at  $0.1126\% \text{ yr}^{-1}$  into the ISM, suggesting that it is still evolving towards the Sedov adiabatic phase (Reynoso et al. 1997). Tycho is also called 3C 10 and SN 1572, and is located at  $l = 120.1^\circ$  and  $b = 1.4^\circ$ . Distance estimates range from 2 to 5 kpc, and are computed from radio, optical, X-ray and gamma-ray observations (see a summary in Hayato et al. 2010), but the kinematic distance of 2.5 kpc is widely used (Tian & Leahy 2011).

At radio–microwave frequencies, the integrated spectrum is characterized by a spectral index of  $\alpha = -0.624 \pm 0.004$  (0.015–70 GHz, Castelletti et al. 2021), which is compatible with previous estimates of about  $\alpha = -0.58 \pm 0.02$  for a similar frequency range (Sun et al. 2011b; Loru et al. 2019; Hurley-Walker et al. 2009). From higher-resolution observations, the spatial spectral variations fall in the  $-0.4$  to  $-0.8$  range (Katz-Stone et al. 2000; Arias et al. 2019) and is steeper near the central region of the remnant. In addition, low-frequency free–free self-absorption has been reported for some regions of Tycho (Arias et al. 2019), which is not observed in the integrated spectrum. In contrast, some studies have reported a weak concave-up spectrum with a smooth spectral break of  $\Delta\alpha \simeq 0.04$  at 1 GHz (Reynolds & Ellison 1992; Castelletti et al. 2021). The polarization fraction seems to be weak at radio frequencies. At 1.42 GHz, observations reveal that the polarization intensity consists of a faint arc structure, where the average percentage polarization is  $2.5 \pm 0.1\%$  (at  $\sim 1$  arcmin, Kothes et al. 2006). Sun et al. (2011b), on the other hand, reported a lower value of 1%, at 4.8 GHz from a map with beam resolution of 9.5 arcmin.

### HB 9

HB 9 is a middle-aged supernova remnant with a mixed-morphology type. In radio bands, shell-like shape of HB 9 has a large extension

**Table 2.** Summary of the sky surveys considered in this study. The first column gives the name of the facility or survey. The second column is the notation that identifies the map used, which has a central frequency (GHz), original beam resolution (arcmin), calibration error (as a percentage) and Stokes maps available (*I*, *Q* or *U*), as shown in the third, fourth, fifth and sixth columns respectively. The main references are identified by the last column.

Name	ID	Freq. [GHz]	FWHM [arcmin]	Cal. [%]	Stokes	Ref.
Several facilities	Has	0.408	51	10	<i>I</i>	1,2
Dwingeloo 25m	Dwi	0.820	72	10	<i>I</i>	3
DRAO 25.6m	Wol	1.410	36	10	<i>Q, U</i>	4
Stockert 25m & Villa-Elisa 30m	Rei	1.420	36	10	<i>I</i>	5,2
Urumqi 25m	Urq	4.8	9.5	10	<i>I, Q, U</i>	6
QUIJOTE-MFI	Q11	11.1	55.4	5	<i>I, Q, U</i>	7
QUIJOTE-MFI	Q13	12.9	55.8	5	<i>I, Q, U</i>	7
QUIJOTE-MFI	Q17	16.8	39.0	5,6,6	<i>I, Q, U</i>	7
QUIJOTE-MFI	Q19	18.8	40.3	5,6,6	<i>I, Q, U</i>	7
WMAP 9yr	WK	22.8	50.7	3	<i>I, Q, U</i>	8
Planck-LFI	P30	28.4	32.3	3	<i>I, Q, U</i>	9
WMAP 9yr	WKa	32.9	38.8	3	<i>I, Q, U</i>	8
WMAP 9yr	WQ	40.7	30.6	3	<i>I, Q, U</i>	8
Planck-LFI	P44	44.1	27.0	3	<i>I, Q, U</i>	9
WMAP 9yr	WV	60.7	20.9	3	<i>I, Q, U</i>	8
Planck-LFI	P70	70.4	13.2	3	<i>I, Q, U</i>	9
WMAP 9yr	WW	93.5	14.8	3	<i>I, Q, U</i>	8
Planck-HFI	P100	100	9.7	3	<i>I, Q, U</i>	9
Planck-HFI	P143	143	7.3	3	<i>I, Q, U</i>	9
Planck-HFI	P217	217	5.0	3	<i>I, Q, U</i>	9
Planck-HFI	P353	353	4.5	3	<i>I, Q, U</i>	9
Planck-HFI	P545	545	4.8	6.1	<i>I</i>	9
Planck-HFI	P857	857	4.6	6.4	<i>I</i>	9
COBE-DIRBE	D10	1249	37.1	11.6	<i>I</i>	10
COBE-DIRBE	D9	2141	38.0	10.6	<i>I</i>	10
COBE-DIRBE	D8	2997	38.6	13.5	<i>I</i>	10

References. 1: Haslam et al. (1982); 2: Platania et al. (2003); 3: Berkhuijsen (1971); 4: Wolleben et al. (2006); 5: Reich & Reich (1986); 6: Sun et al. (2007) and Gao et al. (2011); 7: Rubiño-Martín et al. (2023); 8: Bennett et al. (2013); 9: Planck Collaboration et al. (2020); 10: Hauser et al. (1998).

of approximately  $140 \times 120 \text{ arcmin}^2$  with structures similar to fragmented shells or filaments (Willis 1973; Denoyer 1974; Caswell 1976; Leahy & Roger 1991). The X-ray emission was discovered using HEAO-1 A2 soft X-ray data (Tuohy et al. 1979) and was later confirmed by X-ray missions such as GINGA and Suzaku (Yamauchi & Koyama 1993; Sezer et al. 2019; Saito et al. 2020). In particular, ROSAT observations allowed the detection of the compact thermal X-ray emission in the central part of HB 9 (Leahy & Aschenbach 1995). Other investigations included observations at various frequencies from the optical (Lozinskaia 1975; D’Odorico & Sabadin 1977; Lozinskaia 1980) up to gamma-rays (Araya 2014; Sezer et al. 2019; Abdollahi et al. 2020). For the latter, extended gamma-ray emission was detected in the line of sight to HB 9 (Fermi-LAT data, Araya 2014), but was not detected in the TeV energy regime (MAGIC observations, Carmona et al. 2009). HB 9 is also known as G160.9+2.6 (from early radio studies) although its central position is fixed at  $l = 160.4^\circ$  and  $b = 2.8^\circ$ . The H I and  $^{12}\text{CO}$  ( $J = 1-0$ ) analysis provided a kinematic distance of  $0.6 \pm 0.3 \text{ kpc}$  (Sezer et al. 2019), where the extinction distance of  $0.54 \pm 0.10 \text{ kpc}$  from stars

in the line of sight (GAIA survey, Zhao et al. 2020) suggests a connection between interstellar gas and the remnant. These estimates are in agreement with previous higher values of  $\lesssim 1.5$  kpc (Leahy & Tian 2007; Leahy & Aschenbach 1995). These latter studies also provided age estimates in the ranges 8–20 kyr (ROSAT data, Leahy & Aschenbach 1995) and 4–7 kyr (H $\alpha$  data, Leahy & Tian 2007), which establish HB 9 as a middle-aged SNR with a Sedov age of 6.6 kyr.

Regarding the radio properties, the integrated intensity SED is well described by a power law with a spectral index between  $-0.47$  and  $-0.64$  in the range from 0.01 to 5 GHz (e.g. see Dwarakanath et al. 1982; Kothes et al. 2006; Leahy & Tian 2007); for example, Gao et al. (2011) found  $\alpha = -0.59 \pm 0.02$  in the range 0.1–5 GHz. The spectral bend proposed by Willis (1973) at 1 GHz was not confirmed by observations at higher frequencies (Reich et al. 2003; Gao et al. 2011). The observed linear polarization across HB 9 implies a largely tangential orientation of the magnetic fields (1.4 and 2.7 GHz, Reich et al. 1983; Fürst & Reich 2004). At 1.42 GHz, the average linear polarization fraction is  $9.1 \pm 0.1\%$ , reaching a maximum of 59% (Kothes et al. 2006). Gao et al. (2011) reported a similar polarization level of  $15.6 \pm 1.6\%$  at 4.8 GHz for the entire region. In both cases, authors observed a spatial correlation between the highly polarized emission and the intensity signal coming from the outer filaments of the shell.

### 3 DATA

In this study, we use QUIJOTE-MFI wide survey data together with ancillary data from surveys such as WMAP, *Planck* and DIRBE. We cover the radio up to the far-infrared range in intensity (0.4–3000 GHz) while for polarization the range spans from 5 to 353 GHz. All maps are available in the HEALPix<sup>3</sup> pixelization scheme (Górski et al. 2005) and for different beam resolutions. For a coherent characterization of the spectral energy distribution of SNRs (Section 4.1), we use maps smoothed to a common angular resolution of 1 deg for an  $N_{\text{side}} = 512$  pixelization scheme, which corresponds to a pixel size of  $\sim 6.9$  arcmin and pixel solid angle  $\Omega_o = 3.9947 \times 10^{-6}$  sr. Table 2 presents the main properties of the data used in our analyses, which are briefly described below.

#### 3.1 QUIJOTE-MFI wide survey

The Q-U-I JOint TENERIFE CMB experiment (QUIJOTE, Rubiño-Martín et al. 2012b) is a scientific collaboration devoted to characterizing the polarization of the CMB and astrophysical foregrounds in the range 10–40 GHz. The QUIJOTE telescopes operate from the Teide Observatory (Tenerife, Spain) at 2400 m a.s.l. and cover most of the northern sky (above declination  $-35^\circ$ ) at an angular resolution of  $\sim 1$  deg. The QUIJOTE project consists of two telescopes (of crossed-Dragone design, Gomez et al. 2010; Sanquircé et al. 2014; Sanquircé-García et al. 2016) and three instruments (Hoyland et al. 2012; Pérez-de-Taoro et al. 2016; Hoyland et al. 2022). The data used in this study come from the QUIJOTE-MFI wide survey, based on observations performed with the Multi-Frequency Instrument (MFI, Hoyland et al. 2012) between November 2012 and October 2018 (almost 9000 hr). The MFI consists of four polarimeters (called *horns*) in the bands 10–14 GHz (horns 1 and 3) and

**Table 3.** Band correlation measurements for the QUIJOTE-MFI maps. The second and third columns list correlation factors,  $\rho$ , for the pair of bands 11–13 GHz and 17–19 GHz, for the intensity and polarization maps.

Case	Intensity	polarization
$\rho_{11,13}$	0.77	0.36
$\rho_{17,19}$	0.85	0.29

16–20 GHz (horns 2 and 4). A detailed description of the QUIJOTE-MFI wide survey is presented in Rubiño-Martín et al. (2023) and Genova-Santos et al. (2023a).

The data are publicly available on the QUIJOTE web page<sup>4</sup>. We consider the available intensity ( $I$ ) and the linear polarization ( $Q$  and  $U$ ) maps smoothed to 1 deg (FWHM) which are centred at 11.1, 12.9, 16.8 and 18.8 GHz. Here, these are identified as Q11, Q13, Q17 and Q19 respectively. The Q11 and Q13 maps come from the MFI horn 3. However, the Q17 and Q19 maps are generated as a combination of data from two separate horns (horn 2 and horn 4) in order to reduce the  $1/f$  noise contribution (see details in Rubiño-Martín et al. 2023). The total calibration uncertainties are 5% for intensity and polarization, except for polarized maps Q17 and Q19, which reach a level of 6%. Regarding the zero levels and colour corrections, their effects are discussed in Section 3.4, and the noise correlations between bands and filtering scheme are discussed below.

For each horn, the signal is processed to produce two maps at different frequencies (e.g. Q11 and Q13 are obtained from horn 3), which share the same low-noise amplifier (LNA) configuration. These signals are therefore affected, to some degree, by a common  $1/f$  noise component, which is known as the QUIJOTE band correlation,  $\rho$ . The normalised correlation factors ( $\rho$ ) are around 80% in total intensity, and around 30% in polarization (owing to smaller  $1/f$  residuals), as discussed in detail in (Rubiño-Martín et al. 2023). In our analyses we account for this noise correlation by using the coefficients shown in Table 3.

One of the steps of the procedure to clean residuals radio frequency interference (RFI) involves the subtraction of the median of all pixels at the same declination. This template is called  $f(\delta)$  or FDEC and is applied in both intensity and polarization (see details in Rubiño-Martín et al. 2023; Genova-Santos et al. 2023a). As FDEC filtering acts as a low pass filter, we expect a low impact on the local flux density estimate using the photometric approach, which is the strategy applied here (Section 4). Rubiño-Martín et al. (2023) compares the polarized flux densities from maps with and without the FDEC, finding a negligible maximum difference of the two photometries of 0.4 Jy and a standard deviation of the difference of 0.037 Jy from different sky regions when the aperture size is 2 degrees. The results are lower for the case with apertures of 1 degree (a maximum difference of 0.06 Jy and a standard deviation of 0.007 Jy). Consequently, we use the QUIJOTE-MFI maps with the FDEC filtering applied, which is the standard data product. No FDEC filtering is applied to the remaining ancillary maps.

#### 3.2 Surveys at radio frequencies

At low frequencies, we use data from three well-known radio surveys of sufficient resolution to carry out a comprehensive analysis in combination with the QUIJOTE-MFI maps. These surveys have

<sup>3</sup> HEALpix: <http://healpix.jpl.nasa.gov>.

<sup>4</sup> QUIJOTE: <https://research.iac.es/proyecto/quijote>

effective frequencies centred at 408 MHz (Has map, Haslam et al. 1982), 820 MHz (Dwi map, Berkhuijsen 1971) observed with the Dwingeloo radio telescope, and 1420 MHz (Rei map, Reich & Reich 1986; Reich et al. 2001) from the Stockert 25 m telescope, whose original effective beam resolutions are 51, 72 and 34 arcmin respectively. In our analyses, the most relevant systematic effect is the calibration uncertainty. In this regard, in the determination of flux densities of point sources it must be taken into account that the 1.4 GHz map is calibrated to the full-beam scale, so that the calibration scale must be transferred to the main beam by using its efficiency. A scale factor of 1.55, proposed by Reich & Reich (1986), is required to account for this effect and has been widely used in previous studies (e.g. see discussions in Planck Collaboration et al. 2014; Irfan et al. 2015; Génova-Santos et al. 2017, and references therein). In this context, for each map, we assume a conservative calibration error of 15%, which will be added in quadrature to the flux density uncertainties.

### Galactic plane surveys

At 4.8 GHz, we use the Sino-German  $\lambda 6$  cm survey<sup>5</sup> of the Galactic plane (covering  $10^\circ < l < 230^\circ$  and  $|b| < 5^\circ$ ) produced with the 25 m Urumqi telescope (Sun et al. 2007; Gao et al. 2010; Sun et al. 2011a; Xiao et al. 2011). The intensity and polarization maps are publicly available from the CADE<sup>6</sup> webpage for the Urumqi dataset<sup>7</sup> in HEALPIX format ( $N_{\text{side}} = 1024$ ) at beam resolution of 9.5 arcmin. Since we smooth the maps to 1 deg (assuming the telescope beam to be Gaussian) the sky coverage of Urumqi is further restricted where we extended the original mask by 0.5 deg in order to avoid boundary effects in the smoothing process. We can only apply the photometric method of Section 4.1 to sources CTB 80, Tycho and HB 9. In contrast, HB 21 is partially observed while the Cygnus Loop and CTA 1 are outside of the observed region (at high latitudes). Sun et al. (2007) reported systematic errors from the calibration sources of around 4% and 5% for total intensity and polarized intensity respectively. In the estimation of flux densities, they computed a typical error lower than 10% in intensity and polarization, which was finally used as a global calibration uncertainty (10%) for the study of large SNRs seen by Urumqi (Gao et al. 2011; Sun et al. 2011b). Neither can we adopt to the estimation of flux density uncertainties with random aperture photometry (Section 4.1) because of the limited sky area observed. We therefore adopt a 10% uncertainty as a global calibration error.

### 3.3 Microwave and infrared surveys: WMAP, Planck and DIRBE

The WMAP (Wilkinson Microwave Anisotropy Probe, Bennett et al. 2013) and Planck (Planck Collaboration et al. 2020) missions provide  $I$ ,  $Q$  and  $U$  maps that are publicly available in LAMBDA<sup>8</sup> and in PLA<sup>9</sup> web pages respectively. The maps are in HEALPIX format, where both the original and smoothed (1 deg) versions are available. For WMAP, we consider the nine-year smoothed maps with

effective central frequencies of 22.8, 33.0, 40.6, 60.8 and 93.5 GHz. For Planck, we use the maps from the PR3-2018 data release. The nine bands cover from 28.4 to 857 GHz in total intensity and from 28.4 to 353 GHz in polarization (see effective central frequencies in Table 2). For WMAP and Planck, when working with intensity and polarized maps, we used a global calibration uncertainty of 3% (22.8–353 GHz), 6.1% (545 GHz) and 6.4% (857 GHz), which have been used previously in SED analyses that adopt the aperture photometry strategy (e.g. see Planck Collaboration et al. 2014; Génova-Santos et al. 2017; Poidevin et al. 2023; Fernández-Torreiro et al. 2023; Tramonte et al. 2023, and references therein). In addition, we consider the CMB map recovered with the SMICA algorithm (Planck Collaboration et al. 2020), which is also available in the PLA web page.

Finally, we consider the data product from the COBE-Diffuse Infrared Background Experiment (DIRBE, Hauser et al. 1998), which span the wavelength range from 1.25  $\mu\text{m}$  to 240  $\mu\text{m}$ . We use the far-infrared maps at 240  $\mu\text{m}$  (D10 at 1249 GHz), 140  $\mu\text{m}$  (D9 at 2141 GHz) and 100  $\mu\text{m}$  (D8 at 2997 GHz) available in LAMBDA<sup>8</sup>, which are useful for modelling the spectrum of the thermal dust emission in intensity. For these maps, we consider uncertainty levels of 11.6, 10.6 and 13.5 % respectively (Hauser et al. 1998).

### 3.4 Colour corrections and additional remarks

To correct our flux density estimates for the effect of finite bandwidth we apply a colour correction during the SED fitting (Section 4), which is estimated using the slope of the fitted spectrum at each frequency. In general, this redness is not negligible for experiments with broad bandpass receivers (QUIJOTE-MFI, WMAP, Planck and DIRBE), and when the spectral shape of the sources of interest departs from the shape of the spectrum of their calibrator.<sup>10</sup> Here, the colour correction coefficient,  $cc_\nu(\theta)$  at frequency  $\nu$ , is defined as a multiplicative factor applied to the raw flux density and to its uncertainty. The estimation of  $cc_\nu(\theta)$  depends on the non-ideal behaviour of detectors across the bandpass and the spectral shape of the source (identified by the parameter space  $\theta$  of the fitted spectrum).

This procedure requires the spectral integration over each bandpass for each model tested, which is computationally expensive and inefficient for our SED fit with the MCMC sampling approach (Section 4.2.2). Therefore, as an alternative, we use the FASTCC<sup>11</sup> code (Peel et al. 2022). FASTCC is optimized for several CMB experiments such as CBASS, QUIJOTE, WMAP, Planck and DIRBE. It provides the colour correction factors by evaluating a previously modelled quadratic function, assuming a power law behaviour (with spectral index  $\alpha$ ) across the bandpass. Optionally, for DIRBE and Planck-HFI bands, we use the dust temperature ( $T_d$ ) and emissivity index ( $\beta_d$ ) as input when our spectrum is dominated by a thermal dust component (see details in Peel et al. 2022). This is available for dust temperatures between 10 and 40 K and dust emissivity index between 1.0 and 4.0.

The uncertainties in the determination of the zero levels affect almost all the maps, although they are more significant in some surveys at the low frequencies. Nonetheless, the zero levels have a neg-

<sup>5</sup> <http://zmtt.bao.ac.cn/6cm/>

<sup>6</sup> Centre d'Analyse de Données Etendues (CADE, Paradis et al. 2012): <http://cade.irap.omp.eu>

<sup>7</sup> <https://cade.irap.omp.eu/dokuwiki/doku.php?id=urumqi>

<sup>8</sup> Legacy Archive for Microwave Background Data Analysis (LAMBDA): <http://lambda.gsfc.nasa.gov/>

<sup>9</sup> Planck Legacy Archive (PLA): <http://lambda.gsfc.nasa.gov/>

<sup>10</sup> In general, QUIJOTE, WMAP, Planck and DIRBE are calibrated using the CMB (mainly the dipole) or Galactic sources such as Tau A and Cas A (known as primary calibrators).

<sup>11</sup> FASTCC is available in IDL and Python language at <https://github.com/mp Peel/fastcc>.

**Table 4.** Aperture photometry parameters selected to our SNRs. In addition, CTB 80 and HB 21 include a mask to avoid strong Galactic diffuse emission and point sources (see text for details).

SNR	$l$ [deg]	$b$ [deg]	$r_{\text{src}}, r_{\text{int}}, r_{\text{ext}}$ [arcmin]	$\Omega_{\text{src}}$ [sr]
CTB 80	68.8	2.7	60, 80, 100	$9.51 \times 10^{-4}$
Cygnus L.	73.9	-8.8	130, 140, 170	$4.50 \times 10^{-3}$
HB 21	89.0	4.7	80, 100, 120	$1.43 \times 10^{-3}$
CTA 1	119.5	10.0	80, 100, 120	$1.70 \times 10^{-3}$
Tycho	120.1	1.4	60, 80, 100	$9.51 \times 10^{-4}$
HB 9	160.4	2.8	90, 100, 120	$2.15 \times 10^{-3}$

ligible effect on our flux density estimation, because the background correction applied by the photometric aperture method (Section 4) cancels them out. Therefore, we do not take into account the effects of zero levels.

Regarding polarization maps, we follow the COSMO convention used by WMAP, *Planck* and QUIJOTE-MFI, which differs from the IAU convention by the negative sign in the Stokes  $U$  maps (i.e.  $U = -U_{\text{IAU}}$ , Hamaker & Bregman 1996). Therefore, the Stokes  $U$  map at 4.8 GHz also includes the negative sign in accordance with the COSMO convention.

## 4 METHODOLOGY FOR SNR CHARACTERIZATION

This section presents the methodologies used to obtain the observational properties of SNRs, based mainly on the description and fitting of the spectral energy distribution, both in intensity and in polarization. We start with the estimation of integrated flux densities in intensity and polarization, followed by their modelling, which includes the implementation of the Markov Chain Monte Carlo (MCMC) approach for sampling the posterior distribution in a Bayesian framework. In addition, strategies to perform the rotation measure fit and achieve constraints on the intensity amplitude of the AME are also described.

### 4.1 Flux densities and uncertainties

The spectral energy distribution is determined by the flux densities observed for all frequency bands. Since the QUIJOTE-MFI maps (and most of the low-frequency ancillary maps) have effective resolutions of  $\lesssim 1$  deg, we are orientated towards the integrated properties of intensity and polarization signals. We therefore estimate the integrated flux densities in Stokes  $I$ ,  $Q$  and  $U$  maps on angular scales of 1 deg. For this purpose, we use the aperture photometry technique, which has the benefit of being robust against uncertainties in the beam or source shapes. In fact, this method is useful when the intensity and polarization spatial morphologies are different. Aperture photometry is a widely used technique (see implementations in López-Caraballo et al. 2011; Rubiño-Martín et al. 2012a; Génova-Santos et al. 2015b; Fernández-Torreiro et al. 2023, and references therein), where we computed the flux density from the integrated flux (the averaged temperature) inside a circular aperture  $r_{\text{src}}$  defining the solid angle of the source ( $\Omega_{\text{src}}$ ). The background emission in the line of sight is corrected by subtracting the median temperature in a circular corona (or ring) between radii  $r_{\text{int}}$  and  $r_{\text{ext}}$  with solid angle  $\Omega_{\text{bkg}}$ . The flux density uncertainty associated with this measurement is computed as the propagation of the standard deviation from the corona, also taking into account

the number of pixels in the source and background regions (see Génova-Santos et al. 2015b).

Table 4 shows the input parameters defining the source aperture and the background ring for each SNR. These parameters are the same for all the maps. They are selected to cover the entire SNR emission in intensity and polarization across all bands and to reduce the effects of prominent background structures. For instance, the apertures of Cygnus Loop are off-centre to avoid contamination from the Galactic plane in the northern region of the remnant (see Figure A2). Although this method provides an efficient correction of the background emission, two SNRs are contaminated by strong point or extended sources. For this reason, we apply a mask for HB 21 and CTB 80 in all the maps to avoid emission from two sources lying in the background region. The uncertainty estimator might also be biased owing to the high Galactic variation, large-scale correlated noise ( $1/f$  noise) or residual CMB contribution, mainly in sources covering large regions. Other alternatives, such as the selection of random control regions, are therefore explored to obtain a robust estimate of the errors.

#### 4.1.1 Random regions for uncertainty estimation

In general, our SNRs are relatively close to the Galactic plane in regions with diffuse Galactic emission that varies markedly with position (see Figures A1, . . . , A5 in Appendix A). Even the Cygnus Loop and CTA1, which are located at  $|b| > 5^\circ$ , show non-negligible background diffuse emission. In this situation, estimation of final errors from the pixel-to-pixel scatter is not straightforward and needs knowledge of the exact correlation of the noise. To have a more reliable assessment of the impact of background fluctuations on the noise, we have selected control regions in the neighbourhood of our SNR, taking care to (following López-Caraballo et al. 2011; Génova-Santos et al. 2015b; Poidevin et al. 2023; Tramonte et al. 2023) avoid zones with strong point or extended sources. We apply the photometry method in the random control regions of each SNR while taking into account the same apertures considered for that remnant (Table 4). The uncertainty arising from the diffuse background fluctuations is then estimated through the standard deviation of the flux densities extracted from the random control regions. Overall, the background fluctuation contribution to the error bar is significant for the  $I$  Stokes parameter with respect to the instrumental noise level, while its contribution is lower for Stokes  $Q$  and  $U$ . Note that this methodology cannot be applied to the 4.8 GHz maps because these are restricted to the Galactic plane.

#### 4.1.2 polarization measurements

The polarized SED is characterized via the integrated total linearly polarized intensities,  $P_\nu$ . First, we obtain the raw polarization intensity through the following expression:

$$P_{\text{raw},\nu} = \sqrt{Q_\nu^2 + U_\nu^2}, \quad (2)$$

where  $Q_\nu$  and  $U_\nu$  are the integrated flux densities from Stokes  $Q$  and  $U$  at frequency  $\nu$ . However, this raw polarization is affected by the positive noise bias (see Vaillancourt 2006; Rubiño-Martín et al. 2012a, and references therein). To obtain the true integrated polarization,  $P_\nu$ , a debiasing procedure is applied by using the Modified Asymptotic estimator (MAS, Plaszczyński et al. 2014):

$$P_\nu = P_{\text{raw}} - b^2 \frac{1 - e^{-P_{\text{raw}}^2/b^2}}{2P_{\text{raw}}} \quad (3)$$

where  $b = \sqrt{(Q_\nu \cdot \sigma_{U_\nu})^2 + (U_\nu \cdot \sigma_{Q_\nu})^2} / P_{\text{raw}}$ . From the debiased polarized measurement, we can compute the integrated polarization fraction via  $\Pi_\nu = 100 \times P_\nu / I_\nu$ . However, this calculation would be a biased estimate of the true polarization fraction, which becomes more pronounced when the signal-to-noise of the intensity estimate  $I_\nu$  is low. We should then apply debiasing of the quantity  $P_{\text{raw}} / I_\nu$ . To this aim we evaluate numerically, through Monte Carlo simulations, the probability density function of the true polarization fraction and integrate this curve to obtain the central value and confidence interval, as was done in [Génova-Santos et al. \(2017\)](#).

In addition, the apparent orientation of the projected polarization electric vector is described by the polarization angle:

$$\gamma_\nu = 0.5 \arctan(-U_\nu / Q_\nu), \quad (4)$$

where  $\arctan(\dots)$  represents the 4-quadrant inverse function providing angles between  $-\pi$  and  $\pi$ , where the quadrant is assigned according to the sign of the  $Q_\nu$  and  $U_\nu$  flux densities. In expression 4, the negative sign appears to maintain the meaning of  $\gamma$ , since the COSMO convention differs from the IAU convention ( $U = -U_{\text{IAU}}$ , [Hamaker & Bregman 1996](#)).

The flux densities from intensity and polarization are presented in Tables A1–A6 (Appendix A), where uncertainties are computed by random control apertures analysis (section 4.1.1). Overall, these measurements have not been colour corrected because this correction depends on the model considered (see section below). Note that the polarization intensity ( $P_\nu$ ) and the polarization fraction ( $\Pi_\nu$ ) correspond to the debiased measurements.

## 4.2 SED fitting procedure

### 4.2.1 SED Models

The spectral energy distributions of SNRs are dominated by synchrotron emission, which is the main component at low frequencies ( $\leq 100$  GHz). However, in the microwave range other physical mechanisms can be present, such as free–free, AME, thermal dust emission and a residual emission from CMB anisotropies. Some of these contributions arise as spurious emission in the line of sight (e.g. the CMB residual) while the rest can be associated with the SNR or their surrounding interstellar medium (such as free–free and thermal dust emissions), the presence (or not) of AME in our SNR sample being of particular interest. The strategy used to constrain the intensity amplitude of AME is presented in Section 4.4.

A preliminary analysis could determine whether the observed SEDs could be well fitted using a combination of synchrotron and thermal dust emission, where the former is associated with emission coming from the remnants and the latter is expected to be residual emission from the surrounding environment. Visual inspection of the SED (Figures 2–7) shows that the intensity signal appears to be dominated by synchrotron and thermal dust (low contribution) components, while the polarized signal is well modelled by one component (a synchrotron emission). In what follows, we describe the parametric representation of synchrotron and thermal dust emission, along with models proposed to fit the intensity and polarization SEDs in joint and separate analyses.

*Synchrotron emission.* The synchrotron radiation reflects the power-law energy spectrum of the relativistic particles responsible of the observed emission. Therefore, as usual, we consider the standard power-law function (labelled PL) with spectral index  $\alpha$  ([Pacholczyk 1970](#); [Rohlf 1990](#)):

$$S_{\text{syn}}(\nu; A_s, \alpha) = A_{\text{syn}} \left( \frac{\nu}{\nu_{\text{ref}}} \right)^\alpha, \quad (5)$$

where  $A_{\text{syn}}$  is the synchrotron amplitude at the reference frequency  $\nu_{\text{ref}}$ . This synchrotron parametric model is used in this paper, in both the intensity and polarization analyses, where the emission amplitude is normalised at  $\nu_{\text{ref}} = 11.1$  GHz in both cases.

The intensity SEDs of CTB 80 and HB 21 show evidence of a break in the synchrotron spectrum at low frequencies ( $\lesssim 5$  GHz), the spectral index being significantly steeper at high frequency. In these cases, there is no standard model for the SED characterization, a power law with an exponential cut-off function being one of the most frequently used models (e.g. [Pivato et al. 2013](#); [Loru et al. 2021](#); [Tramonte et al. 2023](#)). In our cases, the spectral change is noticeably abrupt and the spectra follow a power law below (radio frequencies) and above the break frequency, which is not so compatible with the gradual change of spectral indices described by the cut-off curve or Rolloff models (see Appendix B and Figure B1). We therefore consider a smooth broken power-law spectral model (SBPL):

$$S_{\text{syn}}^{\text{SBPL}}(\nu; A_{\text{syn}}, \alpha_{\text{bb}}, \alpha_{\text{ab}}, \nu_b, m) = A_{\text{syn}} \left( \frac{\nu}{\nu_{\text{ref}}} \right)^{\alpha_{\text{bb}}} \cdot \left( \frac{1 + (\nu/\nu_b)^m}{1 + (\nu_{\text{ref}}/\nu_b)^m} \right)^{\frac{\alpha_{\text{ab}} - \alpha_{\text{bb}}}{m}}, \quad (6)$$

where  $\alpha_{\text{bb}}$  and  $\alpha_{\text{ab}}$  are respectively the spectral indices below and above of the break frequency  $\nu_b$ . The synchrotron amplitude is normalised at  $\nu_{\text{ref}} = 11.1$  GHz. The  $m$  parameter determines the smoothing level of the spectral break. Since we have assumed  $m > 0$ , the sign of  $\Delta\alpha = \alpha_{\text{ab}} - \alpha_{\text{bb}}$  determines whether the spectrum is flatter ( $\Delta\alpha > 0$ ) or steeper ( $\Delta\alpha < 0$ ) after the spectral break. As  $m$  increases, the spectrum converges to the sharp shape of the Broken Power Law (BPL, equation B3) function (see Appendix B and Figure B1). In our implementation, the  $m$  value is fixed in order to have the same number of free parameters as in the BPL model (i.e.  $A_{\text{syn}}$ ,  $\alpha_{\text{bb}}$ ,  $\alpha_{\text{ab}}$  and  $\nu_b$ ). For HB 21 and CTB 80, we adopted a smooth broken power-law (SBPL) function with  $m = 10$ , because it provides close concordance between the SBPL and BPL spectral models, and is also in agreement with the smooth transition of the power laws observed for these remnants (see Appendix B).

*Thermal dust contribution.* It can be fitted by a single-temperature modified blackbody function assuming an optically thin scenario:

$$S_{\text{dust}}(\nu; \tau_{353}, T_d, \beta_d) = \tau_{353} \left( \frac{\nu}{353 \text{ GHz}} \right)^{\beta_d} \frac{2h\nu^3}{c^2 (e^{h\nu/kT_d} - 1)} \Omega_{\text{src}}, \quad (7)$$

where  $\tau_{353}$  is the optical depth at 353 GHz for the solid angle subtended by the aperture defining the source ( $\Omega_{\text{src}}$ ).  $\beta_d$  and  $T_d$  are the dust emissivity and dust temperature respectively.

Our estimates provide upper limits on the polarized flux densities for  $\nu \gtrsim 90$  GHz. These results are expected because the intensity of thermal dust emission is detected with low signal-to-noise. Therefore, this type of emission is not considered in the polarization SED modelling.

*Remarks on proposed models.* We have considered and implemented three fitting procedures based on intensity data only (INT), on polarization data only (POL) and on a combination of the two (INTPOL). The model for the INT fit case,  $m^{\text{int}}(\theta)$ , consists of synchrotron (in either the PL or the SBPL case) and thermal dust emissions, except for CTB 80 and CTA 1, where the thermal dust component is not included because measurements at frequencies higher than  $\sim 50$  GHz are noise dominated. Table 5 shows the model and parameter space  $\theta$  for each SNR. As an example, the model that is fitted to the intensity SED of HB 21 consists of the pa-

parameter space  $\theta_{\text{Int,HB21}} = \{A_{\text{syn}}, \alpha_{\text{bb}}, \alpha_{\text{ab}}, \nu_{\text{b}}, \tau_{353}, T_{\text{d}}, \beta_{\text{d}}\}$ , while CTA 1 is modelled with two parameters ( $\theta_{\text{Int,CTA1}} = \{A_{\text{syn}}, \alpha_{\text{bb}}\}$ ). In the case of the POL fit, the synchrotron emission is modelled with only the power-law function (PL) because the sampling of the polarized SED is limited. Since polarized measurements are available above 11.1 GHz (or above 4.8 GHz for two cases), we do not consider polarized spectral break behaviour for either CTB 80 or HB 21. Therefore, the proposed model is a power law,  $\theta_{\text{Pol}} = \{A_{\text{syn}}^{\text{pol}}, \alpha^{\text{pol}}\}$ , for each SNR (see bottom of Table 5).

Concerning the simultaneous intensity and polarization fit (INTPOL), we assume that synchrotron radiation has the same spectral behaviour in both intensity and polarization; e.g.  $\alpha^{\text{int}} = \alpha^{\text{pol}}$  in the power-law function case. Thus, the polarized synchrotron SED is written in terms of the intensity SED as  $S_{\text{syn}}^{\text{pol}} = \Pi_{\text{syn}} \cdot S_{\text{syn}}$ , where  $\Pi_{\text{syn}}$  is the polarization fraction of the synchrotron emission, on the assumption that  $\Pi_{\text{syn}}$  is constant. For instance, the model for HB 21 consists of intensity ( $m^{\text{int}} = S_{\text{syn}} + S_{\text{dust}}$ ) and polarized ( $m^{\text{pol}} = \Pi_{\text{syn}} \cdot S_{\text{syn}}$ ) components whose parameter space is  $\theta_{\text{IntPol,HB21}} = \{A_{\text{syn}}, \alpha_{\text{bb}}, \alpha_{\text{ab}}, \nu_{\text{b}}, \Pi_{\text{syn}}, \tau_{353}, T_{\text{d}}, \beta_{\text{d}}\}$ . For each SNR, Table 5 presents the intensity (int) and polarized (pol) components for the INTPOL case, as well as its space parameter  $\theta_{\text{IntPol}}$ .

#### 4.2.2 Likelihood analysis

For each model, the parameter space  $\theta$  is explored using a Markov Chain Monte Carlo (MCMC) analysis, which allows us to extract the parameters and uncertainties through marginalization of the posterior probability distribution function of each parameter. We used the publicly available affine-invariant MCMC sampler algorithm called EMCEE<sup>12</sup> (Foreman-Mackey et al. 2013), where the model is fitted to the data by maximizing the corresponding logarithmic posterior distribution:

$$\ln \left( \mathcal{L}(\theta) \prod_j \mathcal{P}(\theta_j) \right) \propto -\frac{1}{2} \chi^2(\theta) + \sum_j \ln(\mathcal{P}(\theta_j)), \quad (8)$$

where  $\mathcal{L}(\theta)$  is the likelihood and  $\mathcal{P}(\theta_j)$  corresponds to the prior distribution on the  $j$ -th parameter. Concerning priors, we impose positive top-hat priors<sup>13</sup> on amplitudes of our components, such as  $A_{\text{syn}}, A_{\text{syn}}^{\text{pol}}, \tau_{353}$  and  $\Pi_{\text{syn}}$ . For the synchrotron curved model, we set  $|\alpha_{\text{ab}} - \alpha_{\text{bb}}| \geq 0.1$  in order to avoid strong degeneracy. For the thermal dust, the priors on  $\beta_{\text{d}}$  and  $T_{\text{d}}$  are a proxy of the range available in the FASTCC (Section 3.4), yielding uniform priors  $\mathcal{P}(\beta_{\text{d}}) = \mathcal{U}(1.0, 4.0)$  and  $\mathcal{P}(T_{\text{d}}) = \mathcal{U}(10 \text{ K}, 40 \text{ K})$  respectively.

As we establish positive or uniform priors on parameters (Table 5), the maximization of posterior distribution, equation 8, is driven by the shape of the objective function  $\chi^2$ :

$$\chi^2 = (\mathbf{D} - \mathbf{m}(\theta))^T \mathbf{N}^{-1} (\mathbf{D} - \mathbf{m}(\theta)), \quad (9)$$

in which  $\mathbf{D}$  and  $\mathbf{m}(\theta)$  identify vectors with the raw flux densities and the model predictions for all frequencies respectively. In this equation,  $\mathbf{N}$  is the noise covariance matrix, whose inverse matrix ( $\mathbf{N}^{-1}$ ) must exist. We can now perform the characterization of the posterior distribution (equation 8). However, the colour correction

effects and the correlation between QUIJOTE-MFI bands are also elements that need to be taken into account.

*Colour correction.* As mentioned in Section 3.4, we use FASTCC<sup>11</sup> to compute the colour correction coefficients,  $cc_{\nu}(\theta)$ , which depend on the spectral shape of the SED. These are multiplicative factors applied to the flux densities and uncertainties of QUIJOTE, WMAP, *Planck* and DIRBE data. After factoring these into equation 9, they are included in the likelihood formalism as follows:

$$\chi^2 = \left( \mathbf{D} - \frac{\mathbf{m}(\theta)}{\mathbf{cc}(\theta)} \right)^T \mathbf{N}^{-1} \left( \mathbf{D} - \frac{\mathbf{m}(\theta)}{\mathbf{cc}(\theta)} \right), \quad (10)$$

where  $\mathbf{cc}(\theta)$  is the vector with colour correction factors for all frequencies. Note that  $cc_{\nu}(\theta) = 1$  when the colour correction is not applied, as in the case of low-frequency narrow-band surveys (Section 3.2). FASTCC provides accurate colour correction coefficients in our sample of SNRs as their spectra are reasonably well approximated by a power law. In fact, the differences between coefficients derived from FASTCC and from the exact integration on the bandpass are very small (lower than 1 %).

*QUIJOTE-MFI bands correlation.* For QUIJOTE-MFI measurements, this correlation between frequency bands leads to a non-diagonal noise matrix (Section 3.1). Therefore, the normalised correlation terms,  $\rho_{i,j}$ , from the pairs of bands (identified as  $i$  and  $j$ ) are non-negligible:

$$\begin{pmatrix} \sigma_i^2 & \rho_{i,j} \sigma_i \sigma_j \\ \rho_{j,i} \sigma_i \sigma_j & \sigma_j^2 \end{pmatrix} \quad (11)$$

where  $\rho_{j,i} = \rho_{i,j} \neq 0$  is assumed and  $\sigma_k$  is the flux density uncertainty measured in the  $k$  band. As discussed in Section 3.1, we take into account two cases,  $\rho_{11,13}$  at low frequency and  $\rho_{17,19}$  at high frequency, which have different values for intensity and polarization (see Table 3). Ideally, the noise is uncorrelated (i.e.  $\rho_{i,j} = 0 \forall i, j$ ) and the covariance noise matrix is diagonal; i.e.  $(\mathbf{N}^{-1})_{i,j} = \delta_{i,j} / \sigma_i^2$ , so the objective function  $\chi^2$  becomes:

$$\chi^2 = \sum_{i=1}^n \frac{(d_i - m_i(\theta) / cc_i(\theta))^2}{\sigma_i^2}, \quad (12)$$

which is the standard and simplest representation applied in SED fitting. In this equation,  $d_i$  and  $\sigma_i$  are the flux densities and uncertainties at the  $i$ -th frequency band.

For the INT and POL analysis, the objective functions follow equation 9 with the respective data and model; i.e. we have  $\chi_{\text{int}}^2(\theta_{\text{Int}})$  and  $\chi_{\text{pol}}^2(\theta_{\text{Pol}})$  separately for the intensity (INT) and the polarization (POL) fits respectively. The objective function for the INTPOL fit, however, is written in terms of the intensity and polarization objective functions as follows:

$$\chi^2(\theta_{\text{IntPol}}) = \chi_{\text{int}}^2(\theta_{\text{IntPol}}) + \chi_{\text{pol}}^2(\theta_{\text{IntPol}}), \quad (13)$$

which is minimized by the MCMC method, assuming that the intensity and polarized noises are uncorrelated. Overall, the spectral energy distributions presented throughout this paper are generated with colour-corrected flux densities coming from the INTPOL analysis (see Figures 2–7).

#### 4.2.3 Estimation of parameters

The characterization of the posterior distributions is performed by running EMCEE with 32 chains, although the iteration steps and the burn-in sample (first steps excluded of each chain) depend on the

<sup>12</sup> EMCEE is available at <https://emcee.readthedocs.io/en/stable/#>

<sup>13</sup> Positive priors are uniform priors,  $\mathcal{U}(a, b)$ , in the positive domain of the explored parameter, i.e.  $\mathcal{U}(0, \infty)$ .

**Table 5.** Models and parameter spaces considered for each SNR. Parametric models are presented in Section 4.2.1 and consist of  $S_{\text{syn}}$  (equation 5) and  $S_{\text{syn}}^{\text{SBPL}}$  (equation 6) for synchrotron,  $S_{\text{dust}}$  (equation 7) for thermal dust, and  $\gamma_{\text{PA}}$  (equation 14) for polarization angle.

INT	INTPOL
<b>HB 21</b> $S_{\text{syn}}^{\text{SBPL}}(A_{\text{syn}}, \alpha_{\text{bb}}, \alpha_{\text{ab}}, \nu_{\text{b}}, m = 10) + S_{\text{dust}}(\tau_{353}, T_{\text{d}}, \beta_{\text{d}})$ $\theta_{\text{INT}}: \{A_{\text{syn}}, \alpha_{\text{bb}}, \alpha_{\text{ab}}, \nu_{\text{b}}, \tau_{353}, T_{\text{d}}, \beta_{\text{d}}\}$	$\text{int}: S_{\text{syn}}^{\text{SBPL}}(A_{\text{syn}}, \alpha_{\text{bb}}, \alpha_{\text{ab}}, \nu_{\text{b}}, m = 10) + S_{\text{dust}}(\tau_{353}, T_{\text{d}}, \beta_{\text{d}})$ $\text{pol}: \Pi_{\text{syn}} \times S_{\text{syn}}^{\text{SBPL}}(A_{\text{syn}}, \alpha_{\text{bb}}, \alpha_{\text{ab}}, \nu_{\text{b}}, m = 10)$ $\theta_{\text{INTPOL}}: \{A_{\text{syn}}, \Pi_{\text{syn}}, \alpha_{\text{bb}}, \alpha_{\text{ab}}, \nu_{\text{b}}, \tau_{353}, T_{\text{d}}, \beta_{\text{d}}\}$
<b>CTB 80</b> $S_{\text{syn}}^{\text{SBPL}}(A_{\text{syn}}, \alpha_{\text{bb}}, \alpha_{\text{ab}}, \nu_{\text{b}}, m = 10)$ $\theta_{\text{INT}}: \{A_{\text{syn}}, \alpha_{\text{bb}}, \alpha_{\text{ab}}, \nu_{\text{b}}\}$	
<b>Cygnus Loop, HB 9 and Tycho</b> $S_{\text{syn}}(A_{\text{syn}}, \alpha) + S_{\text{dust}}(\tau_{353}, T_{\text{d}}, \beta_{\text{d}})$ $\theta_{\text{INT}}: \{A_{\text{syn}}, \alpha, \tau_{353}, T_{\text{d}}, \beta_{\text{d}}\}$	
<b>CTA 1</b> $S_{\text{syn}}(A_{\text{syn}}, \alpha)$ $\theta_{\text{INT}}: \{A_{\text{syn}}, \alpha\}$	
<b>POL</b> $S_{\text{syn}}(A_{\text{syn}}^{\text{pol}}, \alpha^{\text{pol}})$ $\theta_{\text{POL}}: \{A_{\text{syn}}^{\text{pol}}, \alpha^{\text{pol}}\}$	<b>POL. ANGLE</b> $\gamma_{\text{PA}}(\text{RM}, \gamma_0)$ $\theta_{\text{PA}}: \{\text{RM}, \gamma_0\}$

number of parameters of each case. For instance, the INTPOL analysis of HB21 (eight parameters) involves 30 000 iteration steps, with a *burn-in* sample of 3 500 steps. In order to obtain the parameters from the SED modeling, we marginalize the posterior distribution function over each parameter  $\theta_i$  to yield the PDF( $\theta_i$ ). The value of the parameter  $\theta_i$  is then computed as the median (the 50th percentile) of its PDF( $\theta_i$ ), while its associated uncertainty is obtained from the 16th and 84th percentiles. Table 6 reports the parameters and uncertainties obtained from the posterior distributions for the INT, POL and INTPOL fits of our SNR sample.

### 4.3 Modelling of the polarization angle

The multi-frequency characterization of the polarization angle provides information about the rotation measure. The RM is proportional to the product of the line-of-sight integral of the electron density and the parallel component of the magnetic field. In our case, we can recover a RM value across the whole SNR, which is obtained from modelling the multi-frequency polarization angles using the model:

$$\gamma_{\text{PA}}(\nu; \text{RM}, \gamma_0) = \gamma_0 + \text{RM} \left( \frac{c}{\nu} \right)^2, \quad (14)$$

where  $c$  is the speed of light in vacuo and  $\gamma_0$  corresponds to the intrinsic polarization angle (i.e. the observed angle for  $\nu \mapsto \infty$ ). The fitting procedure follows the MCMC approach described in Section 4.2.2, and we build the likelihood via equation 9. In this case, the colour correction factors have no effect, and, for simplicity, we do not consider the QUIJOTE-MFI band correlation.

### 4.4 Constraint on the AME intensity

The intensity spectral analysis provide no evidence of the AME component towards any of the six SNRs studied here. This is also supported by the low signal-to-noise detection of the intensity thermal dust emission. In addition, the inclusion of an AME component does not improve the modelling of the intensity spectra, and it sometime worsens the exploration of parameters with the MCMC procedure.

Notwithstanding, we are interested in constraining the intensity amplitude of AME for the six remnants. For this purpose, we have included an AME contribution in our SED fit and have decided to impose strong priors on all components. We consider the parametric description of the AME component (Stevenson 2014; Poidevin et al. 2023; Fernández-Torreiro et al. 2023) as follows:

$$S_{\text{AME}}(\nu; A_{\text{AME}}, \nu_{\text{AME}}, W_{\text{AME}}) = A_{\text{AME}} e^{-0.5(\ln(\nu/\nu_{\text{AME}})/W_{\text{AME}})^2}, \quad (15)$$

$A_{\text{AME}}$  being the AME amplitude at the peak frequency  $\nu_{\text{AME}}$ , and  $W_{\text{AME}}$  the width of the parabola in log–log space. This component is added to the SED fit of intensity (INT), where the parameters and uncertainties obtained in the case without AME (Table 6) are considered as Gaussian priors.<sup>14</sup> For example, we use a prior  $\mathcal{P}(\alpha) = \mathcal{N}(-0.5, 0.02)$  for the synchrotron spectral index of HB 9. For estimating the constraints on  $A_{\text{AME}}$ , we also impose the priors  $\mathcal{P}(\nu_{\text{AME}}) = \mathcal{N}(21 \text{ GHz}, 2 \text{ GHz})$  and  $\mathcal{P}(W_{\text{AME}}) = \mathcal{N}(0.7, 0.2)$  for the AME component. These values are consistent with a recent study

<sup>14</sup> A Gaussian prior follows the functional shape of a normal Gaussian distribution,  $\mathcal{N}(\bar{x}, \sigma_x)$ , described by the mean and standard deviation of the  $x$ -parameter.

**Table 6.** Results obtained from the characterization of the spectral energy distribution in intensity and polarization for the six SNRs: HB 21, CTB 80 (both with curved spectra), the Cygnus Loop, CTA 1, Tycho and HB 9. Three SED model approaches are performed: 1) only intensity measurements (INT), 2) only polarization measurements (POL) and 3) fitting simultaneous intensity and polarization measurements (INTPOL). The last is considered as our reference SED analysis. The models and parameter spaces are detailed in Table 5. For the POL approach,  $A_{\text{syn}}$  and  $\alpha$  represent  $A_{\text{syn}}^{\text{pol}}$  and  $\alpha^{\text{pol}}$  in Table 5. Parameters are estimated from the 50th percentile of the marginalized posterior distribution functions, while their uncertainties are estimated from the 16th and 84th percentiles.

	INTPOL	INT	POL	INTPOL	INT	POL		
			<b>CTB 80</b>					
$A_{\text{syn}}$ [Jy]	$21.0^{+1.1}_{-1.0}$	$20.9^{+1.2}_{-1.1}$	$0.8 \pm 0.1$	$58.1^{+2.5}_{-2.2}$	$56.1^{+2.2}_{-2.1}$	$3.2 \pm 0.2$		
$\Pi_{\text{syn}}$ [%]	$3.7 \pm 0.3$	-	-	$5.0 \pm 0.2$	-	-		
$\alpha_{\text{bb}}$	$-0.24^{+0.07}_{-0.06}$	$-0.27^{+0.06}_{-0.04}$	-	$-0.34^{+0.04}_{-0.03}$	$-0.33 \pm 0.04$	-		
$\alpha_{\text{ab}}$	$-0.60^{+0.04}_{-0.05}$	$-0.70^{+0.10}_{-0.12}$	$-0.52 \pm 0.07$	$-0.86^{+0.04}_{-0.05}$	$-0.80^{+0.04}_{-0.05}$	$-1.02 \pm 0.08$		
$\nu_b$ [GHz]	$2.0^{+1.2}_{-0.5}$	$3.7^{+1.2}_{-1.7}$	-	$5.0^{+1.2}_{-1.0}$	$4.0^{+1.1}_{-0.8}$	-		
$\tau_{353}$ [ $10^{-7}$ ]	-	-	-	$143.7^{+69.8}_{-52.5}$	$146.0^{+69.7}_{-53.2}$	-		
$T_d$ [K]	-	-	-	$12.5^{+2.6}_{-1.7}$	$12.2^{+2.4}_{-1.6}$	-		
$\beta_d$	-	-	-	$2.0 \pm 0.5$	$2.2 \pm 0.5$	-		
$\chi_{\text{dof}}^2$	1.83	2.24	0.70	0.63	0.47	0.54		
			<b>Cygnus Loop</b>					
$A_{\text{syn}}$ [Jy]	$44.6^{+1.0}_{-1.1}$	$44.6 \pm 1.0$	$2.9^{+0.6}_{-0.5}$	$8.9 \pm 0.6$	$9.0 \pm 0.6$	$1.0 \pm 0.2$		
$\Pi_{\text{syn}}$ [%]	$6.0 \pm 0.4$	-	-	$9.4^{+1.2}_{-1.1}$	-	-		
$\alpha$	$-0.47 \pm 0.02$	$-0.47 \pm 0.02$	$-0.59 \pm 0.23$	$-0.50 \pm 0.03$	$-0.50 \pm 0.03$	$-0.84^{+0.29}_{-0.27}$		
$\tau_{353}$ [ $10^{-7}$ ]	$27.3^{+9.3}_{-7.1}$	$27.3^{+9.2}_{-7.2}$	-	-	-	-		
$T_d$ [K]	$15.8^{+2.1}_{-2.0}$	$15.8 \pm 2.1$	-	-	-	-		
$\beta_d$	$1.8^{+0.4}_{-0.3}$	$1.8^{+0.4}_{-0.3}$	-	-	-	-		
$\chi_{\text{dof}}^2$	0.63	0.59	0.75	0.39	0.25	0.45		
			<b>Tycho</b>					
$A_{\text{syn}}$ [Jy]	$12.9 \pm 0.6$	$12.9 \pm 0.6$	$0.1^{+0.2}_{-0.1}$	$20.6 \pm 0.7$	$20.7 \pm 0.7$	$1.4 \pm 0.1$		
$\Pi_{\text{syn}}$ [%]	$0.0^{+1.5}_{-1.6}$	-	-	$6.9 \pm 0.5$	-	-		
$\alpha$	$-0.60 \pm 0.02$	$-0.60 \pm 0.02$	$-1.57^{+1.29}_{-1.35}$	$-0.51 \pm 0.02$	$-0.50 \pm 0.02$	$-0.60 \pm 0.08$		
$\tau_{353}$ [ $10^{-7}$ ]	$119.3^{+28.3}_{-24.8}$	$119.6^{+28.3}_{-24.8}$	-	$82.0^{+22.2}_{-16.9}$	$82.1^{+23.0}_{-16.9}$	-		
$T_d$ [K]	$14.7^{+1.4}_{-1.3}$	$14.6^{+1.4}_{-1.3}$	-	$14.9^{+1.6}_{-1.7}$	$14.8^{+1.6}_{-1.7}$	-		
$\beta_d$	$2.2^{+0.4}_{-0.3}$	$2.2^{+0.4}_{-0.3}$	-	$1.5 \pm 0.3$	$1.5 \pm 0.3$	-		
$\chi_{\text{dof}}^2$	0.45	0.69	0.02	0.44	0.23	0.76		
			<b>CTA 1</b>					
			<b>HB 21</b>					
			<b>HB 9</b>					

of AME in the Galactic plane (using QUIJOTE-MFI data at scales of 1 deg, Fernández-Torreiro et al. 2023) and also span the AME parameters obtained for the SNRs W44, W41 and W51 (Génova-Santos et al. 2017; Tramonte et al. 2023). The upper limits on the AME amplitude are presented in Table 8 and their impact on the presence of AME on SNRs is discussed in Section 5.7.3.

## 5 RESULTS AND DISCUSSION

In this section we discuss in detail the integrated SED in intensity and in polarization for our sample of SNRs. The obtained properties presented in Table 6 correspond to modelling the SEDs with the three proposed approaches called INT (only intensity data), POL (only polarization data) and INTPOL (simultaneously fitting the intensity and polarization data). We use the results of the INTPOL fit as a reference. In addition, we discuss the statistical properties of the SNRs, such as the contribution of the AME mechanism in the SNR scenario on a scale of 1 deg. In our statistical studies (section 5.7), we combine our results for these six objects with those obtained in other QUIJOTE publications for other SNRs.

### 5.1 SED of CTB 80

The complex morphology of CTB 80 at radio frequencies (central nebula, plateau and arms) is diluted into the 1 deg scale resolution, yielding only an extended structure (in intensity signal) well covered by an aperture of radius of  $\sim 1$  deg (see Figure A1 and Table 4). CTB 80 is located on the north-east edge of the Cygnus area, where extended diffuse emission covers the field of view. In addition, a source with a strong intensity signal lies partly in the external ring that we use for background subtraction. This source is masked with a circular aperture of radius 0.9 deg centred at  $l = 70.2$  deg and  $b = 1.55$  deg (see Figure A1). Table A1 lists the flux densities of CTB 80. In intensity, the spectrum is dominated by synchrotron emission with a spectral break at frequencies lower than the QUIJOTE bands (first evidence from Sofue et al. 1983; Gao et al. 2011; Castelletti & Dubner 2005). Spurious thermal dust emission is negligible; in fact, for  $\nu \gtrsim 70$  GHz only upper limits (on flux densities) are computed from Table A1. We also consider literature measurements in order better to characterize the curved shape of the intensity SED, although this procedure must be treated carefully because of the wide range of systematic effects of each measurement (see Appendix C). We do not take into ac-

count measurements below 200 MHz in order to avoid the possible low frequency spectral turnover generated by the free-free thermal self-absorption (proposed by [Castelletti & Dubner 2005](#)), which is still debated on the basis of the inconsistency with the low level of dispersion reported for PSR B1951+32 ([Gao et al. 2011](#); [Hobbs et al. 2004](#)). Low-frequency flux densities are listed in Appendix C and identified by blue diamonds in Figure 2. Nevertheless, the data dispersion is high at low frequencies, which is also observed in our measurements. At 0.408 and 0.82 GHz, we measure  $109 \pm 13$  and  $47.1 \pm 7.1$  Jy. These are the highest and lowest measurements in the ranges 0.3–0.5 GHz and 0.7–1.0 GHz respectively. Regarding the map at 0.8 GHz, one explanation may be connected to the fact that the apertures are optimized for a beam of 1 deg while the map has a beam resolution of 1.2 deg. At 11.1 GHz, we obtain a raw flux density of  $21.5 \pm 3.4$  Jy, which is in agreement with the  $18.8 \pm 1.3$  Jy at 10.2 GHz reported by [Sofue et al. \(1983\)](#). Despite the high dispersion of the data, we decided to use measurements from the literature in order to be consistent with the analysis performed for the other SNR with a curved spectrum (HB 21, Section 5.3). In polarization, it is not possible to trace an eventual break, since the polarized spectrum lacks data at low frequency. We then consider a single power-law synchrotron component for the POL fit. Finally, we use frequencies only up to 100 and 60.7 GHz bands for intensity and polarization SEDs respectively. Figure 2 shows the intensity and polarization SEDs, including upper limits, of CTB 80 for the INTPOL analysis.

In the intensity SED description, the INTPOL and INT analyses provide good agreement for the synchrotron amplitude at 11.1 GHz ( $21 \pm 1$  Jy) and the spectral index before the break ( $-0.24 \pm 0.07$  and  $-0.27 \pm 0.06$ ). When these are compared with previously reported values such as  $-0.36 \pm 0.02$  ([Castelletti & Dubner 2005](#)),  $-0.45 \pm 0.03$  ([Kothes et al. 2006](#)) and  $-0.38 \pm 0.13$  (using flux densities at 6, 11 and 21 cm from [Gao et al. 2011](#)), we found that the largest discrepancy is at  $2.6\sigma$ . This discrepancy is understood to be due to the wide dispersion of flux densities at low frequencies and to some studies using data at frequencies lower than 200 MHz. In that case, when all the flux densities at low frequencies are taken into account (including  $\lesssim 200$  MHz), we found that the INTPOL and INT results were in full agreement. However, we recover a flatter  $\alpha_{bb}$  and lower  $\nu_b$ ; e.g.  $-0.10 \pm 0.06$  and  $1.5 \pm 0.3$  GHz for the INTPOL analysis, although it is performed with a similar  $\chi^2_{\text{dof}}$  of 1.86. This  $\alpha_{bb}$  around  $-0.1$  therefore disagrees significantly from previous studies ([Castelletti & Dubner 2005](#); [Kothes et al. 2006](#)). Note that, our results provide  $A_{\text{syn}} \approx 21$  Jy and  $\alpha_{ab} \approx -0.6$  that remain stable in spite of the model and the low-frequency data set considered, which is to be expected because these two parameters characterize the microwave SED (the QUIJOTE-MFI frequencies and higher).

The INT fit yields an asymmetric marginalized PDF for  $\nu_b$  and  $\alpha_{ab}$  (and also higher uncertainties for  $\nu_b$  and  $\alpha_{ab}$ ) with respect to the INTPOL case. The PDF of  $\nu_b$  shows a bimodal distribution peaking at  $\sim 2$  and  $\sim 4$  GHz. This also affects the  $\alpha_{ab}$  characterization, whose marginalized PDF yields  $-0.70^{+0.10}_{-0.12}$ , reaching maximum at around  $-0.62$  (which agrees with  $\alpha_{ab} = -0.60 \pm 0.05$  from the INTPOL). Even so, the  $\alpha_{ab}$  and  $\nu_b$  are consistent at  $1\sigma$  between the INTPOL and INT analyses. Although our estimates of the spectral index in the microwave range,  $-0.70^{+0.10}_{-0.12}$  and  $-0.60 \pm 0.05$ , are not compatible with the approximate spectral index of  $-0.8$  inferred at 30 and 44 GHz ([Planck Collaboration et al. 2016a](#)), our approach is the first SED fit to leave  $\nu_b$  and  $\alpha_{ab}$  as free parameters.

We confirm the curved shape of CTB 80 inferred by [Sofue et al. \(1983\)](#) and [Planck Collaboration et al. \(2016a\)](#), where our models show the spectral break to occur between 1.5 and 4 GHz (most

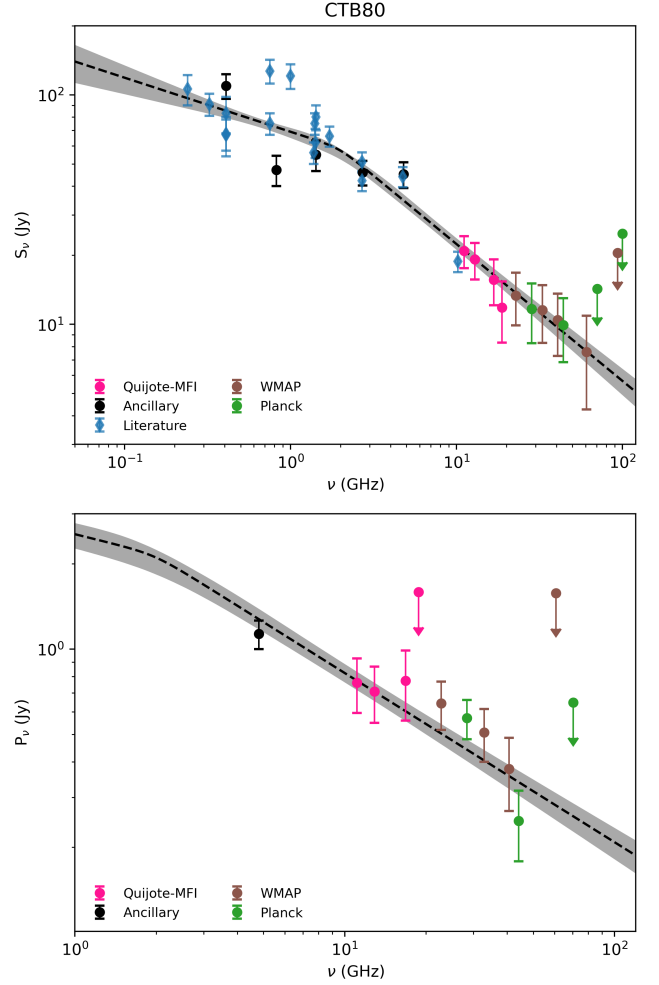


**Figure 2.** Spectral energy distribution of CTB 80 in intensity (top panel) and polarization (bottom panel). The integrated flux densities coming from different data sets are identified with colours. The blue diamonds are low frequency intensity flux densities from the literature (see Appendix C). The dashed line corresponds to the SED model obtained from INTPOL analysis (Table 6), while grey shading represents its uncertainties.

probably at  $2^{+1.2}_{-0.5}$  GHz) with a radio spectral index between  $-0.1$  and  $-0.3$ <sup>15</sup> and a microwave spectral index of  $\alpha_{ab} = -0.6 \pm 0.5$ . The spectral break  $\Delta\alpha$  estimates are  $-0.34 \pm 0.07$  and  $-0.43 \pm 0.12$  for INTPOL and INT respectively. The former value departs from the prediction,  $\Delta\alpha = -0.5$ , of synchrotron losses in a homogeneous source with a continuous injection of electrons ([Reynolds 2009](#)), while the latter,  $-0.43 \pm 0.12$ , could be ascribed to the mechanism expected for a pulsar wind nebula ([Reynolds 2009](#)).

Regarding polarization properties, we recover a polarization fraction  $\Pi_{\text{syn}} = 3.7 \pm 0.3\%$  and a spectral index  $\alpha_{ab} = -0.60^{+0.04}_{-0.05}$  for the INTPOL analysis. For comparison, the polarized spectrum is described by a single power law with spectral index  $\alpha^{\text{pol}} = -0.52 \pm$

<sup>15</sup> For this range, the particle spectral index  $\Gamma_p$  falls in the range of 1.2 and 1.6, which is in agreement with the value of 1.72 used to model the leptonic contribution of the non-thermal emission at high energy ([Araya & Herrera 2021](#)). Note that they took into account the radio spectral index  $\alpha = -0.36 \pm 0.02$  reported by [Castelletti & Dubner \(2005\)](#).

0.08 and amplitude  $A_{\text{syn}}^{\text{pol}} = 0.8 \pm 0.1 \text{ Jy}$  (POL fit). This polarized spectral index, it will be recalled, is expected to be equivalent to  $\alpha_{\text{ab}}$  from the INTPOL fit. We find that  $\alpha^{\text{pol}}$  is flatter than the other two cases using intensity data, with differences of 0.08 (at  $1\sigma$ ) and  $-0.18$  (at  $1.4\sigma$ ) with respect to INT and INTPOL respectively. This flattening could suggest depolarization between Urumqi band and microwave frequency bands, or that the intensity and polarization spectral indices are different. However, the polarized SED from INTPOL (Figure 2) shows a suitable model of the SED. Also, we observe a slight dip between the WMAP/Planck (23–33 GHz) and QUIJOTE-MFI (11–13 GHz) bands. However, the uncertainties in the measured flux densities prevent more accurate modelling. As a consistency test, the polarization fraction  $\Pi_{\text{syn}}^{\text{pol,int}} = 3.8 \pm 0.4\%$ , computed from the intensity and polarization amplitudes of the INT and POL analyses, is in agreement with the  $\Pi_{\text{syn}} = 3.7 \pm 0.3\%$  for the INTPOL case. This reveals that the polarization fraction at 11.1 GHz is a reliable estimate, regardless of the model. In addition,  $\Pi_{\text{syn}}$  is unaffected by the different intensity low frequency data set considered in previous intensity analyses.

The polarization degree  $\Pi_{\text{syn}} = 3.7 \pm 0.3\%$  appears to be in disagreement with the high level reported in CTB 80, where the averaged polarization fractions reported are  $13.2 \pm 2.0\%$ ,  $12^{+10}_{-6}\%$  and  $7.6 \pm 0.7\%$  at 4.7, 2.73 and 1.42 GHz respectively (Mantovani et al. 1985; Castelletti & Dubner 2005; Gao et al. 2011). However, literature measurements obtained using maps with higher resolutions and the polarization levels are provided at pixel scales. In contrast, we integrate  $Q$  and  $U$  in our aperture and derive the polarized intensity from those integrated quantities (Eq. 2), so our results are more prone to depolarization effects. A straightforward comparison is therefore not possible.

## 5.2 SED of the Cygnus Loop

At an angular resolution of 1 deg, the Cygnus Loop appears as a complex region with well-defined edges of diffuse plateau emission. Two extended structures can be clearly distinguished (see the intensity map in Figure A2). The smallest one is associated with the NGC 6992/5 regions (west region), while the main component (eastern region) predominantly encompasses the southern shell, NGC 6960, the central filament and the remaining structures in the north (regions mentioned in Section 2.1). These two regions are separated by an unpolarized canal, which is more noticeable at 22.8 and 28.4 GHz (WK and P30 bands), as seen in the  $P$  map in Figure A2. In addition, the polarization angle distribution shows differences up to  $45^\circ$  between the NGC 6992/5 regions and the rest of the remnant. This morphology is compatible with observations at lower frequencies and higher angular resolution, where weak diffuse polarized emission is observed between these two areas of the SNR (e.g. see polarization maps in Leahy et al. 1997; Uyaniker et al. 2002; Sun et al. 2006).

Even though the Cygnus Loop is far enough from the Galactic plane, we observe Galactic diffuse emission in the northern part of our apertures, mainly affecting the intensity signal at high frequencies (see Figure A2). Note that the central position of apertures is selected to reduce this contamination (Table 4). Nonetheless, the intrinsic intensity emission of Cygnus Loop is negligible for frequencies  $\geq 100$  GHz. Its large size, however, requires a large aperture ( $r_{\text{src}} = 130$  arcmin), where the CMB residuals become more important. Therefore, we subtract the SMICA-CMB map from the Planck collaboration, which traces the CMB anisotropies (see Section 3.3). The raw (CMB-subtracted) flux densities for the whole

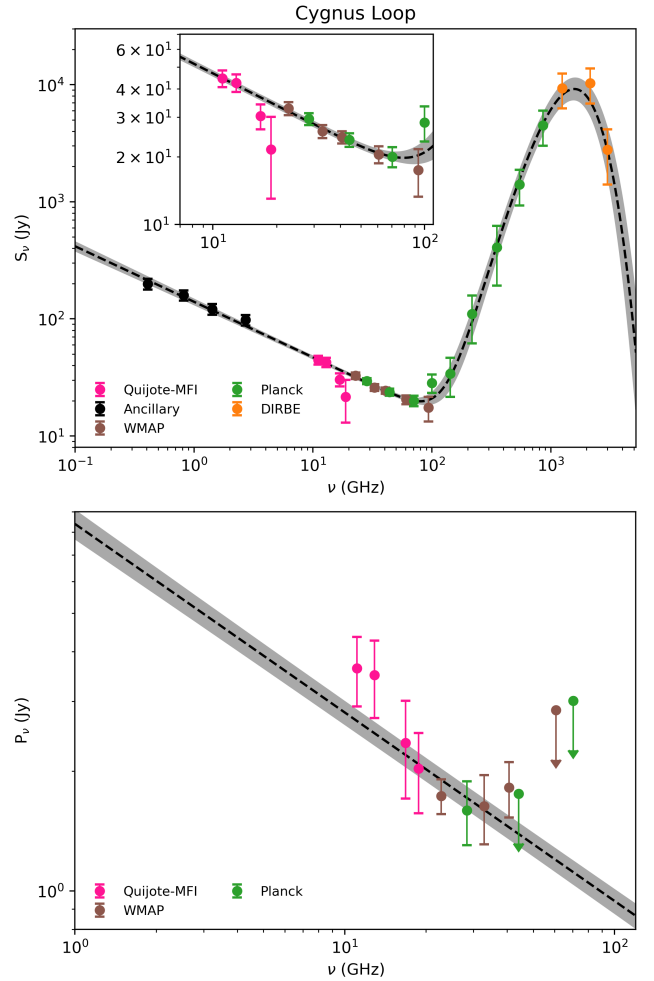


**Figure 3.** Spectral energy distribution of Cygnus Loop in intensity (top panel) and in polarization (bottom panel). The integrated flux densities coming from different data sets are identified by colour. The dashed line corresponds to the SED model obtained from the INTPOL analysis (Table 6), while grey shading represents its uncertainties.

Cygnus Loop are listed in Table A2. At 11.1 GHz, we obtain an intensity flux density of  $46 \pm 4 \text{ Jy}$ , which is in agreement with the value extrapolated (using  $\alpha = -0.53$ ) from the flux density measured at 8.5 GHz ( $54 \pm 4 \text{ Jy}$ ) with the Medicina telescope (Loru et al. 2021). The intensity signal is well described by a power-law spectrum characteristic of synchrotron emission (below 100 GHz), while the observed thermal dust emission probably arises from Galactic background emission. In polarization, we consider only one component associated with synchrotron emission and use measurements at frequencies lower than 80 GHz. In Figure 3, we show the intensity and polarization SEDs, including constraints, of the Cygnus Loop for the INTPOL case.

In intensity, we find a synchrotron amplitude at 11.1 GHz of  $44.6 \pm 1.0 \text{ Jy}$  and a spectral index of  $\alpha = -0.47 \pm 0.02$ , since INT and INTPOL yield the same parameter values, with the only difference being in the  $\chi^2_{\text{dof}}$  values (0.59 and 0.62 respectively). We also detect a weak thermal dust component associated with the background emission (with a  $\tau_{353}$  significance of  $3.8\sigma$ ), which is supported by the morphology observed at high frequencies (see, for example, the

map at 217 GHz in Figure A2). Our synchrotron spectral index falls in the range of  $-0.40$  to  $-0.53$  reported in previous studies (e.g., see Uyaniker et al. 2004; Sun et al. 2006; Planck Collaboration et al. 2016a; Loru et al. 2021), with differences of  $2.7\sigma$  in the worst case. For instance, recently, Loru et al. (2021) obtained  $\alpha = -0.53 \pm 0.01$  in the frequency range 0.022–30 GHz. In addition, Loru et al. (2021) modelled an exponential cut-off providing the spectral index  $\alpha = -0.51 \pm 0.02$  with a cut-off frequency  $\nu_c = 172 \pm 117$  GHz, setting a weak restriction on the curvature of the spectrum, which becomes compatible with our power-law model for frequencies lower than 100 GHz. In another analysis, Sun et al. (2006) reported a flatter spectral index ( $\alpha = -0.40 \pm 0.06$ ) fitting only five bands in the range of 0.408–4.8 GHz, a frequency range that is comparable with our lower-frequency data set. Our synchrotron model is therefore reliable and the low flux densities measured in the Q17 and Q19 bands do not affect the fit since their uncertainties are conservative.

The polarized emission is described by a single power law spectrum up to around 30 GHz, and beyond that frequency our measurements are compatible with zero. The INTPOL characterization provides a polarization fraction of  $\Pi_{\text{syn}} = 6.0 \pm 0.4\%$ . This polarized SED model predicts flux densities lower than observed in the Q11 and Q13 bands, although these are inside the  $1\sigma$  level when uncertainties are taken into account (see bottom panel in Figure 3). This effect is small because the INTPOL, INT and POL analyses provide coherent results. In fact, the  $\Pi_{\text{syn}}$  value agrees with the polarization fraction  $\Pi_{\text{syn}}^{\text{pol,int}} = 6.5 \pm 1.4\%$ , where the latter is computed with amplitudes from the INT and POL fits. In contrast, the spectral index  $\alpha^{\text{pol}} = -0.59 \pm 0.23$  (from the POL analysis) differs by 0.12 with respect to the value found in the INTPOL case, although they are compatible at  $0.5\sigma$ . As for CTB 80, our integrated polarization fraction cannot be compared directly with values reported in the literature owing to the different methodologies and angular resolutions. At 4.8 GHz, the average polarization degree reaches levels of 30% and 20% around NGC 6992/5 and the southern shell respectively (Sun et al. 2006; Kundu & Becker 1972). In our  $Q$  and  $U$  maps at 1 deg, the polarization is mainly observed in the eastern region (the main component) while it is weaker towards the NGC 6992/5 region. For instance, in the Q11 and Q13 bands, the emission from NGC 6992/5 becomes indistinguishable from noise or background contamination (see the  $P$  map in Figure A2).

### 5.3 SED of HB 21

HB 21 is located on the north-eastern edge of the Cygnus X area, and its radio emission appears to be superimposed on surrounding extended diffuse emission. In the high-frequency range, where the synchrotron emission is below noise level, our default aperture lead to negative flux densities. This is a consequence of the thermal dust emission being brighter in the background ring than in the aperture. In order to avoid this spurious emission, we use a mask to exclude part of the southern part of our background annulus (see Figure A3). The flux densities extracted from the masked maps are then listed in Table A3. At 22.8 GHz, we measure  $32.6 \pm 2.5$  Jy in intensity, which agrees with the  $34 \pm 3$  Jy value obtained by Pivato et al. (2013) in the same band. For the SED analyses, the intensity signal is described by a synchrotron component with a smooth broken spectral behaviour and thermal dust emission, while the polarization signal is well characterized by the synchrotron component only (see models in Table 5). The thermal dust component is considered to be due to background emission. Similarly to CTB 80, fitting the synchrotron with a spectral break represents a challenge owing

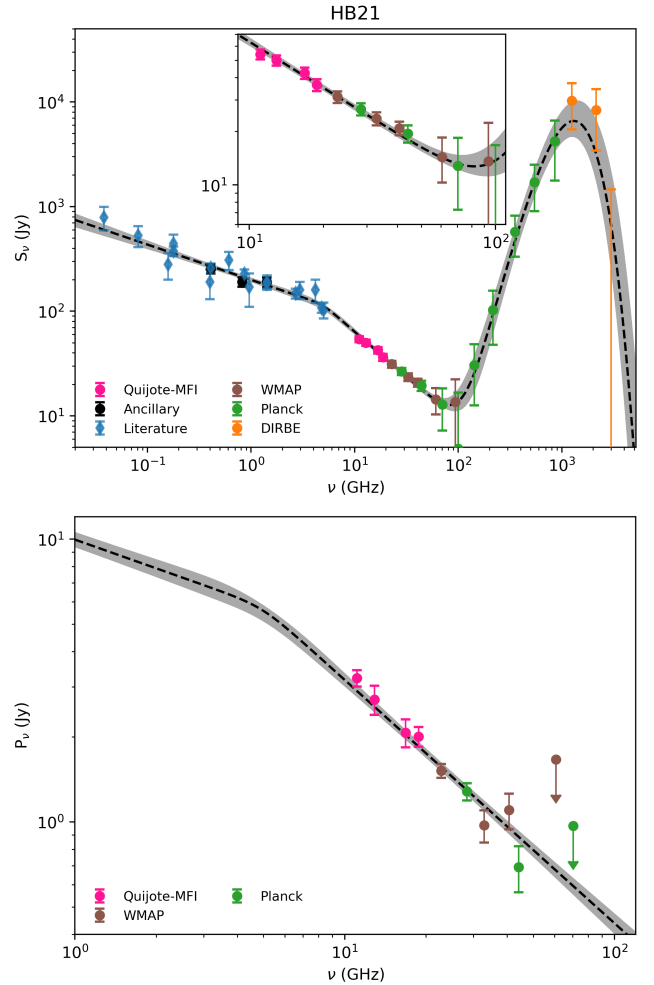


**Figure 4.** Spectral energy distribution of HB 21 in intensity (top panel) and polarization (bottom panel). The integrated flux densities coming from different data sets are identified by colour. The blue diamonds are low-frequency intensity flux densities from the literature (see Appendix C). The dashed line corresponds to the SED model obtained from INTPOL analysis (Table 6), while grey shading represents its uncertainties.

to our low number of measurements at low frequencies, which strongly affects the estimation of  $\nu_b$ . We therefore use literature data available for  $\nu \leq 10$  GHz (see details in Appendix C). In addition, the polarized measurements at high frequency,  $\nu \gtrsim 100$  GHz, are noise dominated, so that we only consider polarized flux densities up to 70.4 GHz (P70 band). The polarization from the 60.7 and 70.4 GHz frequencies are upper limits. Figure 4 shows the modelled SEDs in intensity and in polarization from the INTPOL approach.

For the intensity signal, the INTPOL and INT approaches provide similar results for the synchrotron component (see Table 6), whose parameters agree within the uncertainties. We obtained amplitudes normalised at 11.1 GHz of  $58.1^{+2.5}_{-2.2}$  Jy and of  $56.1^{+2.2}_{-2.1}$  Jy, and spectral indices below the spectral break of  $-0.34^{+0.04}_{-0.03}$  and  $-0.33 \pm 0.04$  for INTPOL and INT respectively. The largest differences, although still inside the 1-sigma level, are found for the spectral index after the break ( $\alpha_{\text{ab}}$ ) and the break frequency ( $\nu_b$ ). The fit provides steeper  $\alpha_{\text{ab}}$  ( $-0.86^{+0.04}_{-0.05}$ ) and higher  $\nu_b$  ( $5.0^{+1.2}_{-1.0}$  GHz) values when polarization and intensity signals are analysed together, in contrast to the

intensity-only analysis ( $\alpha_{\text{ab}} = -0.80^{+0.04}_{-0.05}$  and  $\nu_{\text{b}} = 4.0^{+1.1}_{-0.8}$  GHz). Although the spectral break has already been reported in previous studies (e.g, Pivato et al. 2013; Planck Collaboration et al. 2016a), this is the first study in which the spectral indices and  $\nu_{\text{b}}$  are modelled as free parameters. Using low-frequency and WMAP data, Pivato et al. (2013) assumed a sudden spectral break of  $\Delta\alpha = -0.5$  to recover a radio spectral index of  $\alpha = -0.38 \pm 0.02$ , (equivalent to our  $\alpha_{\text{bb}}$ ) and  $\nu_{\text{b}} = 5.9 \pm 1.2$  GHz. Regarding the break frequency, our derived results are lower than those of Pivato et al. (2013), where INTPOL gives the closest value ( $\nu_{\text{b}} = 5.0^{+1.2}_{-1.0}$  GHz). For the radio spectral index, we obtained a steeper index ( $-0.34 \pm 0.04$ ). This provides a particle spectral index of  $1.68 \pm 0.08$ , which is also in agreement with the  $\Gamma_{\text{p}} = 1.67 \pm 0.02$  reported by Pivato et al. (2013). In addition, we compute the spectral break,  $\Delta\alpha = \alpha_{\text{ab}} - \alpha_{\text{bb}}$ , of  $-0.52 \pm 0.06$  and  $-0.47 \pm 0.06$  for INTPOL and INT respectively. These values are in good agreement with the reference  $\Delta\alpha = -0.5$  expected for middle-aged SNRs with synchrotron losses in a homogeneous source with continuous injection of electrons (Reynolds 2009).

Regarding the polarization properties, we recover a polarization fraction  $\Pi_{\text{syn}} = 5.0 \pm 0.2\%$  and a spectral index  $\alpha_{\text{ab}} = -0.80^{+0.04}_{-0.05}$  in QUIJOTE-MFI (and higher) frequencies (INTPOL analysis). For the POL case, the polarized spectrum is described by a single power law with spectral index  $\alpha^{\text{pol}} = -1.02 \pm 0.08$  and amplitude  $A_{11.1}^{\text{pol}} = 3.2 \pm 0.2$  Jy. This spectral index of polarization is steeper than the other two cases using the intensity measurements ( $\alpha_{\text{ab}}$ ), where we have a difference of  $-0.22$  (at  $2.3\sigma$ ) and  $-0.16$  (at  $1.7\sigma$ ) for INT and INTPOL respectively. Concerning the polarization level, the polarization fraction from amplitudes obtained in INT and POL,  $\Pi_{\text{syn}}^{\text{pol,int}} = 5.7 \pm 0.4\%$ , is in agreement with  $\Pi_{\text{syn}} = 5.0 \pm 0.2\%$  for the INTPOL case. Although a straightforward comparison is not possible, as mentioned for previous SNRs these polarization fractions are smaller than the average polarization fraction of  $10.7 \pm 1.1\%$  at 4.8 GHz (Gao et al. 2011) and  $3.7 \pm 0.5\%$  at 1.42 GHz (Kotthes et al. 2006) reported previously.

#### 5.4 SED of CTA 1

At a resolution of 1 deg, the intensity signal of CTA 1 appears as an extended source where the emission from the shell, from the central branch and the breakout region, are diluted as a result of the coarse angular resolution (Figure A4). There is a small diffuse region to the north-west that is associated with two extragalactic point sources and part of the diffuse emission coming from the western shell. We also keep in mind the Faraday Screen (FS) reported by Sun et al. (2011a), which is located at  $(l, b) = (121^\circ, 11^\circ)$  with an approximated radius of  $1.5^\circ$ . Part of the FS covers the western shell, which could be associated with the negative spot in the  $Q$  maps (mainly in Q11, WK and P30 bands). For CTA 1, we do not apply any mask despite the fact that our polarization measurements could contain the information coming from the FS. The integrated flux densities in Table A4 could therefore be affected by these effects. In intensity, we obtained a flux density of  $9.0 \pm 1.4$  Jy at 11.1 GHz. For frequencies higher than 50 GHz, measurements are noise dominated and upper limits are computed. In the modelling of the intensity SED we consider only a synchrotron component. In polarization, we measure a polarized flux density of  $11.4 \pm 0.31$  Jy at 11.1 GHz, which is in agreement with the extrapolation of  $20.3 \pm 2.0$  Jy, assuming a spectral index  $\alpha_{\text{radio}} = -0.63$  (from  $\lambda 11$  cm, Sun et al. 2011a). As for intensity analysis, we take into account a single power-law function for the synchrotron component only. Figure 5 shows the

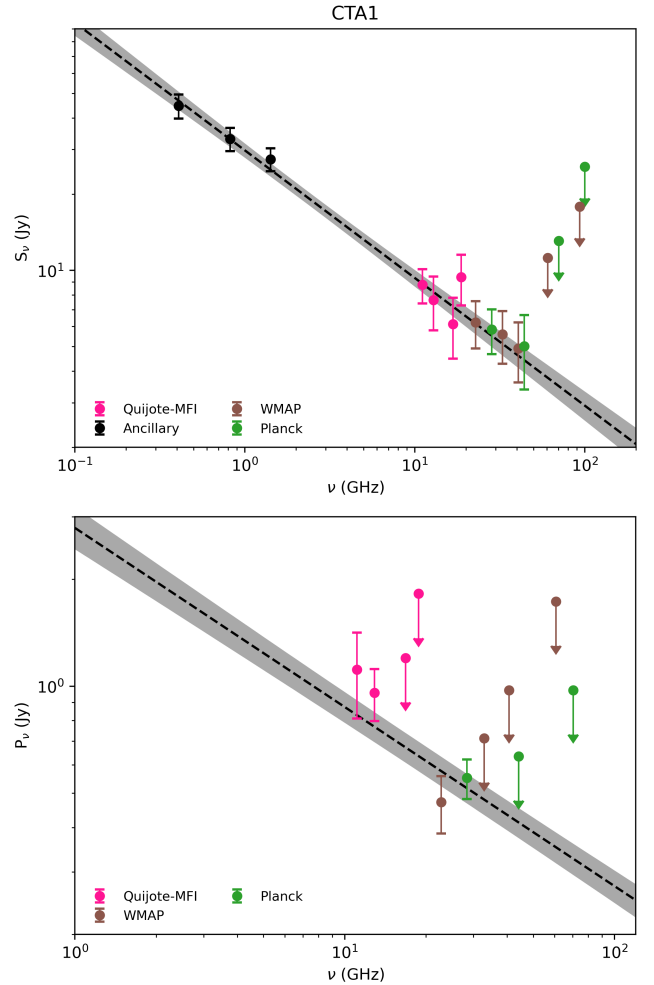


**Figure 5.** Spectral energy distribution of CTA 1 in intensity (top panel) and polarization (bottom panel). The integrated flux densities coming from different data sets are identified by colour. The dashed line corresponds to the SED model obtained and from INTPOL analysis (Table 6), grey shading represents its uncertainties.

intensity and polarization SEDs, including upper limits, of CTA 1 for the INTPOL analyses.

The intensity spectrum is described by a synchrotron component with amplitude of  $8.9 \pm 0.6$  Jy and spectral index of  $-0.50 \pm 0.03$ , as provided by both INT and INTPOL analyses. This result is expected because the polarized SED consists only of four measurements, thus the INTPOL fits is dominated by the intensity SED. This spectral index is  $\sim 2.2\sigma$  away from previous radio spectral index estimates, such as  $\alpha = -0.63 \pm 0.05$  computed at frequencies lower than 4.8 GHz (Sun et al. 2011a; Pineault et al. 1997). Sun et al. (2011a) also found consistency between the integrated flux density spectral index and the spectral index computed from the TT plot strategy. Therefore, the difference  $\Delta\alpha = 0.13$  between our results may be due to background contamination or to the worse beam resolution, which are not taken into account by our simple model. Also, the spatial distribution of the spectral index towards CTA 1 (at  $\sim 10$  arcmin, Sun et al. 2011a; Pineault et al. 1997; Sieber et al. 1981) shows a mean value of  $-0.5$  in the shell region, a value that is closer to our derived spectral index. In addition, this spectral index map shows

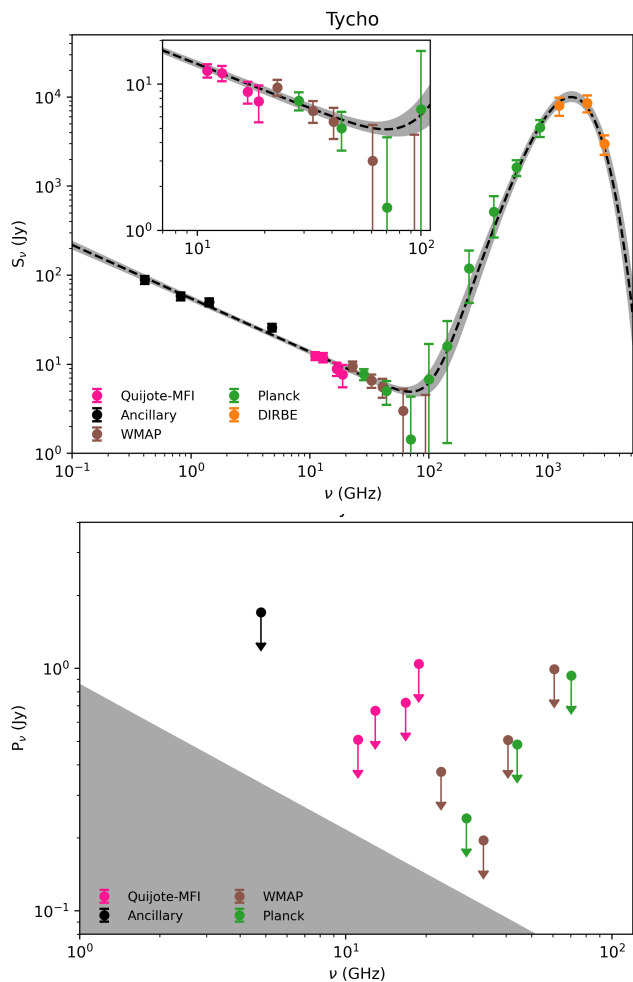


**Figure 6.** Spectral energy distribution of Tycho in intensity (top panel) and in polarization (bottom panel). The integrated flux densities coming from different data sets are identified by colour. The dashed line corresponds to the SED model obtained from INTPOL analysis (Table 6) and gray shading represents its uncertainties.

variations of up to 0.3, where the central branch has spectral indices of around  $-0.6$  and the breakout region shows steeper values.

In polarization the scarcity of high signal-to-noise measurements does not permit a reliable fit. Using four measurements and upper limits in the 10–90 GHz range, we obtained an amplitude of  $A_{\text{syn}}^{\text{pol}} = 1.0 \pm 0.2 \text{ Jy}$  and a spectral index of  $\alpha_{\text{pol}} = -0.8 \pm 0.3$  (POL analysis). Thanks to the high uncertainty of  $\alpha_{\text{pol}}$ , this value is in agreement with the INT and INTPOL analyses at just  $1.4\sigma$ . From the INTPOL analysis, the polarization fraction is  $\Pi_{\text{syn}} = 9.4 \pm 1.2\%$ , the highest  $\Pi_{\text{syn}}$  being computed for our SNR sample. We computed a polarization fraction  $\Pi_{\text{syn}}^{\text{pol,int}} = 11.1 \pm 2.4\%$  (from INT and POL amplitudes) in full agreement with the  $\Pi_{\text{syn}} = 9.4 \pm 1.2\%$  from the INTPOL case. From higher angular resolution maps, Sun et al. (2011a) found average polarization fractions of about 26%, 14% and 10% for the eastern shell, the central branch and the southern shell respectively.

## 5.5 SED of Tycho

In the QUIJOTE bands, the spatial structure of the total intensity emission of Tycho resembles that of a compact source, with low background contamination (see Figure A5). This is due to its small angular size ( $\sim 8$  arcmin, Loru et al. 2019) compared to our beam size. In contrast, the polarization maps reveal negligible  $Q$  and  $U$  emission, which are dominated by noise fluctuations. The raw integrated flux densities are presented in Table A5. In Q19 and WK bands, we measure flux densities in total intensity of  $7.6 \pm 2.1$  and  $9.9 \pm 1.2 \text{ Jy}$  (not colour-corrected), which agree with the value of  $8.8 \pm 0.9 \text{ Jy}$  measured with the Sardinia Radio Telescope at 21.4 GHz (Loru et al. 2019). In contrast, our measurement of  $25.9 \pm 2.6 \text{ Jy}$  at 4.8 GHz departs from the value of  $20 \pm 2 \text{ Jy}$  reported by Sun et al. (2011b). In polarization, we quote upper limits on integrated polarized intensity for all frequencies.

At 4.8 GHz our measured flux density in total polarization,  $1.4 \pm 0.2 \text{ Jy}$ , is significantly higher than the value of  $0.28 \pm 0.03 \text{ Jy}$  obtained by Sun et al. (2011b). This difference could be due to spurious emission coming from the Faraday rotation of a source to the south-east inside the annulus (see map P in Figure A5). The source is only visible in the original Urumqi maps at 9.5 arcmin and our angular resolution extends its contribution inside our aperture. Therefore we only estimate an upper limit on the polarized flux density at 4.8 GHz. The intensity and polarized SEDs are drawn in Figure 6 using as a reference the INTPOL analysis.

The intensity spectrum of the remnant below 100 GHz is well characterized by a spectral index of  $-0.60 \pm 0.02$  and an amplitude of  $12.9 \text{ Jy}$  at 11.1 GHz (see Table 6). The thermal dust emission is coming from extended diffuse emission not associated with the SNR. Our synchrotron component agrees with previous spectral indices of  $\alpha = -0.624 \pm 0.004$  (at 0.015–70 GHz Castelletti et al. 2021) and  $\alpha = -0.58 \pm 0.02$  (Sun et al. 2011b; Loru et al. 2019). Our data lack sufficient sensitivity and frequency coverage to be able to trace the weak concave-up change in the spectral index,  $\Delta\alpha \approx 0.04$ , at around 1 GHz reported by previous studies (Reynolds & Ellison 1992; Castelletti et al. 2021). Around 100 GHz, the steepening of the spectrum could be understood in terms of a small negative residual CMB contribution. We rule out a spectral break of the synchrotron component because it is not expected in this frequency coverage. In fact, the gamma-ray analysis suggests a spectral break at higher energies at around 100 eV (Acciari et al. 2011).

As polarization measurements yield only upper limits for all frequency bands; the analyses taking into consideration the polarized SED just provides constraints on the polarized properties. From the INTPOL, we find an upper limit of  $\Pi_{\text{syn}} < 3.2\%$  (at 95% of C.L.). This is a conservative constraint with respect to the average percentage polarization of 1% (at 4.8 GHz, Sun et al. 2011b) and 2.5% (at 1.42 GHz, Kothés et al. 2006) reported previously. At 4.8 GHz, we obtain a constraint on the integrated polarization fraction of 7.4% (at 95% C.L.), and our most restrictive polarization levels are of the order of 4% for the Q11 and WK bands. In this context, we do not have the sensitivity to reach such low polarization level observed at lower frequencies.

## 5.6 SED of HB 9

On scales of 1 deg, the shell structure of HB 9 dominates the total-intensity emission, where the peak emission is off-centre to the south-west (see Figure A6). Synchrotron emission from HB 9 is visible up to 70 GHz, while a thermal dust component is captured inside the aperture although there is a weak spatial correlation be-

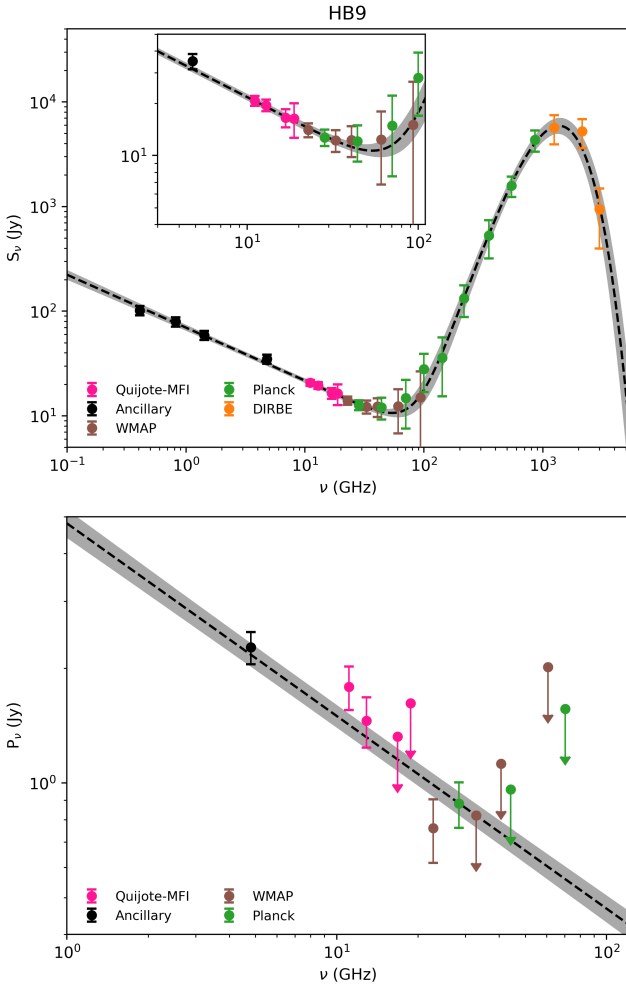


**Figure 7.** Spectral energy distribution of HB 9 in intensity (top panel) and in polarization (bottom panel). The integrated flux densities coming from different data sets are identified by colour. The dashed line corresponds to the SED model obtained from INTPOL analysis (Table 6) and grey shading represents its uncertainties.

tween them. In polarization, the smoothed  $U$  maps, mainly in the Urumqi band, reveal two spots with positive (north-west) and negative (south-east) emission, and this pattern seems to prevail up to 40 GHz. At higher frequencies, the polarized emission of HB 9 becomes very weak (see  $P$  map in Figure A6). For HB 9, the raw flux densities are presented in Table A6. In intensity, we measure a flux density of  $35.0 \pm 3.5$  at 4.8 GHz that is consistent with the value of  $33.9 \pm 3.4$  Jy reported by Gao et al. (2011). At 11.1 GHz, the QUIJOTE measurement is  $21.2 \pm 1.4$  Jy. In polarization, upper limits are provided for frequencies higher than 30 GHz. Therefore, we assumed that synchrotron emission drives the polarization spectrum of HB 9. The intensity and polarized SEDs are presented in Figure 7 for the INTPOL analysis.

For the intensity signal, the INTPOL and INT fits provide similar amplitudes of about  $21 \pm 1$  Jy (at 11.1 GHz) and spectral index of  $-0.51 \pm 0.02$ . Our fitted spectral index is flatter than that of  $-0.59 \pm 0.02$  computed in the range 0.1–5 GHz by Gao et al. (2011), while it is steeper than the value of  $-0.44 \pm 0.04$  obtained at frequencies below 1 GHz by Willis (1973). As pointed out by Reich et al. (2003),

the differences in spectral index could be caused by the contribution from the HB 9 plateau, which can be diluted on our maps due to our large beam. These values are consistent with the spatial variation of the spectral index,  $-0.4$  to  $-0.9$ , obtained with a TT-plot approach over fifty two regions across HB 9 (408–1420 MHz, Leahy & Tian 2007). However, our spectral analysis shows no evidences for the spectral change at around 1 GHz proposed by Willis (1973). This result is consistent with the simple power law behaviour observed by previous authors (see Reich et al. 2003; Gao et al. 2011).

We obtained a polarization fraction  $\Pi_{\text{syn}} = 6.9 \pm 0.5\%$  and a spectral index  $\alpha = -0.51 \pm 0.02$  for the INTPOL analysis. For the POL case, the polarized spectrum is described by a single power law with spectral index  $\alpha^{\text{pol}} = -0.60 \pm 0.08$  and amplitude  $A_{11.1}^{\text{pol}} = 3.2 \pm 0.2$  Jy. This spectral index of polarization is steeper than that obtained with intensity data ( $\alpha$  from INT and INTPOL fits), although they are consistent when the uncertainties are taken into consideration. Furthermore,  $\alpha^{\text{pol}} = -0.60 \pm 0.08$  is in agreement with the value of  $\alpha = -0.59 \pm 0.02$  obtained with only intensity flux densities between 0.1 and 5 GHz (Gao et al. 2011). Moreover, we computed a polarization fraction of  $\Pi_{\text{syn}}^{\text{pol,int}} = 6.8 \pm 0.7\%$  (from INT and POL amplitudes) in full agreement with the previous  $\Pi_{\text{syn}} = 6.9 \pm 0.5\%$  value from the INTPOL case, which shows the stability of the estimation of the polarization fraction. This value is only half the average polarization degree of  $9.1 \pm 0.1\%$  and  $15.6 \pm 1.6\%$  obtained with better angular resolutions at 1.42 GHz by Gao et al. (2011) and at 4.8 GHz by Kothes et al. (2006) respectively.

## 5.7 Overall description of the QUIJOTE SNR sample

This section is devoted to exploring the properties of SNRs from a statistical point of view. To this end, the observational properties obtained in this study are complemented with previous QUIJOTE-MFI studies of SNRs. A joint study of these sources is possible because the SED analyses and methodologies used in those previous studies are fully consistent with those used in this article (described in Section 4).

### 5.7.1 SNR spectral indices and ages

We explore the evolution of the polarized spectral index of SNRs studied with QUIJOTE-MFI on scales of 1 deg. This sample consists of our six SNRs and other sources such as W44 (Génova-Santos et al. 2017), IC443, W49 and W51 (Tramonte et al. 2023). For our six SNRs, we select  $\alpha^{\text{intpol}}$  which contains information from the intensity and polarized SEDs. For W44, IC443, W49 and W51, we use the polarized spectral index  $\alpha^{\text{pol}}$  derived in those references, since these did not simultaneously fit intensity and polarization signals.

On angular scales of 1 deg, we obtain an average spectral index of  $-0.48 \pm 0.16$  for the whole sample, where the term 0.16 represents the scatter of the measurements. For evolved SNRs, i.e. older than 20 kyr, we find flatter spectral indices covering from  $-0.54$  to  $-0.24$  (CTB 80, HB 21, W51, W44 and IC443, see Figure 8), with an average spectral index of  $-0.37 \pm 0.18$ . In contrast, we recover a mean spectral index of  $-0.55 \pm 0.08$  for younger remnants ( $< 20$  kyr). The spectral indices are significantly flatter for the older CTB 80 ( $\sim 65$  kyrs) and HB 21 ( $\sim 30$  kyrs), reaching indices of  $-0.24$  and  $-0.36$  respectively. In fact, CTB 80 and HB 21 exhibit a curved spectrum; however, here we use the radio spectral indices  $\alpha_{\text{bb}}^{\text{intpol}}$  (purple points in Figure 8). Therefore, we obtain flatter spectral indices for the older SNRs, which agrees with other Galactic studies,

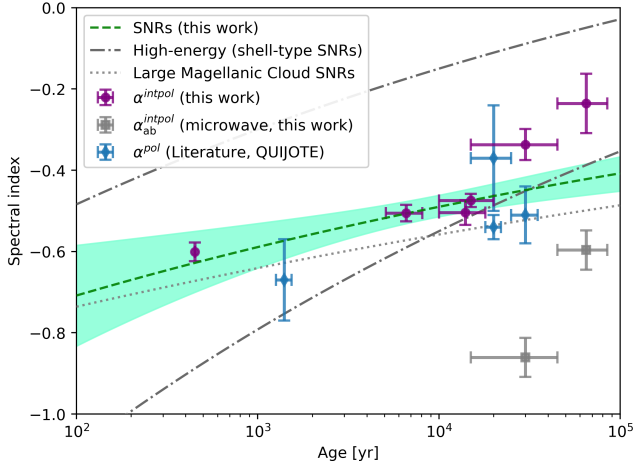


**Figure 8.** The spectral index evolution for SNRs observed with QUIJOTE-MFI data. The spectral indices are obtained from SEDs built at 1 deg resolution (FWHM), which also span information from the intensity and polarization SED. The blue points correspond to W44, IC443, W49 and W51 from other QUIJOTE-MFI studies. The ages of SNRs are taken from Table 1. The purple points identify the SNRs studied in this paper. For remnants with curved spectra (HB 21 and CTB 80), we display the spectral indices below (purple circles) and above (grey squares) the break frequency. The evolution of the spectral index is modelled with a power-law function fitting the purple and blue points, which provides  $a = -0.49 \pm 0.02$  and  $b = -0.07 \pm 0.03$  (the green dashed line). In addition, we also drawn the relation between the spectral index and age for the Milky Way (the dashed and dotted lines, see text for details) and for the Large Magellanic Cloud (the dotted line, [Bozzetto et al. 2017](#)).

although the scatter of the spectral index distribution is still large ([Clark & Caswell 1976](#); [Harris 1962](#); [Zeng et al. 2019](#); [Ranasinghe & Leahy 2023](#)).

To find a relation between spectral index and age, we consider a power-law function following the same procedure implemented for the Large Magellanic Cloud SNRs (LMC, [Bozzetto et al. 2017](#)):

$$\alpha(t; a, b) = a(t/t_{\text{ref}})^b, \quad (16)$$

where  $a$  is the amplitude,  $t$  is the age normalised to  $t_{\text{ref}} = 10^4$  yr and  $b$  is the slope. The fit provides  $a = -0.49 \pm 0.02$  and  $b = -0.07 \pm 0.03$ . This evolution of the spectral index is drawn by dashed green line in Figure 8. This fit underestimates the spectral indices of HB 21 and CTB 80, with a significance of  $2.0\sigma$  and  $4.6\sigma$  respectively. This could suggest a different trend for these older SNRs ( $\geq 30$  kyr) with curved spectra. Note that the W51 ( $\sim 30$  kyr), W44 and IC443 ( $\sim 20$  kyr) remnants are inside the modelled tendency although the dispersion is higher than in younger SNRs ( $< 20$  kyr).

Although our modelling is conservative and limited by our number of SNRs, it is in agreement with other Galactic constraints. The dash-dotted lines of Figure 8 show that our spectral index tendency is contained within the evolutionary trend extrapolated from [Zeng et al. \(2019\)](#). Actually, they obtained the correlation of the particle spectral index and the age of Galactic SNRs (Figure 3b of [Zeng et al. 2019](#)), from which we put upper and lower edges by power laws with slope  $-0.09$  and amplitudes of 2.1 and 1.3 (at  $t_{\text{ref}} = 10^4$  yr) respectively. Then these ages are translated to the  $\alpha_{\text{radio}}(t)$  using the established relationship  $\alpha_{\text{radio}} = (1 - \Gamma_p)/2$  to yield the previously mentioned dash-dotted lines of Figure 8. The

**Table 7.** Summary of the polarization properties considered for statistical analysis.

SNR	$d$ [kpc]	age [yrs]	$\Pi$ [%]	$\delta_\pi$ [%]
Tycho	2.50	450	$\leq 3.2$	$0.0 \pm 2.2$
W49	11.00	1400	$11.0 \pm 6.3$	$15.4 \pm 8.8$
HB 9	0.60	6600	$6.9 \pm 0.5$	$10.0 \pm 0.7$
CTA 1	1.40	14000	$9.4 \pm 1.2$	$13.5 \pm 1.8$
Cygnus Loop	0.74	15000	$6.0 \pm 0.4$	$8.7 \pm 0.6$
IC443	1.90	20000	$2.7 \pm 1.1$	$4.0 \pm 1.6$
W44	3.10	20000	$15.2 \pm 1.8$	$21.8 \pm 2.5$
W51	5.40	30000	$5.5 \pm 2.5$	$8.0 \pm 3.6$
HB 21	1.74	30000	$5.0 \pm 0.2$	$7.5 \pm 0.3$
CTB 80	2.00	65000	$3.7 \pm 0.3$	$5.7 \pm 0.5$

region bounded by these curves is wide and spans the flatter spectra of CTB 80 and HB 21 (for the radio spectral indices); although their microwave spectral indices fall outside this trend (grey squares in Figure 8).

Regarding comparisons with extragalactic studies, [Bozzetto et al. \(2017\)](#) obtained a slope  $b_{\text{LMC}} = -0.06 \pm 0.02$  and amplitude  $a_{\text{LMC}} = -0.97 \pm 0.09$  at 1 yr for the LMC (see dotted line in Figure 8). They established the correlation of the radio spectral index and age using 29 LMC SNRs, which includes multi-epoch observations of the younger remnant SN1987A. The latter was crucial to confirm that evolved remnants have flatter spectral indices than the younger ones. The model evolution of spectral indices for the LMC exhibits steeper spectral indices than our predictions from the Galaxy model ( $b = -0.07 \pm 0.04$ ). Although the differences fall in the range 0.07 to 0.08 for ages  $\geq 15$  kyr, we found a consistency when uncertainties are considered. As final remark, we emphasise that results for our Galaxy (e.g. [Green 2019](#); [Zeng et al. 2019](#)) and the LMC ([Bozzetto et al. 2017](#)) arise from the characterization of the intensity SED, while our results also span the polarization properties.

### 5.7.2 Observed polarization fraction

We investigate the observed polarized fraction of SNRs studied with QUIJOTE-MFI on a scale of 1 deg. We consider the same sample as in the previous section: our six remnants and sources W44 ([Génova-Santos et al. 2017](#)), IC443, W49 and W51 ([Tramonte et al. 2023](#)). For our six SNRs, we select the  $\Pi_{\text{syn}}$  values yielded by the joint fit of the intensity and polarized SEDs (INTPOL case). For W44, IC443, W49 and W51, we use the polarized fractions computed from the intensity and polarized amplitudes fitted respectively to the intensity and polarized SEDs. In addition, as the observational polarization degree is equivalent to a decreasing factor of the intrinsic polarization, i.e.  $\Pi_o(\alpha_{\text{radio}}) \cdot \delta_\pi$  ([Burn 1966](#); [Sieber et al. 1979](#)), we also compute this  $\delta_\pi$  as follows:

$$\delta_\pi = \frac{\Pi_{\text{obs}}}{\Pi_o(\alpha_{\text{radio}})}, \quad (17)$$

$\alpha_{\text{radio}}$  being the spectral indices considered in the previous section ( $\alpha$  or  $\alpha_{\text{bb}}$ ). Table 7 presents the  $\Pi_{\text{obs}}$  and  $\delta_\pi$  values for each SNR.

On an angular scale of 1 deg, we found a mean and standard deviation of  $7.2 \pm 4.9\%$ , which agrees with previous studies that obtain polarization fractions lower than 20% (e.g. see, [Kothes et al. 2006](#); [Gao et al. 2011](#)). We also found lower polarization fraction levels ( $5.5 \pm 2.5$ ,  $5.0 \pm 0.2$ ,  $3.7 \pm 0.3\%$ ) for the older SNRs (W51, HB 21 and CTB 80), although some younger remnants also have weak polarization; for example, we compute an upper limit of

3.2% at 95% C.L. for Tycho. Nevertheless, the depolarization effects change towards each region (Gardner & Whiteoak 1966; Burn 1966; Sazonov 1973), resulting in unclear correlations between the different parameters obtained from the SED; for instance, the expected evolution of the intrinsic polarization fraction (equations 1 and 16). Thus the observed low polarization fractions for our older SNRs does not constitute robust evidence of a correlation between the  $\Pi_{\text{obs}}$  and the age of SNRs. Even so, this tendency could be explored in future studies, which would require observations with better resolution to avoid the effects of our large beam.

In the ideal case that  $\delta_\pi$  is not dominated by the dilution due to our large beam, the observed low polarization levels trace the importance of a disordered and/or turbulent magnetic field component (Burn 1966; Sazonov 1973) as  $\delta_\pi = H_0^2 / (H_0^2 + H_r^2)$ .<sup>16</sup> In our Galaxy, the average of  $\langle H_r \rangle / \langle H_0 \rangle$  falls in the range 3 to 5 (Beck 2001, and references therein), yielding a  $\delta_\pi$  between 10% and 4%. For our SNR sample, we found a mean and standard deviation of  $10.5 \pm 5.2\%$  for  $\delta_\pi$  (see Table 7), which agrees with the expected 10–4% observed in our Galaxy. In addition, the  $\delta_\pi$  does not seem to depend on distance or position.

### 5.7.3 The AME in SNRs

As was pointed in previous sections, the presence of AME towards our SNRs is not favoured by the SED analysis. In fact, the spectra are dominated by the synchrotron radiation in the 10–40 GHz range. Moreover, the thermal dust contribution is low, so the AME contribution is also expected to be low, reaching values of the order of, or smaller than, our flux density uncertainties. We can estimate the expected AME contribution at 22.8 GHz considering the AME emissivity,  $\epsilon_{\text{AME}, \tau_{353}}^{22.8\text{GHz}}$ , based on the ratio between the AME amplitude at 22.8 GHz and the dust emissivity at 353 GHz. We use the value 9 K as reference for our Galaxy (Planck Collaboration et al. 2016b; Harper et al. 2022; Fernández-Torreiro et al. 2023, and references therein). For instance, the study of AME in the Galactic plane provided  $9.84 \pm 3.57$  K (using QUIJOTE-MFI, Fernández-Torreiro et al. 2023), which is consistent with a full-sky analysis ( $8.3 \pm 0.8$  K, Planck Collaboration et al. 2016b). Table 8 presents the predicted AME amplitudes at 22.8 GHz,  $A_{\text{AME, pred}}^{22.8\text{GHz}}$ , considering the  $\tau_{353}$  values from the INTPOL case. These are unavailable for CTB 80 and CTA 1 since the thermal dust component was not considered in the SEDs fit.

We also study the presence of AME following the methodology proposed in Section 4.4, where an AME component is considered in the SED fit. Overall, we obtain AME amplitudes compatible with zero, thus we provide only upper limits on the AME amplitude (at 95% C.L) for our six SNRs (see Table 8). These limits are dominated by the high uncertainties behind  $A_{\text{AME}}$  and are driven mainly by the uncertainties of the low-frequency (microwave) part of the spectrum. Although these upper limits are not a strong constraint on AME amplitudes, they suggest that the AME contribution is negligible in the range 10–40 GHz for our six remnants. Moreover, this is also supported by the AME emissivity,  $\epsilon_{\text{AME}, \tau_{353}}^{22.8\text{GHz}}$ , obtained from  $A_{\text{AME}}$  and  $\tau_{353}$  provided by the SED fit. We compute upper limits on  $\epsilon_{\text{AME}, \tau_{353}}^{22.8\text{GHz}}$  (at 95 C.L.) of between 5 and 13 K. Tycho and HB 9 show, respectively, the stronger constraints of 6.8 and 4.9 K (at  $2\sigma$ ), which are lower than the observed values in our Galaxy

**Table 8.** Upper limits on the presence of AME towards our SNRs. The second and third rows show respectively the constraints on the amplitude of AME ( $A_{\text{AME}}$  in units of Jy) and on the AME emissivity ( $\epsilon_{\text{AME}, \tau_{353}}^{22.8\text{GHz}}$  in units of K) when an AME component is considered in the SED fit (see section 4.4). These upper limits are computed at 95% of confidence level (95% C.L.). The last row shows the AME amplitude at 22.8 GHz,  $A_{\text{AME, pred}}^{22.8\text{GHz}}$ , obtained from the AME emissivity  $\epsilon_{\text{AME}, \tau_{353}}^{22.8\text{GHz}} = 9$  K.

	CTB 80	Cyg. L.	HB 21	CTA 1	Tycho	HB 9
	Upper limits at 95% C.L.					
$A_{\text{AME}}$	2.8	2.4	3.9	1.4	1.3	1.5
$\epsilon_{\text{AME}, \tau_{353}}^{22.8\text{GHz}}$	–	11.0	12.3	–	6.8	4.9
	Predictions from the AME emissivity					
$A_{\text{AME, pred}}^{22.8\text{GHz}}$	–	1.8	2.9	–	1.6	2.5

(8 – 11 K, Planck Collaboration et al. 2016b; Harper et al. 2022; Fernández-Torreiro et al. 2023).

Other QUIJOTE studies also favour the non-detection of AME towards SNRs on a scale of 1 deg: *i*) the main QUIJOTE-MFI calibrators, the Crab Nebulae and CasA (Rubiño-Martín et al. 2023; Genova-Santos et al. 2023b, in prep.), *ii*) 3C 58 (the Fan region analysis, Ruiz-Granados et al. 2023, in prep.), and *iii*) the G010.19-00.32, G037.79-00.11 and G045.47+00.06 catalogued as semi-significant AME sources (Poidevin et al. 2023). Therefore, sources W44 (Genova-Santos et al. 2017), W49 and W51 (Tramonte et al. 2023) appear to be the only SNRs with an AME contribution on a scale of 1 deg. These three SNRs share two features: first, they interact with HII or molecular clouds; and second, they are all located within the first quadrant of the Galactic plane. However, these two characteristics cannot be assumed as drivers of AME emission in SNRs. Regarding morphology, CTA 1 and HB 21 are considered as remnants that interact with their surroundings, and both lack an AME component in their spectra. In addition, we do not measure AME in SNRs catalogued as plerion types, e.g. compact source remnants w.r.t. our beam size, such as TauA, CasA and 3C58 (Rubiño-Martín et al. 2023; Ruiz-Granados et al. 2023), mainly owing to the lack of a thermal dust component in their spectra. Concerning location, CTB 80, the Cygnus Loop and HB 21 are also in the first quadrant. In addition, SNRs located far from Galactic plane (the Cygnus Loop, CTA 1 and HB 21) also show no evidence of an AME spectrum, or in cases that are relatively close to the Galactic plane in the second and third quadrants (such as Cas A, 3C58 and HB 9).

Therefore, we point to an overlap of different mechanisms along the line of sight rather than to a strong relationship between the AME and SNR scenarios. For instance, on arcminute scales, Loru et al. (2019) used the Sardinia Radio Telescope (SRT, 1.55, 7.0 and 21.4 GHz) to discount an AME spectrum for W44 that had previously been reported by Genova-Santos et al. (2017) at 1 deg scale. Recently, the COMAP maps of Galactic plane (Rennie et al. 2022), covering the 26–31 GHz range at 4.5 arcmin, helped to confirm the SRT results, for which the spectrum is well modelled by a simple synchrotron mechanism with a spectral index of  $-0.54 \pm 0.06$ . In this context, this observational panorama stresses the need for surveys with better angular resolutions in order to access the structure of W44, W49 and W51 in the range 10–40 GHz.

<sup>16</sup> In this equation,  $H_0$  is the regular magnetic field component and  $H_r$  is a random isotropic magnetic field component (with Gaussian variance  $2/3H_0^2$ ).

## 6 CONCLUSIONS

We exploit the new QUIJOTE-MFI wide survey, at 10–20 GHz, to study the intensity and polarization properties of radio–microwave emission towards the SNRs CTB 80, the Cygnus Loop, HB 21, CTA 1, Tycho and HB 9. For each SNR we present updated modelling of the intensity and polarization SEDs, which also takes into account a simultaneous fit of intensity and polarization spectra, taking advantage of the low depolarization level expected in the frequency range of QUIJOTE-MFI (and at higher frequencies). For all six sources, we obtain the properties of the synchrotron radiation on angular scales of 1 deg, mainly associated with the remnant emission of each region (Table 6), and these properties are consistent with previous studies. However, the weak intensity signal of the thermal dust emission captured inside the apertures in some of them is considered as background coming from the Galaxy.

In intensity, we confirm the curved spectra of CTB 80 and HB 21, where a power law with an abrupt break is preferred over other models, such as a power law with an exponential cut-off. In addition, we compute constraints on the intensity amplitude of the Anomalous Microwave Emission that suggest a negligible AME contribution towards all six remnants. From the simultaneous intensity and polarization fit, we recover radio spectral indices as flat as  $-0.24$ , with a mean and scatter values of  $-0.44 \pm 0.12$ . In addition, the polarization degree levels are lower than 10% with a mean and scatter values of  $6.1 \pm 1.9\%$ , while we set the upper limit of  $\Pi_{\text{syn}} \lesssim 3.2\%$  (at 95% of confidential level) only for Tycho.

When combining our results with the measurements from other QUIJOTE-MFI studies of SNRs, we find that radio spectral indices are flatter for mature SNRs and are significantly flat for CTB 80 ( $-0.24^{+0.07}_{-0.06}$ ) and HB 21 ( $-0.34^{+0.04}_{-0.03}$ ). We found the evolution of the spectral indices to be adequately described by a power-law function with an exponent  $-0.07 \pm 0.03$  and amplitude  $-0.49 \pm 0.02$ , which is conservative and agrees with previous studies of our Galaxy and the Large Magellanic Cloud. Further observations at higher sensitivities and beam resolutions at lower frequencies in these and other remnants, will help to complete this study by increasing the number of SNRs and improving the SED modelling. Therefore, data product from CBASS at 5 GHz (Jones et al. 2018) and the upcoming updated version of the MFI instrument of QUIJOTE (MFI2, Hoyland et al. 2022) will be valuable.

Regarding the AME component towards SNRs on angular scales of 1 deg, the data indicate the overlapping of components along the line of sight rather than a strong relationship between the AME and synchrotron radiation from the SNRs as the reason why only certain SNRs (W44, W49 and W51) show an AME contribution in their spectra. Since they interact with HII or molecular clouds and are embedded inside the Galactic plane in the first quadrant, further observations at higher angular resolution of W44, W49 and W51 will be useful to understanding the nature of the anomalous emission observed on angular scale of 1 deg. This is one of the goals of the TFGI instrument of QUIJOTE (30 and 41 GHz, Pérez-de-Taoro et al. 2016), which is currently operating at Teide Observatory.

## ACKNOWLEDGEMENTS

CHLC appreciates the knowledge, professional training and affection received from Rodolfo Barbá, who has become the most important Supernova of my life. Now I can find you among the stars (RIP, 2021-12-07). We thank Terry Mahoney (Scientific Editorial

Service of the IAC) for proofreading this manuscript. We thank the staff of the Teide Observatory for invaluable assistance in the commissioning and operation of QUIJOTE. The QUIJOTE experiment is being developed by the Instituto de Astrofísica de Canarias (IAC), the Instituto de Física de Cantabria (IFCA), and the Universities of Cantabria, Manchester and Cambridge. Partial financial support was provided by the Spanish Ministry of Science and Innovation under the projects AYA2007-68058-C03-01, AYA2007-68058-C03-02, AYA2010-21766-C03-01, AYA2010-21766-C03-02, AYA2014-60438-P, ESP2015-70646-C2-1-R, AYA2017-84185-P, ESP2017-83921-C2-1-R, PID2019-110610RB-C21, PID2020-120514GB-I00, PID2019-110614GB-C21, IACA13-3E-2336, IACA15-BE-3707, EQC2018-004918-P, the Severo Ochoa Programs SEV-2015-0548 and CEX2019-000920-S, the Maria de Maeztu Program MDM-2017-0765 and by the Consolider-Ingenio project CSD2010-00064 (EPI: Exploring the Physics of Inflation). We acknowledge support from the ACIISI, Consejería de Economía, Conocimiento y Empleo del Gobierno de Canarias and the European Regional Development Fund (ERDF) under grant with reference ProID2020010108. This project has received funding from the European Union’s Horizon 2020 research and innovation program under grant agreement number 687312 (RADIOFOREGROUNDS). We acknowledge the use of data provided by the Centre d’Analyse de Données Etendues (CADE), a service of IRAP-UPS/CNRS (<http://cade.irap.omp.eu>, Paradis et al. 2012). This research has made use of the SIMBAD database, operated at CDS, Strasbourg, France (Wenger et al. 2000). Some of the results in this paper have been derived using the healpy and HEALPIX package (Górski et al. 2005; Zonca et al. 2019). We have also used scipy (Virtanen et al. 2020), emcee (Foreman-Mackey et al. 2013), numpy (Harris et al. 2020), matplotlib (Hunter 2007), corner (Foreman-Mackey 2016) and astropy (Astropy Collaboration et al. 2013, 2018) python packages.

## DATA AVAILABILITY

The QUIJOTE-MFI wide survey maps are available in the QUIJOTE collaboration webpage<sup>4</sup> (<https://research.iac.es/proyecto/quijote>). The ancillary maps used in this work are publicly available in databases such as LAMBDA<sup>8</sup>, PLA<sup>9</sup> and CADE<sup>6</sup>, as explained in Sect. 3.

## REFERENCES

- Abdo A. A., et al., 2008, *Science*, **322**, 1218
- Abdo A. A., et al., 2010, *ApJ*, **720**, 26
- Abdo A. A., et al., 2012, *ApJ*, **744**, 146
- Abdollahi S., et al., 2020, *ApJS*, **247**, 33
- Acciari V. A., et al., 2011, *ApJ*, **730**, L20
- Aliu E., et al., 2013, *ApJ*, **764**, 38
- Angerhofer P. E., Strom R. G., Velusamy T., Kundu M. R., 1981, *A&A*, **94**, 313
- Araya M., 2014, *MNRAS*, **444**, 860
- Araya M., Herrera C., 2021, *MNRAS*, **502**, 472
- Arias M., Vink J., Zhou P., de Gasperin F., Hardcastle M. J., Shimwell T. W., 2019, *AJ*, **158**, 253
- Astropy Collaboration et al., 2013, *A&A*, **558**, A33
- Astropy Collaboration et al., 2018, *AJ*, **156**, 123
- Baade W., 1943, *ApJ*, **97**, 119
- Beck R., 2001, *Space Sci. Rev.*, **99**, 243
- Bell A. R., 1978, *MNRAS*, **182**, 147
- Bennett C. L., et al., 2013, *ApJS*, **208**, 20

- Berkhuijsen E. M., 1971, *A&A*, **14**, 359
- Blair W. P., Fesen R. A., Rull T. R., Kirshner R. P., 1984, *ApJ*, **282**, 161
- Blair W. P., Sankrit R., Raymond J. C., 2005, *AJ*, **129**, 2268
- Blandford R. D., Ostriker J. P., 1978, *ApJ*, **221**, L29
- Bozzetto L. M., et al., 2017, *ApJS*, **230**, 2
- Burn B. J., 1966, *MNRAS*, **133**, 67
- Byun D.-Y., Koo B.-C., Tatematsu K., Sunada K., 2006, *ApJ*, **637**, 283
- Carmona E., Costado M. T., Font L., Zapatero J., 2009, arXiv e-prints, p. arXiv:0907.1009
- Castelletti G., Dubner G., 2005, *A&A*, **440**, 171
- Castelletti G., Dubner G., Golap K., Goss W. M., Velázquez P. F., Holdaway M., Rao A. P., 2003, *AJ*, **126**, 2114
- Castelletti G., Supan L., Peters W. M., Kassim N. E., 2021, *A&A*, **653**, A62
- Caswell J. L., 1976, *MNRAS*, **177**, 601
- Caswell J. L., Murray J. D., Roger R. S., Cole D. J., Cooke D. J., 1975, *A&A*, **45**, 239
- Clark D. H., Caswell J. L., 1976, *MNRAS*, **174**, 267
- Corey B. E., Wilkinson D. T., 1976, in *Bulletin of the American Astronomical Society*. p. 351
- Cruciani A., et al., 2016, *MNRAS*, **459**, 4224
- D'Odorico S., Sabbadin F., 1977, *A&AS*, **28**, 439
- Decourchelle A., 2017, in Alsabti A. W., Murdin P., eds., *Handbook of Supernovae*. p. 117, doi:10.1007/978-3-319-21846-5\_48
- Denoyer L. K., 1974, *AJ*, **79**, 1253
- Desert F.-X., Boulanger F., Puget J. L., 1990, *A&A*, **237**, 215
- Dickinson C., Peel M., Vidal M., 2011, *MNRAS*, **418**, L35
- Dickinson C., et al., 2018, *New Astron. Rev.*, **80**, 1
- Draine B. T., Hensley B., 2013, *ApJ*, **765**, 159
- Draine B. T., Hensley B. S., 2016, *ApJ*, **831**, 59
- Draine B. T., Lazarian A., 1998, *ApJ*, **508**, 157
- Draine B. T., Lazarian A., 1999, *ApJ*, **512**, 740
- Dubner G., Giacani E., 2015, *A&ARv*, **23**, 3
- Dwarakanath K. S., Shevgaonkar R. K., Sastry C. V., 1982, *Journal of Astrophysics and Astronomy*, **3**, 207
- Fernández-Torreiro M., et al., 2023, *MNRAS*, in prep.
- Fesen R. A., Blair W. P., Kirshner R. P., Gull T. R., Parker R. A. R., 1981, *ApJ*, **247**, 148
- Fesen R. A., Gull T. R., Ketelsen D. A., 1983, *ApJS*, **51**, 337
- Fesen R. A., Neustadt J. M. M., Black C. S., Milisavljevic D., 2018a, *MNRAS*, **475**, 3996
- Fesen R. A., Weil K. E., Cisneros I. A., Blair W. P., Raymond J. C., 2018b, *MNRAS*, **481**, 1786
- Fixsen D. J., Cheng E. S., Gales J. M., Mather J. C., Shafer R. A., Wright E. L., 1996, *ApJ*, **473**, 576
- Flower D. R., Pineau des Forêts G., 1999, *MNRAS*, **308**, 271
- Foreman-Mackey D., 2016, *Journal of Open Source Software*, **1**, 24
- Foreman-Mackey D., Hogg D. W., Lang D., Goodman J., 2013, *PASP*, **125**, 306
- Fürst E., Reich W., 2004, in Uyaniker B., Reich W., Wielebinski R., eds., *The Magnetized Interstellar Medium*. pp 141–146
- Gamow G., 1946, *Physical Review*, **70**, 572
- Gao X. Y., et al., 2010, *A&A*, **515**, A64
- Gao X. Y., Han J. L., Reich W., Reich P., Sun X. H., Xiao L., 2011, *A&A*, **529**, A159
- Gardner F. F., Whiteoak J. B., 1966, *ARA&A*, **4**, 245
- Génova-Santos R., et al., 2015a, in Cenarro A. J., Figueras F., Hernández-Monteagudo C., Trujillo Bueno J., Valdivielso L., eds., *Highlights of Spanish Astrophysics VIII*. pp 207–212 (arXiv:1504.03514)
- Génova-Santos R., et al., 2015b, *MNRAS*, **452**, 4169
- Génova-Santos R., et al., 2017, *MNRAS*, **464**, 4107
- Génova-Santos R., et al., 2023a, *MNRAS*, in prep.
- Génova-Santos R., et al., 2023b, *MNRAS*, in prep.
- Ginzburg V. L., Syrovatskii S. I., 1965, *ARA&A*, **3**, 297
- Gomez A., et al., 2010, in *Ground-based and Airborne Telescopes III*. p. 77330Z, doi:10.1117/12.857286
- Gorenstein P., Kellogg E. M., Gursky H., 1970, *ApJ*, **160**, 199
- Górski K. M., Hivon E., Banday A. J., Wandelt B. D., Hansen F. K., Reinecke M., Bartelmann M., 2005, *ApJ*, **622**, 759
- Green D. A., 2019, *VizieR Online Data Catalog*, p. VII/284
- Hamaker J. P., Bregman J. D., 1996, *A&AS*, **117**, 161
- Hanbury Brown R., Hazard C., 1952, *Nature*, **170**, 364
- Harper S. E., et al., 2022, *MNRAS*, **513**, 5900
- Harris D. E., 1962, *ApJ*, **135**, 661
- Harris D. E., Roberts J. A., 1960, *PASP*, **72**, 237
- Harris C. R., et al., 2020, *Nature*, **585**, 357
- Haslam C. G. T., Salter C. J., Stoffel H., Wilson W. E., 1982, *A&AS*, **47**, 1
- Hauser M. G., et al., 1998, *ApJ*, **508**, 25
- Hayato A., et al., 2010, *ApJ*, **725**, 894
- Herman D., et al., 2022, arXiv e-prints, p. arXiv:2201.03530
- Hester J. J., Cox D. P., 1986, *ApJ*, **300**, 675
- Hester J. J., Raymond J. C., Danielson G. E., 1986, *ApJ*, **303**, L17
- Hildebrand R. H., 1983, *QJRAS*, **24**, 267
- Hill L. E., 1974, *MNRAS*, **169**, 59
- Hobbs G., Lyne A. G., Kramer M., Martin C. E., Jordan C., 2004, *MNRAS*, **353**, 1311
- Hoyland R. J., et al., 2012, in *Millimeter, Submillimeter, and Far-Infrared Detectors and Instrumentation for Astronomy VI*. p. 845233, doi:10.1117/12.925349
- Hoyland R. J., et al., 2022, in Zmuidzinas J., Gao J.-R., eds., *Society of Photo-Optical Instrumentation Engineers (SPIE) Conference Series Vol. 12190, Millimeter, Submillimeter, and Far-Infrared Detectors and Instrumentation for Astronomy XI*. p. 1219033, doi:10.1117/12.2640826
- Hunter J. D., 2007, *Computing in Science & Engineering*, **9**, 90
- Hurley-Walker N., et al., 2009, *MNRAS*, **396**, 365
- Irfan M. O., et al., 2015, *MNRAS*, **448**, 3572
- Jones M. E., et al., 2018, *MNRAS*, **480**, 3224
- Kamionkowski M., Kosowsky A., Stebbins A., 1997, *Phys. Rev. D*, **55**, 7368
- Katagiri H., et al., 2011, *ApJ*, **741**, 44
- Katsuda S., et al., 2011, *ApJ*, **730**, 24
- Katz-Stone D. M., Kassim N. E., Lazio T. J. W., O'Donnell R., 2000, *ApJ*, **529**, 453
- Knoedseder J., Oberlack U., Diehl R., Chen W., Gehrels N., 1996, *A&AS*, **120**, 339
- Kogut A., Banday A. J., Bennett C. L., Gorski K. M., Hinshaw G., Smoot G. F., Wright E. I., 1996, *ApJ*, **464**, L5
- Kogut A., et al., 2007, *ApJ*, **665**, 355
- Koo B.-C., Heiles C., 1991, *ApJ*, **382**, 204
- Koo B.-C., Reach W. T., Heiles C., Fesen R. A., Shull J. M., 1990, *ApJ*, **364**, 178
- Kothes R., Fedotov K., Foster T. J., Uyaniker B., 2006, *A&A*, **457**, 1081
- Krause O., Tanaka M., Usuda T., Hattori T., Goto M., Birkmann S., Nomoto K., 2008, *Nature*, **456**, 617
- Ku W. H. M., Kahn S. M., Pisarski R., Long K. S., 1984, *ApJ*, **278**, 615
- Kulkarni S. R., Clifton T. C., Backer D. C., Foster R. S., Fruchter A. S., 1988, *Nature*, **331**, 50
- Kundu M. R., Becker R. H., 1972, *AJ*, **77**, 459
- Kundu M. R., Becker R. H., Velusamy T., 1973, *AJ*, **78**, 170
- Landecker T. L., et al., 2010, *A&A*, **520**, A80
- Lazarian A., Draine B. T., 2000, *ApJ*, **536**, L15
- Lazendic J. S., Slane P. O., 2006, *ApJ*, **647**, 350
- Leahy D. A., Aschenbach B., 1995, *A&A*, **293**, 853
- Leahy D. A., Aschenbach B., 1996, *A&A*, **315**, 260
- Leahy D., Hassan M., 2013, *ApJ*, **764**, 55
- Leahy D. A., Ranasinghe S., 2012, *MNRAS*, **423**, 718
- Leahy D. A., Roger R. S., 1991, *AJ*, **101**, 1033
- Leahy D. A., Roger R. S., 1998, *ApJ*, **505**, 784
- Leahy D. A., Tian W. W., 2007, *A&A*, **461**, 1013
- Leahy D. A., Roger R. S., Ballantyne D., 1997, *AJ*, **114**, 2081
- Leitch E. M., Readhead A. C. S., Pearson T. J., Myers S. T., 1997, *ApJ*, **486**, L23+
- Levenson N. A., et al., 1997, *ApJ*, **484**, 304
- Levenson N. A., Graham J. R., Keller L. D., Richter M. J., 1998, *ApJS*, **118**, 541
- Li J., Torres D. F., de Oña Wilhelmi E., Rea N., Martin J., 2016, *ApJ*, **831**, 19

- Li X.-H., Sun X.-H., Reich W., Gao X.-Y., 2020, *Research in Astronomy and Astrophysics*, **20**, 186
- Lin L. C. C., et al., 2012, *MNRAS*, **426**, 2283
- López-Caraballo C. H., Rubiño-Martín J. A., Rebolo R., Génova-Santos R., 2011, *ApJ*, **729**, 25
- Loru S., et al., 2019, *MNRAS*, **482**, 3857
- Loru S., et al., 2021, *MNRAS*, **500**, 5177
- Lozinskaia T. A., 1975, *Azh*, **52**, 39
- Lozinskaia T. A., 1980, *A&A*, **84**, 26
- Lubin P. M., Epstein G. L., Smoot G. F., 1983, *Physical Review Letters*, **50**, 616
- Macellari N., Pierpaoli E., Dickinson C., Vaillancourt J. E., 2011, *MNRAS*, **418**, 888
- Mantovani F., Reich W., Salter C. J., Tomasi P., 1985, *A&A*, **145**, 50
- Martín J., Torres D. F., Pedalotti G., 2016, *MNRAS*, **459**, 3868
- Mavromatakis F., Ventura J., Paleologou E. V., Papamastorakis J., 2001, *A&A*, **371**, 300
- Mavromatakis F., Xilouris E. M., Boumis P., 2007, *A&A*, **461**, 991
- Migliazzo J. M., Gaensler B. M., Backer D. C., Stappers B. W., van der Swaluw E., Strom R. G., 2002, *ApJ*, **567**, L141
- Mignani R. P., de Luca A., Rea N., Shearer A., Collins S., Torres D. F., Hadasch D., Caliendo A., 2013, *MNRAS*, **430**, 1354
- Minkowski R., 1958, *Reviews of Modern Physics*, **30**, 1048
- Miyata E., Tsunemi H., Pisarski R., Kissel S. E., 1994, *PASJ*, **46**, L101
- Nashimoto M., Hattori M., Poidevin F., Génova-Santos R., 2020, *ApJ*, **900**, L40
- Oster L., 1961a, *AJ*, **66**, 50
- Oster L., 1961b, *ApJ*, **134**, 1010
- Pacholczyk A. G., 1970, Radio astrophysics. Nonthermal processes in galactic and extragalactic sources
- Paradis D., Dobashi K., Shimoikura T., Kawamura A., Onishi T., Fukui Y., Bernard J. P., 2012, *A&A*, **543**, A103
- Peel M. W., Genova-Santos R., Dickinson C., Leahy J. P., López-Caraballo C., Fernández-Torreiro M., Rubiño-Martín J. A., Spencer L. D., 2022, *Research Notes of the American Astronomical Society*, **6**, 252
- Penzias A. A., Wilson R. W., 1965, *ApJ*, **142**, 419
- Pérez-de-Taoro M. R., et al., 2016, in Ground-based and Airborne Telescopes VI. p. 99061K, doi:10.1117/12.2233225
- Pineault S., Landecker T. L., Madore B., Gaumont-Guay S., 1993, *AJ*, **105**, 1060
- Pineault S., Landecker T. L., Swerdlyk C. M., Reich W., 1997, *A&A*, **324**, 1152
- Pivato G., et al., 2013, *ApJ*, **779**, 179
- Planck Collaboration et al., 2014, *A&A*, **565**, A103
- Planck Collaboration et al., 2016a, *A&A*, **586**, A134
- Planck Collaboration et al., 2016b, *A&A*, **594**, A25
- Planck Collaboration et al., 2020, *A&A*, **641**, A1
- Plaszczynski S., Montier L., Levrier F., Tristram M., 2014, *MNRAS*, **439**, 4048
- Platania P., Burigana C., Maino D., Caserini E., Bersanelli M., Cappellini B., Mennella A., 2003, *A&A*, **410**, 847
- Poidevin F., et al., 2023, *MNRAS*, **519**, 3481
- Ramanamurthy P. V., et al., 1995, *ApJ*, **447**, L109
- Ranasinghe S., Leahy D., 2023, *arXiv e-prints*, p. arXiv:2302.06593
- Reich P., Reich W., 1986, *A&AS*, **63**, 205
- Reich W., Fuerst E., Sieber W., 1983, in Danziger J., Gorenstein P., eds, Vol. 101, *Supernova Remnants and their X-ray Emission*. pp 377–379
- Reich P., Testori J. C., Reich W., 2001, *A&A*, **376**, 861
- Reich W., Zhang X., Fürst E., 2003, *A&A*, **408**, 961
- Rennie T. J., et al., 2022, *ApJ*, **933**, 187
- Rest A., et al., 2008, *ApJ*, **681**, L81
- Reynolds S. P., 2009, *ApJ*, **703**, 662
- Reynolds S. P., Ellison D. C., 1992, *ApJ*, **399**, L75
- Reynoso E. M., Moffett D. A., Goss W. M., Dubner G. M., Dickel J. R., Reynolds S. P., Giacani E. B., 1997, *ApJ*, **491**, 816
- Reynoso E. M., Hughes J. P., Moffett D. A., 2013, *AJ*, **145**, 104
- Rohlf K., 1990, Tools of Radio Astronomy
- Romero G. E., Benaglia P., Torres D. F., 1999, *A&A*, **348**, 868
- Rubakov V. A., Sazhin M. V., Veryaskin A. V., 1982, *Physics Letters B*, **115**, 189
- Rubiño-Martín J. A., López-Caraballo C. H., Génova-Santos R., Rebolo R., 2012a, *Advances in Astronomy*, **2012**, 351836
- Rubiño-Martín J. A., et al., 2012b, in Ground-based and Airborne Telescopes VI. p. 84442Y, doi:10.1117/12.926581
- Rubiño-Martín J. A., et al., 2023, *MNRAS*, **519**, 3383
- Ruiz-Granados B., et al., 2023, *MNRAS*, in prep.
- Rybicki G. B., Lightman A. P., 1979, Radiative processes in astrophysics
- Safi-Harb S., Ogelman H., Finley J. P., 1995, *ApJ*, **439**, 722
- Saito M., Yamauchi S., Nobukawa K. K., Bamba A., Pannuti T. G., 2020, *PASJ*, **72**, 65
- Sanquircé-García R., et al., 2016, in Ground-based and Airborne Telescopes VI. p. 99064N, doi:10.1117/12.2232644
- Sanquircé R., et al., 2014, in Ground-based and Airborne Telescopes V. p. 914524, doi:10.1117/12.2056615
- Sazonov V. N., 1973, *Soviet Ast.*, **16**, 774
- Scaife A., et al., 2007, *MNRAS*, **377**, L69
- Seward F. D., Schmidt B., Slane P., 1995, *ApJ*, **453**, 284
- Sezer A., Ergin T., Yamazaki R., Sano H., Fukui Y., 2019, *MNRAS*, **489**, 4300
- Shan S. S., Zhu H., Tian W. W., Zhang M. F., Zhang H. Y., Wu D., Yang A. Y., 2018, *ApJS*, **238**, 35
- Shinn J.-H., Koo B.-C., Burton M. G., Lee H.-G., Moon D.-S., 2009, *ApJ*, **693**, 1883
- Sieber W., Haslam C. G. T., Salter C. J., 1979, *A&A*, **74**, 361
- Sieber W., Salter C. J., Mayer C. J., 1981, *A&A*, **103**, 393
- Simonetti J. M., 1992, *ApJ*, **386**, 170
- Slane P., Seward F. D., Bandiera R., Torii K., Tsunemi H., 1997, *ApJ*, **485**, 221
- Slane P., Zimmerman E. R., Hughes J. P., Seward F. D., Gaensler B. M., Clarke M. J., 2004, *ApJ*, **601**, 1045
- Smoot G. F., et al., 1992, *ApJ*, **396**, L1
- Sofue Y., Takahara F., Hirabayashi H., Inoue M., Nakai N., 1983, *PASJ*, **35**, 437
- Sokoloff D. D., Bykov A. A., Shukurov A., Berkhuijsen E. M., Beck R., Poezd A. D., 1998, *MNRAS*, **299**, 189
- Starobinsky A. A., 1979, *Soviet Journal of Experimental and Theoretical Physics Letters*, **30**, 682
- Stevenson M. A., 2014, *ApJ*, **781**, 113
- Strom R. G., 1987, *ApJ*, **319**, L103
- Sun X. H., Reich W., Han J. L., Reich P., Wielebinski R., 2006, *A&A*, **447**, 937
- Sun X. H., Han J. L., Reich W., Reich P., Shi W. B., Wielebinski R., Fürst E., 2007, *A&A*, **463**, 993
- Sun X. H., Reich W., Han J. L., Reich P., Wielebinski R., Wang C., Müller P., 2011a, *A&A*, **527**, A74
- Sun X. H., Reich P., Reich W., Xiao L., Gao X. Y., Han J. L., 2011b, *A&A*, **536**, A83
- Suzuki H., Bamba A., Shibata S., 2021, *ApJ*, **914**, 103
- Tatematsu K., Fukui Y., Landecker T. L., Roger R. S., 1990, *A&A*, **237**, 189
- Taylor A. R., Stil J. M., Sunstrum C., 2009, *ApJ*, **702**, 1230
- Tian W. W., Leahy D. A., 2011, *ApJ*, **729**, L15
- Torres D. F., Romero G. E., Dame T. M., Combi J. A., Butt Y. M., 2003, *Phys. Rep.*, **382**, 303
- Tramonte D., et al., 2023, *MNRAS*, **519**, 3432
- Tuohy I. R., Clark D. H., Garmire G. P., 1979, *MNRAS*, **189**, 59P
- Uyaniker B., Reich W., Yar A., Kothes R., Fürst E., 2002, *A&A*, **389**, L61
- Uyaniker B., Reich W., Yar A., Fürst E., 2004, *A&A*, **426**, 909
- Vaillancourt J. E., 2006, *PASP*, **118**, 1340
- Velusamy T., Kundu M. R., 1974, *A&A*, **32**, 375
- Vink J., 2020, Physics and Evolution of Supernova Remnants, doi:10.1007/978-3-030-55231-2.
- Virtanen P., et al., 2020, *Nature Methods*, **17**, 261
- Webb G. M., Drury L. O., Biermann P., 1984, *A&A*, **137**, 185
- Weiland J. L., et al., 2011, *ApJS*, **192**, 19
- Weisberg J. M., Cordes J. M., Kuan B., Devine K. E., Green J. T., Backer D. C., 2004, *ApJS*, **150**, 317

- Wenger M., et al., 2000, *A&AS*, **143**, 9
- Willis A. G., 1973, *A&A*, **26**, 237
- Wolleben M., Landecker T. L., Reich W., Wielebinski R., 2006, *A&A*, **448**, 411
- Xiao L., Han J. L., Reich W., Sun X. H., Wielebinski R., Reich P., Shi H., Lochner O., 2011, *A&A*, **529**, A15
- Yamauchi S., Koyama K., 1993, *PASJ*, **45**, 545
- Zaldarriaga M., Seljak U., 1997, *Phys. Rev. D*, **55**, 1830
- Zeiger B. R., Brisken W. F., Chatterjee S., Goss W. M., 2008, *ApJ*, **674**, 271
- Zeng H., Xin Y., Liu S., 2019, *ApJ*, **874**, 50
- Zhao H., Jiang B., Li J., Chen B., Yu B., Wang Y., 2020, *ApJ*, **891**, 137
- Zonca A., Singer L., Lenz D., Reinecke M., Rosset C., Hivon E., Gorski K., 2019, *Journal of Open Source Software*, **4**, 1298

## ONLINE MATERIAL

### APPENDIX A: FLUX DENSITIES AND IMAGES OF OUR SNRS SAMPLE

This section provides the tables with the raw intensity and polarization flux densities (without colour correction) measured for our six SRNs, using the aperture photometry method described in section 5. In addition, we also provide the intensity and polarization (Stokes  $Q$ ,  $U$  and  $P$ ) maps of the six Galactic SNRs studied in this paper. The selected maps range from the radio up the far infrared in intensity and polarization, with the purpose of showing the morphology variations of SNRs across the whole frequency range. In particular, we consider maps from the QUIJOTE-MFI survey and other maps to be useful for the description of the SNRs (see details in Section 5) mainly from the WMAP and *Planck*. The apertures values (Table 4) and masks used to recover the flux densities are drawn in each case. Tables and maps are displayed for CTB 80 (Table A1 and Figure A1), for Cygnus Loop (Table A2 and Figure A2), for HB 21 (Table A3 and Figure A3), for CTA 1 (Table A4 and Figure A4), for Tycho (Table A5 and Figure A5), and for HB 9 (Table A6 and Figure A6).

### APPENDIX B: SYNCHOTRON MODELS WITH CURVED SPECTRA

As mentioned in section 4.2, we selected a smooth broken power-law function (SBPL, equation 6) to characterize the curved spectra observed for CTB 80 and HB 21. Here, we present the parametric representation of other functions to describe the curved spectrum observed in SNRs based on a power-law function (with spectral index  $\alpha$ , equation 5) that dominates at lower frequencies, and then decreases further at high frequencies.

The power law with an exponential cut-off function has been considered in previous SED analyses in the microwave range (e.g. Pivato et al. 2013; Loru et al. 2021; Tramonte et al. 2023). This behaviour is expected when the energy losses exceed the rate of energy gain from shock acceleration (Webb et al. 1984), although the break frequency is commonly at high energies. This function can be written as:

$$S_{\text{PLcutoff}}(\nu; A_{\text{syn}}, \alpha, \nu_c) = A_{\text{syn}} \left( \frac{\nu}{\nu_{\text{ref}}} \right)^\alpha e^{-\frac{\nu - \nu_{\text{ref}}}{\nu_c}}, \quad (\text{B1})$$

where  $\nu_c$  is the cut-off frequency and  $A_{\text{syn}}$  is the amplitude normalised to the reference frequency  $\nu_{\text{ref}}$ . Alternatively, the Rolloff function also describes a smoothed decay from low to high frequencies. Weiland et al. (2011) used this function to model the SED of 3C 58, which is parametrized as follows:

$$S_{\text{Rf}}(\nu; A_{\text{syn}}, b, c, d) = A_{\text{syn}} \left( \frac{\nu}{\nu_{\text{ref}}} \right)^b \frac{1+c}{1+c(\nu/\nu_{\text{ref}})^d}, \quad (\text{B2})$$

where  $b$ ,  $c$  and  $d$  define the shape at high and low frequencies (it is also normalised to  $\nu_{\text{ref}}$ ).

Since the observed spectra of CTB 80 and HB 21 follow a clear power-law behaviour in the QUIJOTE-MFI frequency range, we also explored the broken power-law function with a sudden spectral

index variation at  $\nu_b$ :

$$S_{\text{BPL}}(\nu; A_{\text{syn}}, \alpha_{\text{bb}}, \alpha_{\text{ab}}, \nu_b) = A_{\text{syn}} \begin{cases} \left( \frac{\nu}{\nu_{\text{ref}}} \right)^{\alpha_{\text{bb}}} & , \quad \nu \leq \nu_b \\ \left( \frac{\nu_b}{\nu_{\text{ref}}} \right)^{\alpha_{\text{bb}}} \left( \frac{\nu}{\nu_b} \right)^{\alpha_{\text{ab}}} & , \quad \nu > \nu_b, \end{cases} \quad (\text{B3})$$

where  $\alpha_{\text{bb}}$  and  $\alpha_{\text{ab}}$  are respectively the spectral indices below and above of the break frequency. We choose this function as the final parametric shape to model our curved spectra, although with a smoothed spectral break (SBPL, equation 6). For the SBPL spectral model, the parameter  $m$  drives the level of smoothing around the break frequency (see Figure B1). In this figure, we observe that the SBPL model converges to the BPL model as  $m$  increases. For instance,  $m = 10$  provides a close concordance between the SBPL and BPL spectral models.

### APPENDIX C: MEASUREMENTS FROM THE LITERATURE: CTB 80 AND HB 21

For HB 21 and CTB 80, we use literature measurements of the intensity flux densities for frequencies below the Q11 band, which allow us to improve the fit of their broken spectrum. For CTB 80, we take into account flux densities between 0.01 and 11 GHz compiled by Gao et al. (2011), with frequencies up to 10.2 GHz (Sofue et al. 1983). We excluded measurements at frequencies lower than 200 MHz to avoid modelling the low-frequency turnover due to the free-free thermal absorption (proposed by Castelletti & Dubner 2005). For HB 21, we consider the flux densities used by Kothes et al. (2006) and Pivato et al. (2013) covering frequencies below 5 GHz (Gao et al. 2011). In general, the literature information must be treated carefully in the SED fitting, mainly, owing to the wide range of systematic effects affecting each measurement, which also encompass the differences of the beam resolution of maps and methodologies for recover the flux densities. Therefore, we consider conservative uncertainties for those flux densities taken from the literature, which consists in increasing the uncertainty up to 10% of the intensity signal when the literature error bars are less than this threshold of 10%. Table C1 shows the flux densities from the literature used in the SED fits of CTB 80 (section 5.1) and HB 21 (section 5.3).

This paper has been typeset from a  $\text{\TeX}/\text{\LaTeX}$  file prepared by the author.

**Table A1.** Summary of recovered flux densities for CTB 80. The  $P$ ,  $\Pi$  and  $\gamma$  are obtained from the raw flux densities (second, third and fourth columns).

$\nu$ [GHz]	$I$ [Jy]	$Q$ [Jy]	$U$ [Jy]	$P$ [Jy]	$\gamma$ [deg]	$\Pi$ [%]
0.408	109±13	-	-	-	-	-
0.820	47.1±7.1	-	-	-	-	-
1.420	54.9±8.4	-	-	-	-	-
2.720	45.9±5.6	-	-	-	-	-
4.800	45.0±5.8	-1.11±0.13	0.24±0.10	1.13±0.13	-83.9±3	2.5±0.4
11.1	21.4±3.4	-0.16±0.15	-0.78±0.17	0.78±0.17	50.8±6	3.6±1.0
12.9	19.2±3.5	0.04±0.16	-0.73±0.16	0.71±0.16	43.4±7	3.8±1.1
16.8	15.5±3.5	-0.33±0.23	-0.72±0.20	0.76±0.21	57.3±8	5.1 <sup>1.8</sup> <sub>1.9</sub>
18.8	11.7±3.5	-0.38±0.22	-0.80±0.37	0.85±0.36	57.7±12	7.7 <sup>3.4</sup> <sub>3.6</sub>
22.8	13.9±3.6	-0.02±0.06	-0.67±0.13	0.67±0.13	45.9±6	5.1 <sup>1.3</sup> <sub>1.4</sub>
28.4	11.7±3.4	-0.07±0.07	-0.57±0.09	0.57±0.09	48.5±5	5.2 <sup>1.6</sup> <sub>1.4</sub>
32.9	11.8±3.3	-0.09±0.13	-0.53±0.11	0.52±0.11	49.8±6	4.8±1.6
40.7	10.5±3.2	-0.04±0.11	-0.39±0.11	0.38±0.11	47.9±9	4.1 <sup>1.8</sup> <sub>1.4</sub>
44.1	10.0±3.1	0.16±0.08	-0.21±0.05	0.25±0.07	26.4±7	2.8 <sup>1.1</sup> <sub>1.0</sub>
60.7	7.8±3.4	0.60±0.14	-0.75±0.41	0.92±0.35	25.7±11	13.3 <sup>5.4</sup> <sub>6.6</sub>
70.4	5.7±4.4	0.11±0.13	-0.35±0.15	0.34±0.16	36.3±13	<18.2
93.5	4.3±8.3	0.51±0.69	-0.65±0.78	0.59±1.04	25.9±50	<115.9
100	4±11	0.46±0.17	-0.16±0.15	0.46±0.18	9.6±11	<120.6
143	4±23	2.18±0.56	0.15±0.36	2.16±0.57	-2.0±8	-
217	0±75	7.76±2.30	0.87±1.38	7.68±2.33	-3.2±9	-
353	8±280	35.04±11.13	2.60±6.44	34.54±11.30	-2.1±9	-
545	36±829	-	-	-	-	-
857	-298±2507	-	-	-	-	-
1249	-1303±4998	-	-	-	-	-
2141	1938±7229	-	-	-	-	-
2997	2157±3779	-	-	-	-	-

**Table A2.** Summary of recovered flux densities for the Cygnus Loop. The  $P$ ,  $\Pi$  and  $\gamma$  are obtained from the raw flux densities (second, third and fourth columns).

$\nu$ [GHz]	$I$ [Jy]	$Q$ [Jy]	$U$ [Jy]	$P$ [Jy]	$\gamma$ [deg]	$\Pi$ [%]
0.408	199±21	-	-	-	-	-
0.820	159±16	-	-	-	-	-
1.420	121±13	-	-	-	-	-
2.720	98±10	-	-	-	-	-
11.1	45.7±3.9	-1.33±0.75	3.55±0.72	3.72±0.74	34.7±6	8.2 <sup>1.8</sup> <sub>1.7</sub>
12.9	42.6±3.9	-1.32±0.46	3.28±0.80	3.50±0.77	34.0±6	8.3±1.6
16.8	30.1±3.8	-0.31±0.58	2.37±0.62	2.32±0.64	41.3±8	7.8 <sup>2.4</sup> <sub>2.2</sub>
18.8	21.3±8.4	-0.12±0.65	2.11±0.44	2.01±0.46	43.4±7	10.5 <sup>4.3</sup> <sub>4.8</sub>
22.8	34.0±2.2	-0.44±0.20	1.76±0.18	1.80±0.18	38.0±3	5.3±0.7
28.4	29.3±1.8	-0.25±0.22	1.59±0.29	1.59±0.29	40.5±5	5.4 <sup>1.0</sup> <sub>0.9</sub>
32.9	26.5±1.8	-0.50±0.30	1.62±0.33	1.67±0.33	36.4±6	6.2±1.3
40.7	24.6±1.6	-0.73±0.34	1.71±0.28	1.83±0.29	33.4±5	7.5 <sup>1.4</sup> <sub>1.3</sub>
44.1	23.9±1.6	-0.77±0.42	0.64±0.34	0.93±0.42	19.9±13	3.9 <sup>1.8</sup> <sub>1.6</sub>
60.7	21.0±1.8	-0.79±0.65	1.56±0.59	1.63±0.65	31.6±11	7.7 <sup>3.4</sup> <sub>3.1</sub>
70.4	20.2±2.1	-1.14±0.75	1.22±0.65	1.52±0.77	23.5±14	7.3 <sup>4.1</sup> <sub>3.5</sub>
93.5	17.6±4.2	4.20±2.29	2.95±2.84	4.45±2.86	-17.5±18	<54.8
100	30.8±5.5	-0.89±0.44	1.49±0.42	1.68±0.44	29.6±7	5.6 <sup>1.7</sup> <sub>1.8</sub>
143	35±13	0.28±0.76	1.61±0.86	1.46±0.96	-40.1±19	4.5 <sup>3.2</sup> <sub>2.6</sub>
217	124±54	1.28±4.15	7.36±3.11	6.38±3.69	-40.1±17	5.8 <sup>4.0</sup> <sub>3.7</sub>
353	453±240	7.60±13.85	28.29±15.32	26.01±17.15	-37.5±19	<15.5
545	1562±526	-	-	-	-	-
857	4616±1528	-	-	-	-	-
1249	9033±2978	-	-	-	-	-
2141	9989±3315	-	-	-	-	-
2997	2569±1271	-	-	-	-	-

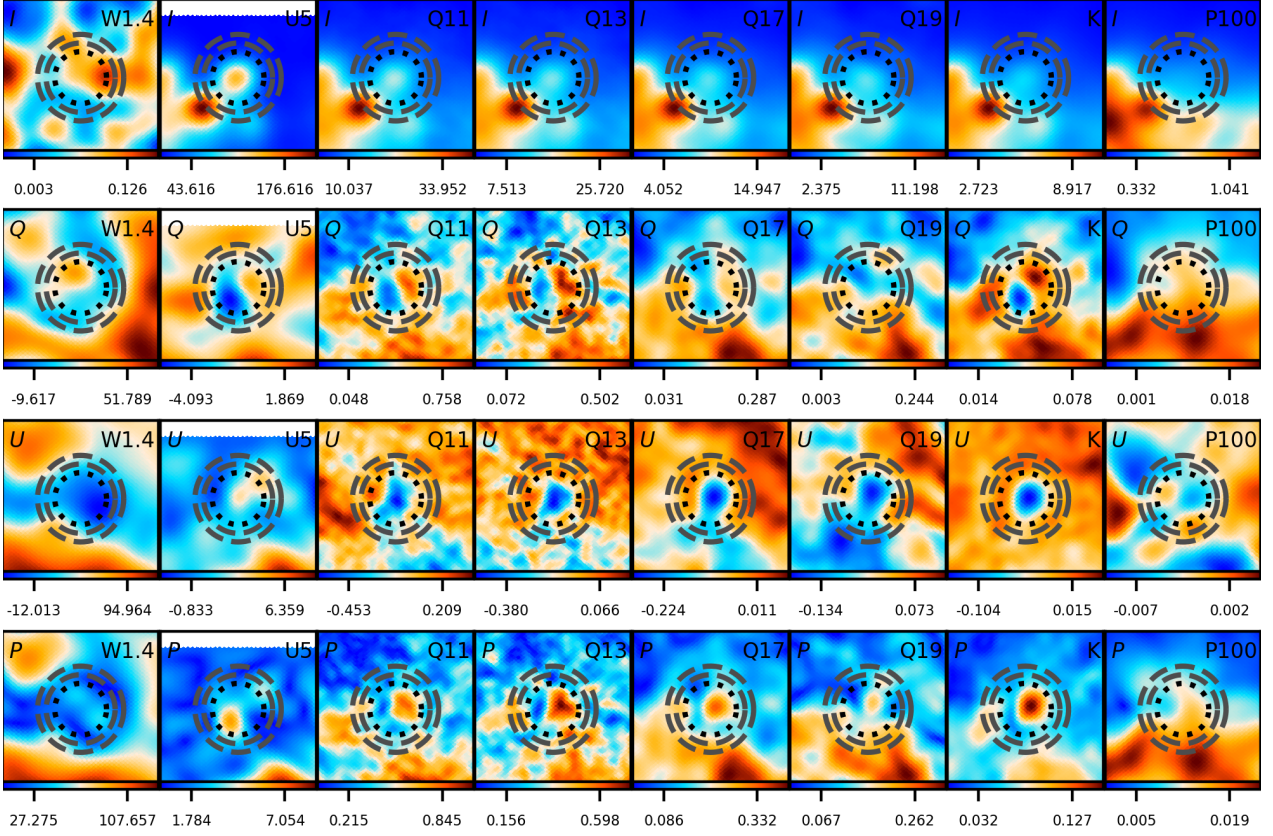


**Figure A1.** Intensity and polarization maps of CTB 80 from the Urumqi, QUIJOTE, WMAP and *Planck* data. Maps are smoothed to an angular resolution of 1 deg, and centred on  $l, b = 68.8^\circ, 2.7^\circ$  with a field of view of  $6.0^\circ \times 6.0^\circ$  (Galactic coordinate system).

**Table A3.** Summary of recovered flux densities for HB 21. The  $P$ ,  $\Pi$  and  $\gamma$  are obtained from the raw flux densities (second, third and fourth columns).

$\nu$ [GHz]	$I$ [Jy]	$Q$ [Jy]	$U$ [Jy]	$P$ [Jy]	$\gamma$ [deg]	$\Pi$ [%]
0.408	255±26	-	-	-	-	-
0.820	191±20	-	-	-	-	-
1.420	189±20	-	-	-	-	-
11.1	55.6±3.5	3.33±0.22	-0.08±0.22	3.32±0.22	0.7±2	5.9±0.6
12.9	50.1±3.3	2.73±0.32	-0.01±0.17	2.72±0.32	0.1±3	5.4±0.6
16.8	42.1±3.1	2.05±0.23	-0.03±0.26	2.03±0.23	0.4±3	4.8±0.7
18.8	36.0±2.8	1.99±0.16	-0.11±0.22	1.98±0.16	1.6±2	5.4±0.7
22.8	32.6±2.4	1.53±0.09	-0.45±0.11	1.59±0.09	8.2±2	4.9±0.5
28.4	26.6±2.1	1.23±0.09	-0.38±0.13	1.28±0.09	8.6±2	4.8±0.6
32.9	24.2±2.0	1.00±0.13	-0.13±0.12	1.00±0.13	3.7±4	4.1±0.6
40.7	21.0±1.9	1.02±0.16	-0.46±0.16	1.11±0.16	12.1±4	5.3±0.9
44.1	19.6±2.2	0.67±0.13	-0.23±0.11	0.70±0.13	9.5±5	3.6 <sub>0.7</sub> <sup>0.8</sup>
60.7	14.8±4.2	-0.03±0.56	0.08±0.40	0.04±0.84	-	<6.7
70.4	13.0±5.6	0.28±0.26	-0.30±0.27	0.33±0.33	23.5±28	<7.4
93.5	13.7±8.8	3.30±1.17	0.12±1.78	2.84±1.36	-1.0±14	<62.8
100	5±13	0.56±0.17	0.17±0.30	0.51±0.21	-8.4±12	<74.3
143	31±18	0.83±0.78	0.70±0.96	0.80±1.16	-20.1±41	<9.7
217	116±62	2.57±3.43	2.09±3.72	2.19±5.36	-19.6±70	<8.8
353	640±271	10.63±16.21	5.12±17.04	7.13±27.08	-	<6.4
545	1896±892	-	-	-	-	-
857	4291±2485	-	-	-	-	-
1249	9658±4521	-	-	-	-	-
2141	8733±5144	-	-	-	-	-
2997	-616±2056	-	-	-	-	-

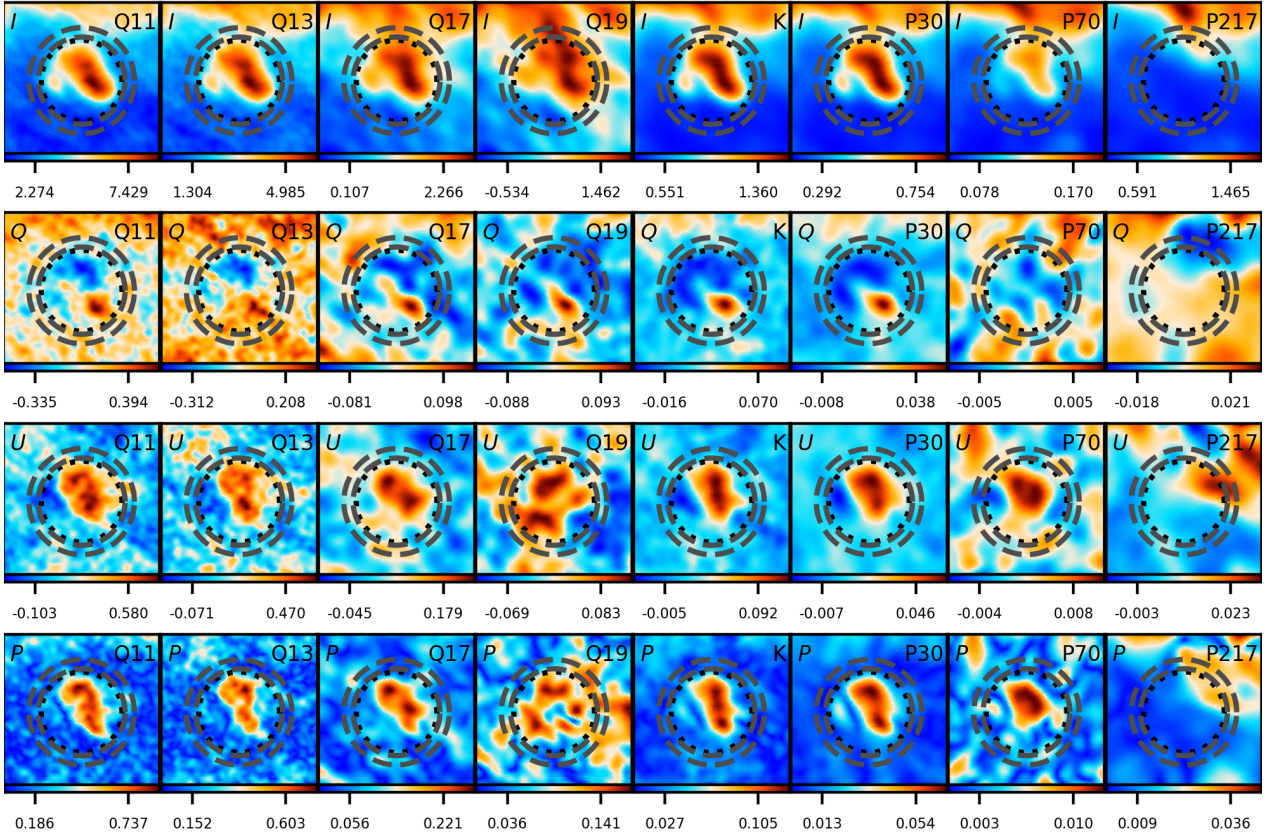


**Figure A2.** Intensity and polarization maps of Cygnus Loop from the QUIJOTE, WMAP and *Planck* data. Maps are smoothed to an angular resolution of 1 deg, and centred on  $l, b = 73.9^\circ, -8.8^\circ$  with a field of view of  $8.4^\circ \times 8.4^\circ$  (Galactic coordinate system).

**Table A4.** Summary of recovered flux densities for CTA 1. The  $P$ ,  $\Pi$  and  $\gamma$  are obtained from the raw flux densities (second, third and fourth columns).

$\nu$ [GHz]	$I$ [Jy]	$Q$ [Jy]	$U$ [Jy]	$P$ [Jy]	$\gamma$ [deg]	$\Pi$ [%]
0.408	44.6 $\pm$ 4.9	-	-	-	-	-
0.820	33.1 $\pm$ 3.5	-	-	-	-	-
1.420	27.5 $\pm$ 2.9	-	-	-	-	-
11.1	9.0 $\pm$ 1.4	-0.48 $\pm$ 0.18	-1.05 $\pm$ 0.32	1.14 $\pm$ 0.31	-32.7 $\pm$ 8	12.4 $^{3.2}_{3.6}$
12.9	7.6 $\pm$ 1.8	-0.37 $\pm$ 0.21	-0.91 $\pm$ 0.15	0.96 $\pm$ 0.16	-33.9 $\pm$ 5	13.4 $^{3.8}_{3.9}$
16.8	6.1 $\pm$ 1.6	0.20 $\pm$ 0.32	-0.64 $\pm$ 0.25	0.60 $\pm$ 0.29	36.3 $\pm$ 14	10.4 $^{6.0}_{5.6}$
18.8	9.3 $\pm$ 2.1	-0.22 $\pm$ 0.65	0.40 $\pm$ 0.40	0.28 $\pm$ 0.76	30.6 $\pm$ 77	<13.5
22.8	6.5 $\pm$ 1.4	-0.16 $\pm$ 0.07	-0.47 $\pm$ 0.09	0.49 $\pm$ 0.09	-35.6 $\pm$ 5	7.7 $^{1.9}_{2.1}$
28.4	5.8 $\pm$ 1.2	-0.34 $\pm$ 0.05	-0.44 $\pm$ 0.08	0.55 $\pm$ 0.07	-26.1 $\pm$ 4	9.8 $^{2.2}_{2.3}$
32.9	5.7 $\pm$ 1.4	-0.27 $\pm$ 0.12	-0.36 $\pm$ 0.15	0.43 $\pm$ 0.15	-26.6 $\pm$ 10	7.9 $\pm$ 3.2
40.7	5.0 $\pm$ 1.3	0.13 $\pm$ 0.18	0.22 $\pm$ 0.32	0.18 $\pm$ 0.40	-29.7 $\pm$ 63	<12.8
44.1	5.1 $\pm$ 1.6	0.35 $\pm$ 0.13	-0.15 $\pm$ 0.18	0.34 $\pm$ 0.15	11.6 $\pm$ 13	7.3 $^{4.1}_{3.8}$
60.7	5.4 $\pm$ 3.1	-0.36 $\pm$ 0.42	-0.98 $\pm$ 0.37	0.96 $\pm$ 0.41	-34.9 $\pm$ 12	<46.4
70.4	5.2 $\pm$ 4.0	-0.05 $\pm$ 0.33	0.21 $\pm$ 0.25	0.13 $\pm$ 0.43	-	<16.1
93.5	6.0 $\pm$ 6.1	-0.91 $\pm$ 1.29	-1.17 $\pm$ 1.58	1.03 $\pm$ 2.12	-26.1 $\pm$ 59	<96.3
100	4 $\pm$ 11	-0.30 $\pm$ 0.19	-0.12 $\pm$ 0.30	0.23 $\pm$ 0.29	-10.9 $\pm$ 36	<69.0
143	5 $\pm$ 16	0.08 $\pm$ 0.86	-0.03 $\pm$ 0.89	0.04 $\pm$ 1.72	-	<39.7
217	4 $\pm$ 59	-2.27 $\pm$ 3.03	0.84 $\pm$ 2.98	1.53 $\pm$ 4.77	10.2 $\pm$ 89	-
353	-50 $\pm$ 215	-6.45 $\pm$ 13.60	0.99 $\pm$ 17.88	3.47 $\pm$ 25.77	-	-
545	-231 $\pm$ 210	-	-	-	-	-
857	-657 $\pm$ 609	-	-	-	-	-
1249	-585 $\pm$ 1086	-	-	-	-	-
2141	281 $\pm$ 1238	-	-	-	-	-
2997	250 $\pm$ 545	-	-	-	-	-

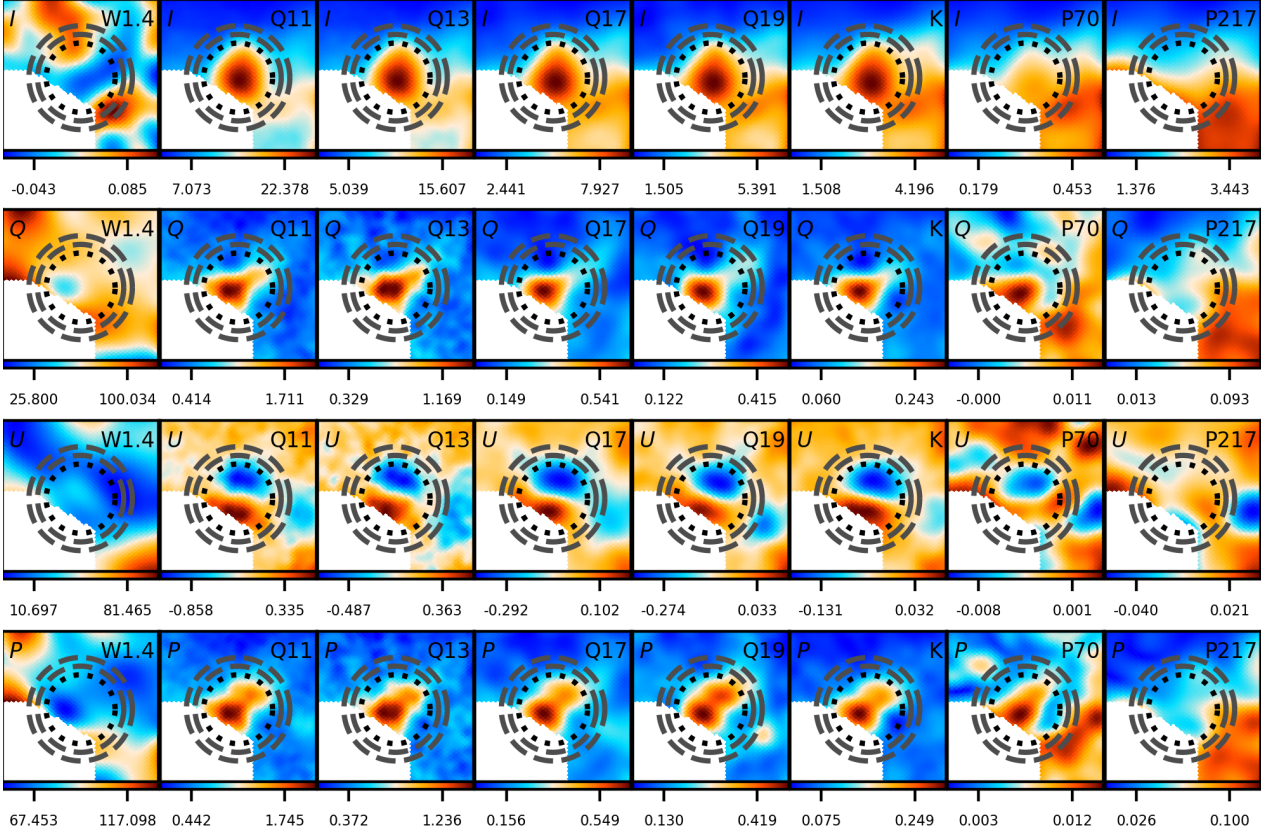


**Figure A3.** Intensity and polarization maps of HB 21 from the QUIJOTE, WMAP and *Planck* data. Maps are smoothed to an angular resolution of 1 deg, and centred on  $l, b = 89.0^\circ, 4.7^\circ$  with a field of view of  $6.0^\circ \times 6.0^\circ$  (Galactic coordinate system).

**Table A5.** Summary of recovered flux densities for Tycho. The  $P$ ,  $\Pi$  and  $\gamma$  are obtained from the raw flux densities (second, third and fourth columns).

$\nu$ [GHz]	$I$ [Jy]	$Q$ [Jy]	$U$ [Jy]	$P$ [Jy]	$\gamma$ [deg]	$\Pi$ [%]
0.408	88.6±8.9	-	-	-	-	-
0.820	58.1±5.9	-	-	-	-	-
1.420	49.7±5.0	-	-	-	-	-
4.800	25.9±2.6	-1.10±0.16	-0.87±0.13	1.40±0.15	-19.2±3	5.4±0.8
11.1	12.7±1.3	-0.25±0.13	-0.04±0.13	0.22±0.15	-4.5±19	1.6 <sup>1.2</sup> <sub>0.9</sub>
12.9	11.9±1.4	-0.23±0.17	-0.26±0.15	0.31±0.18	-24.2±16	2.6 <sup>1.6</sup> <sub>1.4</sub>
16.8	8.8±1.5	-0.35±0.15	-0.18±0.19	0.35±0.18	-13.6±15	4.1±2.2
18.8	7.6±2.1	-0.01±0.16	0.09±0.28	0.05±0.49	-	-
22.8	9.9±1.2	-0.15±0.09	-0.14±0.09	0.19±0.10	-21.5±15	1.8±1.0
28.4	7.7±1.1	-0.11±0.06	-0.04±0.06	0.10±0.07	-10.0±19	1.2 <sup>0.9</sup> <sub>0.7</sub>
32.9	6.7±1.1	0.03±0.04	-0.01±0.10	0.02±0.09	-	<2.0
40.7	5.6±1.3	0.01±0.08	0.17±0.16	0.15±0.18	-43.3±34	<6.2
44.1	5.0±1.5	-0.08±0.19	0.17±0.11	0.13±0.18	32.4±40	<8.6
60.7	3.1±2.3	-0.22±0.21	-0.42±0.28	0.42±0.30	-31.2±20	<43.6
70.4	1.4±2.9	-0.29±0.31	-0.28±0.18	0.33±0.31	-22.0±27	<176.0
93.5	-0.3±4.8	-0.77±0.59	-0.96±0.84	1.04±0.89	-25.6±24	-
100	7±11	0.18±0.55	-0.90±0.29	0.77±0.36	39.4±14	<58.5
143	16±15	0.54±1.84	-2.06±1.03	1.56±1.50	37.7±28	<43.4
217	136±80	0.80±7.16	-8.57±3.41	6.34±4.70	42.3±21	<16.7
353	582±284	0.14±33.84	-37.44±14.84	26.64±20.85	44.9±22	6.3 <sup>5.6</sup> <sub>3.7</sub>
545	1835±374	-	-	-	-	-
857	4696±1013	-	-	-	-	-
1249	7732±1765	-	-	-	-	-
2141	8326±1797	-	-	-	-	-
2997	2779±688	-	-	-	-	-

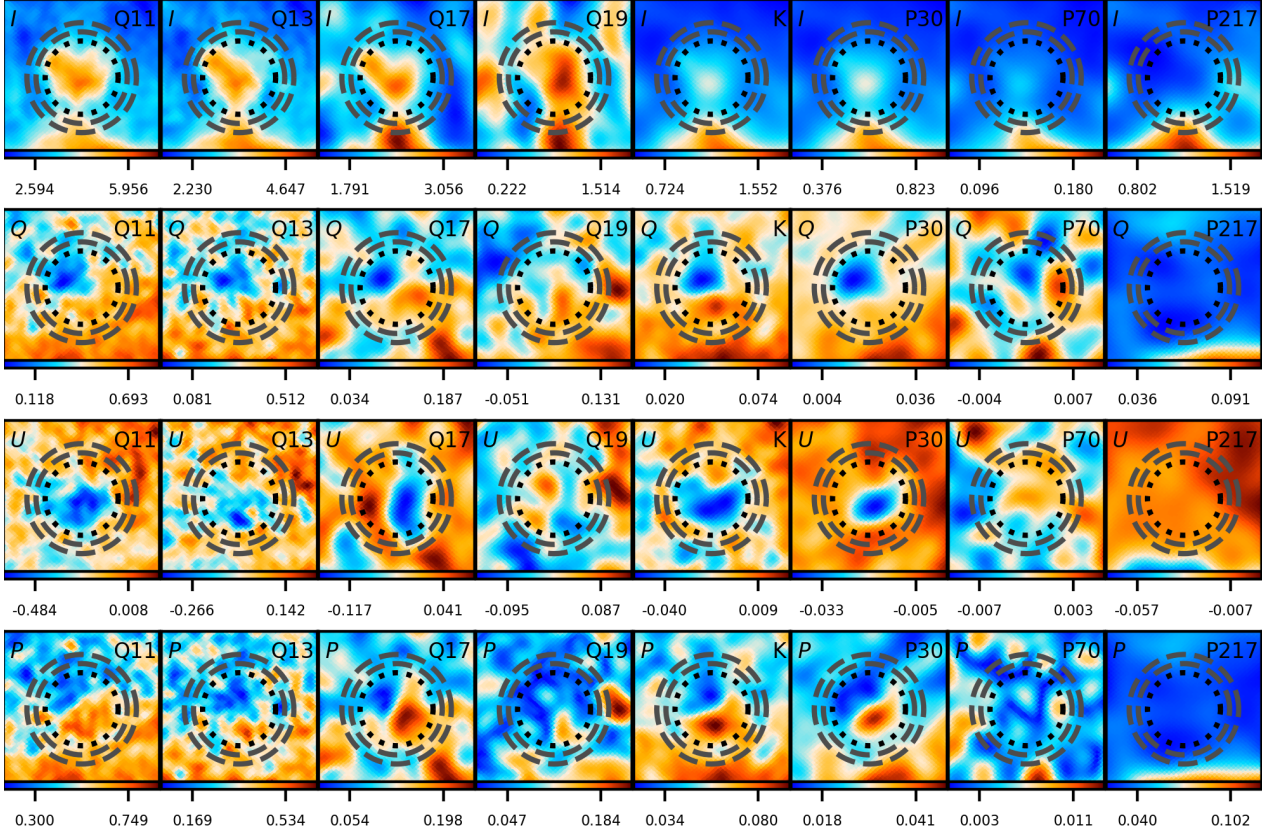


**Figure A4.** Intensity and polarization maps of CTA 1 from the QUIJOTE, WMAP and *Planck* data. Maps are smoothed to an angular resolution of 1 deg, and centred on  $l, b = 119.5^\circ, 10.0^\circ$  with a field of view of  $5.7^\circ \times 5.7^\circ$  (Galactic coordinate system).

**Table A6.** Summary of recovered flux densities for HB 9. The  $P$ ,  $\Pi$  and  $\gamma$  are obtained from the raw flux densities (second, third and fourth columns).

$\nu$ [GHz]	$I$ [Jy]	$Q$ [Jy]	$U$ [Jy]	$P$ [Jy]	$\gamma$ [deg]	$\Pi$ [%]
0.408	102±10	-	-	-	-	-
0.820	79.3±8.0	-	-	-	-	-
1.420	58.9±5.9	-	-	-	-	-
4.800	35.0±3.5	2.12±0.23	-0.82±0.10	2.27±0.22	10.6±3	6.6±0.8
11.1	21.2±1.4	1.84±0.24	0.05±0.18	1.83±0.24	-0.8±4	8.7 <sup>1.1</sup> <sub>1.2</sub>
12.9	19.5±1.5	1.43±0.22	0.39±0.24	1.46±0.22	-7.6±4	7.4 <sup>1.3</sup> <sub>1.4</sub>
16.8	16.4±1.9	0.69±0.31	-0.08±0.21	0.66±0.32	3.3±14	4.0 <sup>1.8</sup> <sub>1.7</sub>
18.8	16.2±3.6	0.63±0.48	-0.33±0.18	0.66±0.47	13.8±20	<7.8
22.8	14.6±1.4	0.79±0.15	-0.01±0.08	0.79±0.15	0.4±5	5.3±0.9
28.4	12.7±1.4	0.88±0.12	0.02±0.08	0.88±0.12	-0.7±4	6.9±1.1
32.9	12.5±1.8	0.42±0.18	-0.23±0.19	0.44±0.20	14.3±13	3.5 <sup>1.7</sup> <sub>1.6</sub>
40.7	12.3±2.5	0.21±0.25	-0.10±0.42	0.13±0.50	-	<6.1
44.1	12.2±2.9	0.08±0.29	0.50±0.23	0.43±0.27	-40.5±18	3.2 <sup>2.5</sup> <sub>2.1</sub>
60.7	12.6±5.7	-0.66±0.59	-0.24±0.53	0.53±0.77	80.0±41	<14.3
70.4	14.9±7.3	0.35±0.49	-0.64±0.38	0.59±0.50	30.7±24	<11.8
93.5	15±12	0.32±1.60	-0.27±1.79	0.22±3.27	-	<24.3
100	30±12	-0.50±0.71	-0.42±0.39	0.48±0.82	70.0±49	<5.4
143	36±21	-1.18±1.83	-2.10±1.30	1.88±1.85	59.7±28	<17.3
217	147±49	-5.04±5.08	-11.23±4.85	11.28±5.34	57.1±14	9.1 <sup>5.4</sup> <sub>3.8</sub>
353	580±230	-20.30±19.15	-45.34±23.20	45.71±24.54	57.1±15	9.0 <sup>5.4</sup> <sub>4.8</sub>
545	1726±380	-	-	-	-	-
857	4388±1000	-	-	-	-	-
1249	5424±1685	-	-	-	-	-
2141	5269±1625	-	-	-	-	-
2997	892±515	-	-	-	-	-

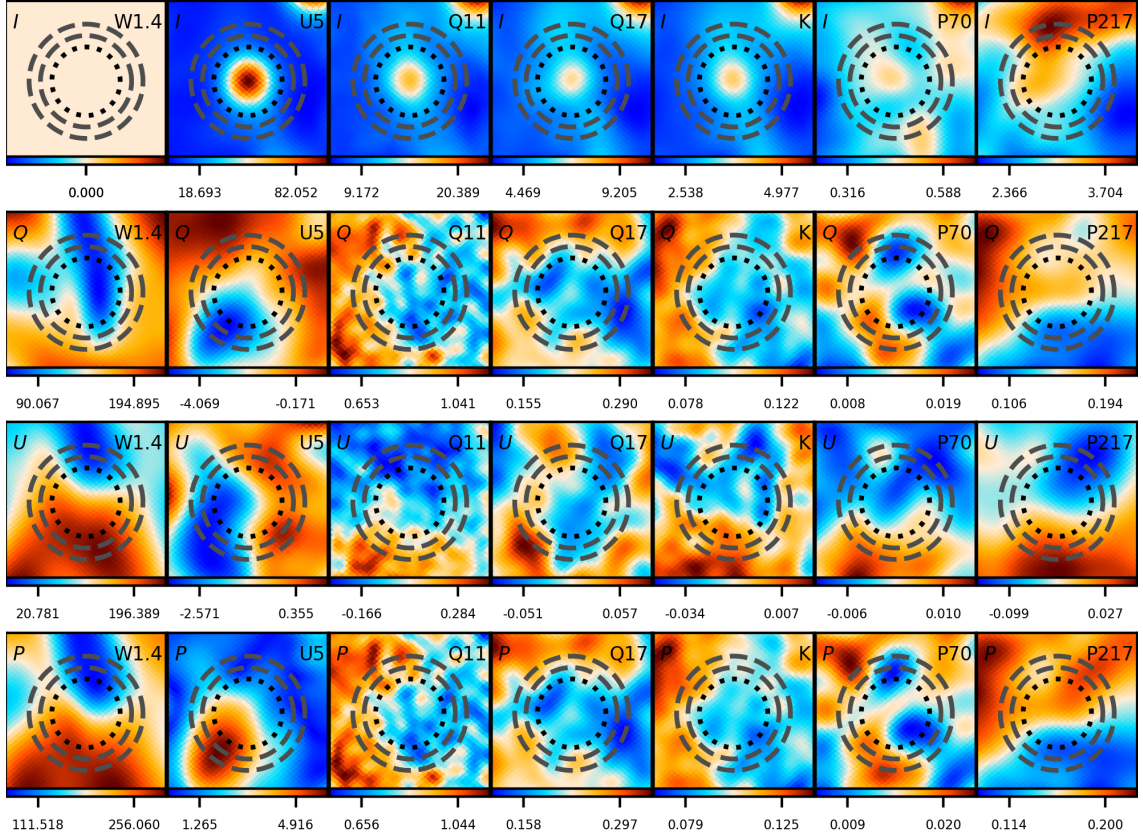


**Figure A5.** Intensity and polarization maps of Tycho from the QUIJOTE, WMAP and *Planck* data. Maps are smoothed to an angular resolution of 1 deg, and centred on  $l, b = 120.1^\circ, 1.4^\circ$  with a field of view of  $4.7^\circ \times 4.7^\circ$  (Galactic coordinate system).

**Table C1.** Integrated radio flux densities of CTB 80 and HB 21 taken from the literature.

$\nu$ [MHz]	$I$ [Jy]	$\nu$ [MHz]	$I$ [Jy]
<b>CTB 80</b>			
240	$106.0 \pm 16.0$	1400	$75.0 \pm 8.0$
324	$91.0 \pm 10.0$	1410	$62.0 \pm 9.0$
408	$67.0 \pm 13.0$	1420	$80.0 \pm 10.0$
408	$67.6 \pm 10.5$	1720	$66.0 \pm 6.6$
408	$83.0 \pm 15.0$	2695	$51.0 \pm 5.1$
750	$127.0 \pm 15.0$	2700	$42.2 \pm 4.2$
750	$75.0 \pm 8.0$	4750	$44.0 \pm 4.4$
1000	$121.0 \pm 15.0$	10200	$18.8 \pm 1.9$
1380	$56.0 \pm 6.0$	-	-
<b>HB 21</b>			
38	$790.0 \pm 200.0$	960	$170.0 \pm 60.0$
81	$530.0 \pm 120.0$	1420	$183.0 \pm 18.3$
158	$280.0 \pm 80.0$	1430	$190.0 \pm 30.0$
178	$375.0 \pm 40.0$	2700	$148.0 \pm 16.0$
178	$440.0 \pm 100.0$	2965	$160.0 \pm 30.0$
400	$190.0 \pm 60.0$	4170	$160.0 \pm 40.0$
408	$259.0 \pm 25.9$	4800	$107.3 \pm 10.7$
611	$308.0 \pm 60.0$	5000	$103.0 \pm 18.0$
863	$228.0 \pm 22.8$	-	-

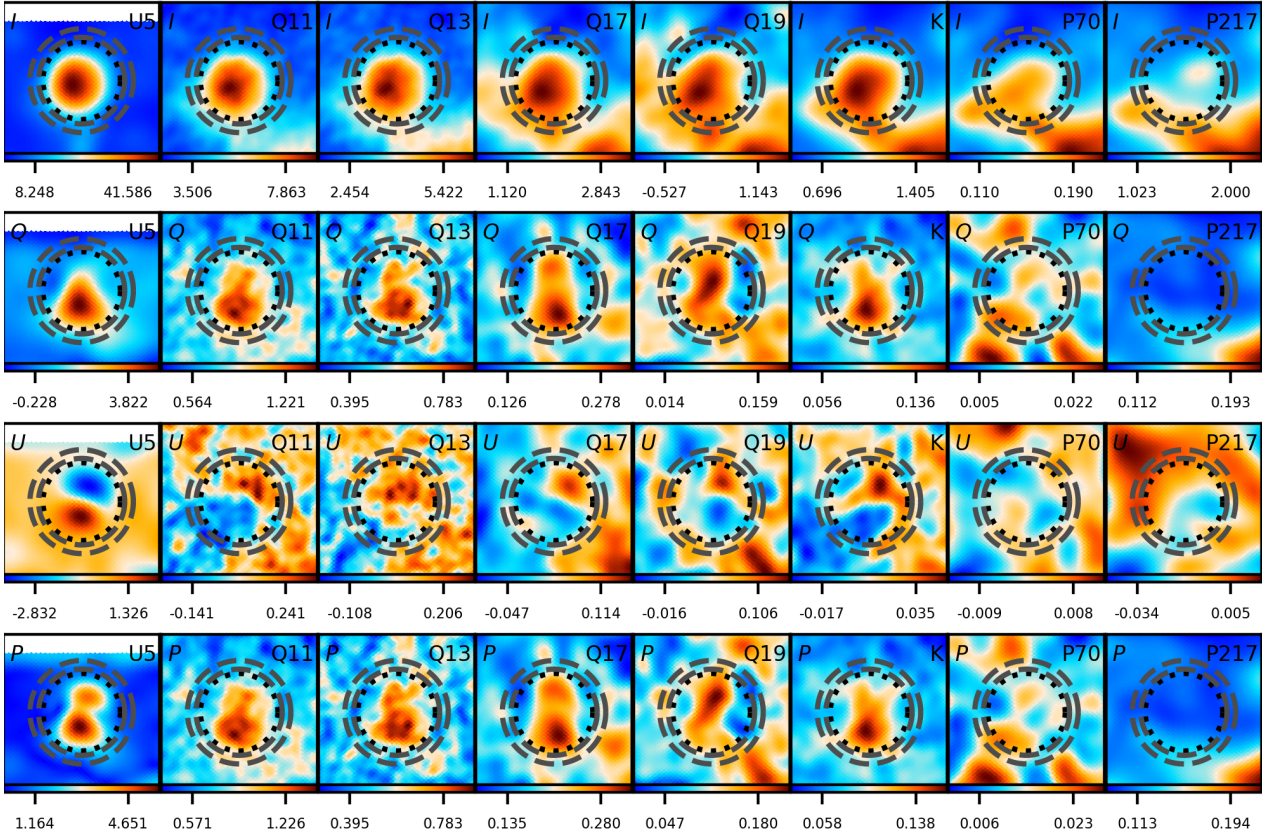


**Figure A6.** Intensity and polarization maps of HB 9 from the QUIJOTE, WMAP and *Planck* data. Maps are smoothed to an angular resolution of 1 deg, and centred on  $l, b = 160.4^\circ, 2.8^\circ$  with a field of view of  $6.0^\circ \times 6.0^\circ$  (Galactic coordinate system).

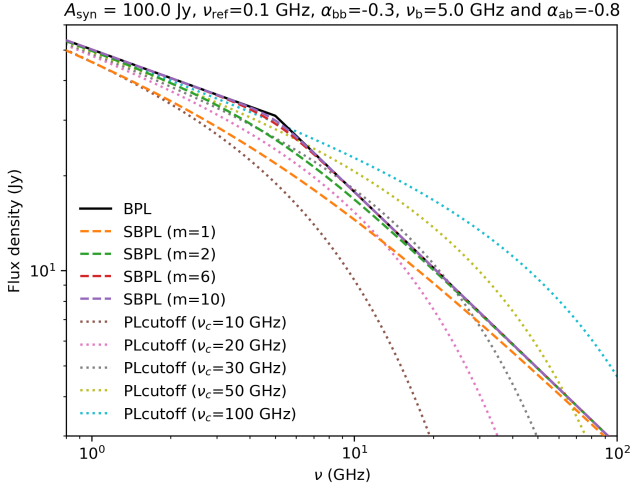


**Figure B1.** Parametric models that were explored to characterize the curved spectra of CTB 80 and HB 21. These are displayed according to the broken power law (solid line, equation B3), to the smooth broken power law (dashed lines, equation 6), and to the power law with exponential cut-off (dotted lines, equation B1). Overall, the amplitude is fixed to  $A_{\text{syn}} = 100 \text{ Jy}$  at  $\nu_{\text{ref}} = 0.1 \text{ GHz}$ , with a radio spectral index of  $\alpha = \alpha_{\text{bb}} = -0.3$ , a break frequency  $\nu_b = 5 \text{ GHz}$  and a spectral index above the break frequency of  $\alpha_{\text{ab}} = -0.8$ . For the  $S_{\text{PLcutoff}}$  model, the coloured dotted lines identify the cut-off frequency  $\nu_c$ . Similarly, the coloured dashed lines represent the  $m$  value considered for the  $S_{\text{SBPL}}$  model.